University of South Carolina
Scholar Commons

Theses and Dissertations

2016

Numerical Studies Of Arterial Tissue Failure

Xiaochang Leng
University of South Carolina

Follow this and additional works at: https://scholarcommons.sc.edu/etd

 Part of the Mechanical Engineering Commons

Recommended Citation

Leng, X.(2016). *Numerical Studies Of Arterial Tissue Failure.* (Doctoral dissertation). Retrieved from https://scholarcommons.sc.edu/etd/3752

This Open Access Dissertation is brought to you by Scholar Commons. It has been accepted for inclusion in Theses and Dissertations by an authorized administrator of Scholar Commons. For more information, please contact dillarda@mailbox.sc.edu.

NUMERICAL STUDIES OF ARTERIAL TISSUE FAILURE

by

Xiaochang Leng

Bachelor of Science
Wuhan University of Technology, 2008

Master of Science
Wuhan University of Technology, 2011

Submitted in Partial Fulfillment of the Requirements

For the Degree of Doctor of Philosophy in

Mechanical Engineering

College of Engineering and Computing

University of South Carolina

2016

Accepted by:

Xiaomin Deng, Major Professor

Susan M. Lessner, Committee Member

Michael A. Sutton, Committee Member

Tarek Shazly, Committee Member

Lacy Ford, Senior Vice Provost and Dean of Graduate Studies

© Copyright by Xiaochang Leng, 2016
All Rights Reserved.

ACKNOWLEDGEMENTS

I would like to express my deep gratitude to my supervisor Prof. Xiaomin Deng for giving me the opportunity to be a part of his laboratory. He provided me with the scientific advice and the enthusiasm without which this work could not be possible. I am also very grateful to Prof. Susan M. Lessner for her support and valuable suggestions during the PhD program. I wish to further thank my other two committee members, Prof. Michael A. Sutton and Prof. Tarek Shazly for valuable advices and precious time.

I am indebted to my long-term work partner, Dr. Boran Zhou and Lindsey Davis, who have taken enormous efforts to perform the biomechanical tests for arterial tissue failure. Many thanks also go to Dr. Yingchao Yang from Rice University, who conducted the micromechanical tests for this study. I must acknowledge Dr. Xin Chen and Hongsheng Zhang for sharing with their experience and knowledge on fracture mechanics and computational mechanics. My appreciation also goes to colleagues, friends and department staff for their generous help and assistance.

This work would not have been possible without the steadfast love and support from my family and other relatives. In particular, I would like to thank my wife, Liqiong Tian, and my little angel, Yanqi Leng, for their endless love, sacrifices and support.

ABSTRACT

Arterial tissue failure leads to a number of potentially life-threatening clinical conditions, such as atherosclerotic plaque rupture and aortic dissection which develop unpredictably and rapidly in vivo. Thus, a full understanding of the two conditions will provide a solid basis for medical advances in the intervention and prevention of the occurrence of this life-threatening event. The present work aims to develop a cohesive zone model (CZM) approach for analysis and simulation of arterial tissue failure, such as plaque and fibrous cap delamination and tearing, and to validate simulation predictions with experimental results.

To characterize the hysteresis phenomenon of diseased aortic tissue, a viscoelastic anisotropic (VA) model for the bulk arterial material behavior is proposed based on a hyperelastic anisotropic model and a general viscoelastic formulation in the literature. The viscoelastic effects of the material are taken into account by using a generalized Maxwell model. In order to capture the failure process of the interface between arterial layers, three types of cohesive zone models were considered, which include the exponential, triangular and trapezoidal CZMs.

Atherosclerotic plaque delamination experiments performed on ApoE-KO mouse aorta specimens were simulated using the CZM approach. A three-dimensional (3D) finite element model for the experiments was developed, in which the Holzapfel-Gasser-Ogden

(HGO) model for the bulk arterial material behavior and a CZM for the plaque-media interface behavior are adopted. A set of HGO and CZM parameter values were obtained through a material parameter identification procedure in which a subset of experimental loading-delamination-unloading cycle data was used. Simulation predictions for additional loading-delamination-unloading cycles were obtained, which show good agreement with experimental measurements.

Two types of delamination experiments (a "mixed-mode" type and a "mode I" type) were conducted on porcine aorta specimens. These experiments were analyzed and compared using finite element simulations. Simulation results revealed that the intuitive classification of these two types of experiments is not necessarily accurate for soft tissue materials. In particular, the "mixed-mode" experiment was found to have a dominant mode II component in the cohesive zone ahead of the growing delamination front.

Human fibrous cap delamination experiments were conducted and simulated using the finite element method by employing the VA bulk material model and three types of CZMs. A set of VA and CZM parameter values was determined using the same material parameter identification procedure as in the simulations of mouse plaque delamination experiments. Using this set of parameter values, simulation predictions for two sequential loading-delamination-unloading cycles were performed, which show good agreement with experimental measurements, including the hysteresis behavior during unloading. Furthermore, a mode I tearing test was conducted on human fibrous cap in order to investigate the failure process of plaque rupture. The CZM parameter values were obtained through an inverse analysis. These parameter values will provide input for further numerical simulation of plaque rupture events.

The CZM based approach was applied to develop a micromechanical model for arterial delamination along the interface between the fibrous cap and the underlying plaque tissue in order to understand delamination mechanisms, including fiber bridging. A 3D unit cell containing an individual fiber between two arterial tissue layers was considered. With the unit cell model, micromechanical factors affecting the resulting traction-separation relation were investigated through a parametric study.

TABLE OF CONTENTS

ACKNOWLEDGEMENTS iii

ABSTRACT iv

LIST OF TABLES xi

LIST OF FIGURES xiii

CHAPTER 1 INTRODUCTION 1

1.1 BACKGROUND AND MOTIVATION 1

1.2 LITERATURE REVIEW 6

1.3 RESEARCH OBJECTIVES 13

1.4 OUTLINE OF THE DISSERTATION 14

CHAPTER 2 ANISOTROPIC HYPERELASTIC MODEL FOR ARTERIAL MATERIAL 17

2.1 INTRODUCTION 17

2.2 ANISOTROPIC HYPERELASTIC MODEL: HOLZAPFEL-GASSER-OGDEN (HGO) MODEL 18

2.3 STRESS TENSORS 20

2.4 ELASTICITY TENSORS 23

2.5 VISCOELASTIC ANISOTROPIC (VA) MODEL 23

2.6 CONCLUSIONS 26

CHAPTER 3 INTERFACE DAMAGE MODEL 28

3.1 Introduction 28
3.2 Interface Cohesive Element 28
3.3 Mixed-Mode Cohesive Zone Model 32
3.4 Exponential CZM 35
3.5 Triangular CZM 40
3.6 Trapezoidal CZM 44
3.7 Summary 49
CHAPTER 4 Modeling of Experimental Atherosclerotic Plaque Delamination 50
4.1 Introduction 50
4.2 Experimental Procedure 51
4.3 Numerical Simulations of Atherosclerotic Plaque Delamination 53
4.4 Convergence Analysis 65
4.5 Prediction and Validation 66
4.6 Analysis of the Effects of the Geometric Uncertainty 69
4.7 Conclusions 71
CHAPTER 5 Experimental and Numerical Studies of Mixed-Mode and Mode I Delamination of Arterial Wall 74
5.1 Introduction 74
5.2 Experimental Procedure 76
5.3 Numerical Implementation 77
5.4 Results 81
5.5 Discussion 88
5.6 Conclusions 92
CHAPTER 6 Numerical Modeling of Experimental

HUMAN FIBROUS CAP DELAMINATION 93
6.1 INTRODUCTION 93
6.2 EXPERIMENTAL DETAILS 95
6.3 MODELING AND SIMULATION 98
6.4 RESULTS 106
6.5 PREDICTION AND VALIDATION 107
6.6 DISCUSSION 111
6.7 CONCLUSIONS 113
CHAPTER 7 AN INVERSE ANALYSIS OF COHESIVE ZONE MODEL PARAMETER VALUES FOR HUMAN FIBROUS CAP MODE I TEARING SIMULATIONS 115
7.1 INTRODUCTION 115
7.2 MATERIALS AND METHODS 117
7.3 NUMERICAL IMPLEMENTATION 118
7.4 RESULTS 122
7.5 DISCUSSION 127
7.6 CONCLUSIONS 129
CHAPTER 8 EXPERIMENTAL AND NUMERICAL STUDIES OF COLLAGEN FIBER FAILURE IN ARTERIAL TISSUE 130
8.1 INTRODUCTION 130
8.2 MATERIALS AND METHODS 131
8.3 NUMERICAL IMPLEMENTATION 133
8.4 MATERIAL PROPERTIES IDENTIFICATION PROCESS 134
8.5 RESULTS 135
8.6 PARAMETRIC STUDIES 138
8.7 DISCUSSION 145

8.8 Conclusions 148
CHAPTER 9 Conclusions and Future Work 150
REFERENCES 155
APPENDIX A – Derivation of Tangential Modulus 168
APPENDIX B – Derivation of Elastic Tensor 171
APPENDIX C – Inverse Analysis Method 174

LIST OF TABLES

Table 2.1 Summary of the procedure for creating an efficient user material subroutine implemented in ABAQUS 26

Table 3.1 Summary of the quantities required for an efficient finite element implementation of exponential CZM in writing UEL subroutine for ABAQUS. 39

Table 3.2 Summary of the quantities required for an efficient finite element implementation of triangular CZM in writing UEL subroutine for ABAQUS. 43

Table 3.3 Summary of the quantities required for an efficient finite element implementation of trapezoidal CZM in writing UEL subroutine for ABAQUS. 47

Table 4.1 Material parameters of mouse arterial wall and plaque identified from specimen #1 61

Table 4.2 Stiffness of spring for specimen #1 and specimen #2 61

Table 4.3 CZM parameter values 63

Table 5.1 Material parameter values of HGO model 80

Table 5.2 CZM parameter values 81

Table 5.3 The values of energy release rate (Gc) for mixed-mode and mode I delamination of porcine aortic tissue: Mix-C1~Mix-C6, Mix-A1~Mix-A6, MI-C1~MI-C6 and MI-A1~MI-A6 are the specimens of mixed-mode and mode I delamination tests from circumferential and axial directions, respectively. 83

Table 6.1 HGO and VA material model parameter values 103

Table 6.2 CZM parameter values 103

Table 6.3 Critical energy release rate values from fibrous cap delamination tests 106

Table 7.1 Best-fit parameters for the HGO model of human fibrous cap samples under uniaxial tensile tests. 122

Table 7.2 The values of critical energy release rate and interfacial strength of fibrous cap tissue from inverse analysis method. 123

Table 8.1 Diameter, strain at failure and ultimate strength from fiber tensile tests..... 136

Table 8.2 Material parameter values of exponential CZM 137

Table 8.3 Material parameter values of HGO model..... 141

LIST OF FIGURES

Fig. 1.1 Images of arterial delamination events: (a) A schematic image of a ruptured plaque, with rupture circled; (b) plaque delamination from the underlying media layer (blue arrow) (Wang et al., 2013); (c) delamination within the media layer (Madaloso and Benvenuti, 2013); (d) fibrous cap delamination from the underlying plaque tissue (Tavora et al., 2010); (e) fibrous cap rupture at the at shoulder (red arrow) (Pasterkamp et al., 2000); (f) collagen fibers bridging at a delamination interface in a microscale fiber pullout test. 4

Fig. 2.1 Arterial tube with helicoidal arrangement of two families of fibers in cylindrical and rectangular coordinate systems. The two direction vectors $\boldsymbol{a}_{01}$ and $\boldsymbol{a}_{02}$ are tangent to the fiber directions and $2r$ is the angle between $\boldsymbol{a}_{01}$ and $\boldsymbol{a}_{02}$. 19

Fig. 2.2 Schematic model of a viscoelastic material (Unterberger et al., 2013). 24

Fig. 3.1 Eight node interface element for three dimensional analysis. 31

Fig. 3.2 Interfacial triangular mixed-mode cohesive traction-separation law. 32

Fig. 3.3 Schematic of the tractions and displacement jump perpendicular and across to the cohesive surface. 36

Fig. 3.4 Exponential irreversible cohesive model denotes with normalized effective traction and effective displacement. 38

Fig. 3.5 Triangular irreversible cohesive model denotes with effective traction and effective displacement. 41

Fig. 3.6 Trapezoidal irreversible cohesive model denotes with effective traction and effective displacement. 45

Fig. 4.1 A schematic of the atherosclerotic plaque delamination experimental setup: (a) Side view of the schematic diagram of the experiment, a mouse specimen on a loading table; (b) a schematic diagram of the experimental process represented by a finite element; ; (c) top view of the schematic diagram of the experiment; (d) three typical consecutive experimental load vs. load-point displacement curves. 52

Fig. 4.2 An experimental delamination image of a mouse plaque specimen (specimen #1). The "upper face" is the separated surface pulled by the micro-clamp, and the "lower face" is the exposed surface. Scale bar=1 mm. 55

Fig. 4.3 A FE model of the mouse aorta (specimen #1): (a) a FE model for delamination simulation, where L is the length of the atherosclerotic plaque; elastic springs under the arterial wall in x, y and z directions. (b) a cross-sectional view of the aorta and parameters, where r is the radius of the aortic wall curvature away from the plaque, R is the radius of curvature of the interface between the plaque and the arterial wall, t is the thickness of the aortic wall, W is the width of the plaque, T is the height of the atherosclerotic plaque, and C_0 is the total circumferential width of the aortic wall. 57

Fig. 4.4 (a) The simulated load-displacement curve of the first loading-unloading cycle from specimen #1 is compared with the measured curve, $G_c = 0.019\ \mathrm{N/mm}$. (b) The simulated load-displacement curve of the first loading-unloading cycle from specimen #2 is compared with the measured curve, $G_c = 0.01\ \mathrm{N/mm}$. The entire cycle includes the loading phase in which the plaque is pulled without delamination, the delamination phase in which the plaque is pulled and separated from the underlying internal elastic lamina (IEL), and the unloading phase in which the plaque is returned to the initial position. 62

Fig. 4.5 von Mises stress (MPa) contours for three typical points of loading-unloading cycle of plaque delamination simulation from specimen #1. 62

Fig. 4.6 (a) Cross-section of three different meshes, (b) predicted 1st-cycle load-displacement curves using the three meshes, with comparison to the experimental curve. 66

Fig. 4.7 Comparisons of the predicted and measured load-displacement curves for loading-unloading cycles. (a) cycle 2 and (b) cycle 3 of specimen #1; (c) cycle 2 and (d) cycle 3 of specimen #2. 67

Fig. 4.8 Analysis of the effects of the geometric uncertainty: (a) The cross-sections of finite element models with three typical atherosclerotic plaque thicknesses. (b) Predicted load-displacement curves from simulations with three different thicknesses. (c) The cross-sections of finite element models with three typical atherosclerotic plaque curvatures. (d) Predicted load-displacement curves from simulations with three different curvatures. 70

Fig. 5.1 Schematic of experimental setup. (a) A radial cut was made on the porcine abdominal aorta and strips oriented at the angle of 0^o and 90^o with respect to the circumferential vessel axis were obtained; (b) Experimental setup of delamination tests; (c) mixed-mode and (d) mode I delamination experiment setup (zoomed-in view). 77

Fig. 5.2 Images of (a) mixed-mode and (b) mode-I delamination experiments on porcine abdominal aorta specimens, and deformed shapes of (c) the mixed-mode and (d) mode-I specimens from finite element simulations. The right delaminated part of the specimen (red section) contains intima and part of media, and the left delaminated part (blue section) contains adventitia and part of media. The delamination of aorta propagated inside the media layer. 78

Fig. 5.3 The predicted load-displacement curves of one loading-unloading cycle are compared with the measured curves. (a) mixed-mode delamination; (b) mode I delamination..... 80

Fig. 5.4 Load/width versus load-point displacement curves for 6 circumferential and 6 axial strip specimens of mixed-mode delamination tests. The thick black curves represent the arithmetic mean values..... 82

Fig. 5.5 Load/width versus load-point displacement curves for 6 circumferential and 6 axial strip specimens of Mode I delamination tests. The thick black curves represent the arithmetic mean values..... 82

Fig. 5.6 The simulation predicted load-displacement curves of four loading-delamination-unloading cycles are compared with the experimentally measured curves: (a) cycle 2 and (b) cycle 3 of mixed-mode delamination; (c) cycle 2 and (d) cycle 3 of mode I delamination. 85

Fig. 5.7 Comparison of predicted and measured delamination front profiles: (a) mixed-mode experiment; (b) mode I experiment..... 86

Fig. 5.8 Predicted ratios of $\left(\frac{\delta s1}{\delta}\right)^2$ and $\left(\frac{\delta n}{\delta}\right)^2$; figurative depiction of the definition of delamination fronts (damage parameter equals to one) for (a) mixed mode and (b) mode I fracture; ratios of $\left(\frac{\delta s1}{\delta}\right)^2$ and $\left(\frac{\delta n}{\delta}\right)^2$ of delamination tests for mixed mode (c) at the outside surface and (d) at the mid-plane as well as for mode I (e) at the outside surface and (f) at the center plane, respectively. 87

Fig. 5.9 (a) Loading angles at middle plane θ_{mid} and outside surface θ_{out}; (b) predicted ratios of $\left(\frac{\delta s1}{\delta}\right)^2$ and $\left(\frac{\delta n}{\delta}\right)^2$ related to loading angles for mixed-mode experiment. 88

Fig. 6.1 Fibrous cap delamination experiments: experimental setup (scale bar=5 mm)..... 96

Fig. 6.2 Histological images of the fibrous cap delamination surfaces after Masson's Trichrome staining: (a) a longitudinal section of a completely delaminated specimen, including a partial media and the tissues of atherosclerotic plaque and fibrous cap; (b) a fibrous cap delaminated from the underlying plaque tissue. In

these images, the collagen is stained blue, the nuclei are stained purple-black, and the smooth muscle cells (SMCs) are stained red. (Lipid rich core and necrotic core are identified by LC and NC labels, respectively)..... 97

Fig. 6.3 Representative experimental images of the fibrous cap delamination specimen: (a) a front view of the specimen and the finite element (FE) model; (b) a top view of the specimen and the FE model; (c) the delamination area and the area for simulation predictions are marked by red color (the delamination direction is along the X axis); (d) the FE model based on the geometric model reconstructed from the images. 100

Fig. 6.4 Predicted load-displacement curves of three different cycles using three different types of CZM, with comparison to the experimental curve..... 104

Fig. 6.5 (a) Mesh 1 and Mesh 2 (a refinement of Mesh 1) of the 3D finite element model ; (b) the predicted load-displacement curves for three loading cycles using the two meshes; (c) relative percent error in the reaction load vs. displacement between Mesh 2 and Mesh 1 (M2/M1) for three loading cycles. 105

Fig. 6.6 The simulation-predicted load-displacement curves of nine loading-delamination-unloading cycles are compared with the measured curves: (a) the load-displacement curves and (b) relative error vs. displacement curves for cycles #1, #2 and #3 for sample FC1; (c) load-displacement curves and (d) relative error vs. displacement curves for cycles #4, #5 and #6 for sample FC1; (e) the load-displacement curves and (f) relative error vs. displacement curves of cycles #1, #2 and #3 for sample FC2..... 108

Fig. 6.7 von Mises stress contours at three typical points during loading-delamination-unloading cycle #3: (a) at point 1 in the loading phase; (b) at point 2 in the delamination phase; (c) at point 3 in the unloading phase; (d) the effective traction contours in the cohesive elements at point 2; (e) the cohesive damage parameter contours in the cohesive elements at point 2. 110

Fig. 7.1 Schematic of experimental setup. (a) Schematic of carotid artery plaque specimens obtained from endarterectomies and cut to strips transversely (A: axial direction; C: circumferential direction); (b) Experimental setup of fibrous cap tearing tests; (c) experiment setup (zoomed-in view)..... 118

Fig. 7.2 Representative experimental images of the fibrous cap tearing specimen: (a) a front view of the specimen; (b) a side view of the specimen; (c) FE model of front view of the specimen, which the white line shows the initial separated path and the red dot line represents the predefined tearing path that will be teared during the experiment; (d) FE model of side view of the specimen. 119

Fig. 7.3 Flow chart of the inverse analysis of fibrous cap tearing tests which used to obtain the cohesive interface parameter values along the tearing path..... 121

Fig. 7.4 The simulation predicted load-displacement curves of loading-tearing cycles are compared with the experimental measured curves. 124

Fig. 7.5 (a) Variations of CZM parameters and (b) objective function with iteration numbers of inverse modeling of tearing experiment for sample FCT-1..... 125

Fig. 7.6 Tension stress (S22, along Y direction) contours at eight typical points along the load-displacement curve during tearing process: (a) tension deformation from experiment and (b) simulation prediction. 126

Fig. 8.1 Schematic of set-up for tensile testing in SEM. (a) A radial cut was made on the porcine abdominal aorta and strips oriented at the angle of 0^o and 90^o with respect to the circumferential vessel axis were obtained; (b) a strip was teared into two parts and a bundle of collagen fibers was harvested at the teared surface; (c) collagen fiber uniaxial tensile test setup..... 132

Fig. 8.2 Schematic representation of the numerical implementation of micromechanical model with fiber breakage. (a) SEM image of collagen fibers from the uniaxial tensile test and FE model of collagen fibers; (b) best fitting of load vs. load-point displacement curve between the simulation predictions and experimental measurements; (c) Schematic illustration of parametric studies using 3D unit cell model..... 133

Fig. 8.3 (a) SEM image of fibers after the tensile test and (b) the zoom-in image of the breakage surface of the collagen fibers..... 134

Fig. 8.4 Cauchy stress-strain curves from collagen fiber tensile tests. 136

Fig. 8.5 The simulation predicted load-displacement curves of tensile tests of collagen fibers are compared with the experimental measured curves. 138

Fig. 8.6 Schematic representation of 3D unit cell models distributed in the fibrous cap delamination path..... 139

Fig. 8.7 Finite element model of the 3D unit cell model for micromechanical study of fibrous cap delamination: (a) left section view of 3D unit cell model, the collagen fibers connecting fibrous cap and underlying plaque tissue (the red line shows a zero thickness layer of cohesive elements assigned to the interface across fibers at the middle of fibers); (b) front view of 3D unit cell model; (c) collagen fibers; (d) top section view of 3D unit cell model. 140

Fig. 8.8 Traction-separation curves from simulation predictions with five different values of (a) critical energy release rate G_c and (b) interfacial strength σ_c. 143

Fig 8.9 Traction-separation curves from simulations with five different values of (a) elastic modulus E and (b) Poisson's ratio ν..... 144

Fig. 8.10 Traction-separation curves from simulations with five different values of initial gap of the interface L_g. 144

CHAPTER 1

INTRODUCTION

1.1 Background and Motivation

Arterial tissue failure leads to a number of potentially life-threatening clinical conditions, including atherosclerotic plaque rupture and aortic dissection. Atherosclerotic plaque rupture is a serious complication of advanced atherosclerosis, often leading to catastrophic clinical consequences such as myocardial infarction (heart attack) or stroke (Assemat and Hourigan, 2013; Badimon and Vilahur, 2014; Schwartz et al., 2007). Roughly 75% of all myocardial infarctions originate from plaque rupture and approximately 1.1 million people are affected in the USA per year (Virmani, 2007). The American Heart Association has developed a method to predict future costs of cardiovascular disease, which includes coronary heart disease and stroke; associated costs are estimated to increase from $172 billion in 2010 to $276 billion in 2030 (Heidenreich et al., 2011). These forecasts illustrate the magnitude of the clinical problems resulting from arterial tissue failure and the importance of improving our basic understanding of the arterial failure process. A full understanding of plaque rupture will provide a solid basis for medical advances in intervention and prevention of this life-threatening event.

A common plaque rupture site is the shoulder region (Fig. 1.1a, blue arrow) where the interface between the plaque and the underlying vascular wall is located (Loree et al., 1992). This site is prone to delaminate along the plaque-media interface, for example, when the arterial wall experiences large expansion under balloon angioplasty (Badel et al., 2014). In general, due to mismatch in mechanical properties across a vessel wall interface, interlayer shear stress concentration is expected to occur at geometric discontinuities (e.g. along the edge of the plaque-media interface) when the artery is deformed, which may cause initiation of interfacial delamination. Plaque delamination (dissection) (Fig. 1.1b) at the shoulder with intimal flap formation during balloon angioplasty and stenting has been demonstrated by in vivo imaging modalities such as intravascular ultrasound and optical coherence tomography (Ferrante, 2013; Honye, 1992; Sakai, 2003; Tearney, 2012). Shear loading due to flow induced shear traction on the plaque surface is also expected to contribute to the initial tearing and delamination of the plaque. The subsequent delamination growth may be mixed-mode, in which the Mode I (opening mode) component can be significant. The Mode I component can be due to the normal loading from flow pressure (e.g. immediately after the initial tear and delamination) and/or due to a peeling action created by the flow-induced shear traction on the now delaminated portion of the plaque. Once delamination occurs, it seems that this shear traction will tend to pull the delaminated plaque in the direction of the flow, because the plaque is compliant and the delaminated portion will tend to bend in the flow direction. As such, it is important to understand plaque delamination (dissection) failure in order to develop effective approaches for treatment and intervention.

Abdominal aortic dissection, manifested as delamination and separation of the medial layer of the arterial wall (Fig. 1.1a, the part between blue and red lines), may direct the blood flow into the newly created false lumen, and the blood flow in turn aggregates the delamination in the form of Mode I or mixed-mode failure (Gasser and Holzapfel, 2006; Leng et al., 2015b). Moreover, with the inherent inhomogeneity of the arterial wall along the delamination path, the delaminated medial layer may be peeled from the arterial wall in a mixed-mode manner (Leng et al., 2015b). The failure process inside the media and the resultant damage would trigger aortic dissection which may cause rupture of abdominal aortic aneurysm (Daugherty and Cassis, 2002; Golledge and Norman, 2010; Venkatasubramaniam et al., 2004) and false lumen patency of thoracic descending aorta (Bernard et al., 2001). Numerous studies investigated the dissection behavior of the arterial tissue under Mode I (Ferrara and Pandolfi, 2010; Gasser and Holzapfel, 2006) or mixed-mode conditions between atherosclerotic plaque and the media (Leng et al., 2015b), yet few investigations have focused on comparing the contributions of these two failure modes on the delamination propagation process in the arterial wall (Fig. 1.1c).

Another type of plaque rupture (Fig. 1.1a, red arrow) is often in the form of fibrous cap separation (delamination) from the underlying tissue (Fig. 1.1d). Fibrous cap failure typically occurs at one of two locations. One location is at the center of the plaque, where the fibrous cap may be very thin and prone to rupture under large deformations and stress concentrations. Another is at the shoulder region, where the interface between the fibrous cap and the underlying plaque tissue is located (Jensen et al., 2006; Loree et al., 1992), which is prone to delaminate along the interface. This type of failure occurs, for example, when the atherosclerotic plaque experiences large expansion under balloon angioplasty or

stenting, possibly caused by stress concentration along the interface due to mismatch in mechanical properties (Badel et al., 2014; Kolodgie et al., 2007; Li et al., 2008). For example, fibrous cap delamination at the shoulder region during balloon angioplasty has been demonstrated by intravascular ultrasound in vivo (Honye, 1992). At the site of stress concentration, mechanical damage is expected to initiate and accumulate, leading to delamination when the damage reaches a critical level. In general, the subsequent delamination growth may contain Mode I (opening mode, caused by an opening force) and Mode II (shearing mode, caused by a shearing force) components.

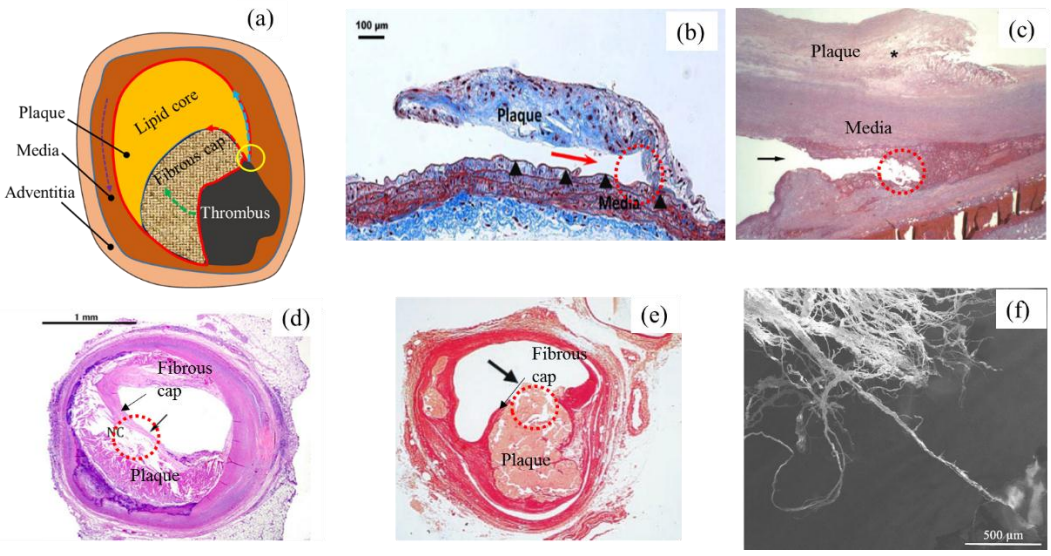


Fig. 1.1 Images of arterial delamination events: (a) A schematic image of a ruptured plaque, with rupture circled; (b) plaque delamination from the underlying media layer (blue arrow) (Wang et al., 2013); (c) delamination within the media layer (Madaloso and Benvenuti, 2013); (d) fibrous cap delamination from the underlying plaque tissue (Tavora et al., 2010); (e) fibrous cap rupture at the at shoulder (red arrow) (Pasterkamp et al., 2000); (f) collagen fibers bridging at a delamination interface in a microscale fiber pullout test.

Furthermore, fibrous cap tearing under Mode I conditions (Fig. 1.1a, green arrow) is one mechanism that leads to plaque rupture. The inflation of a carotid artery with atherosclerotic plaque under balloon angioplasty or stenting will cause extension of the

fibrous cap at the shoulder or middle area (Fig. 1.1e) which may trigger tearing of the fibrous cap through the thickness (Glagov et al., 1997; Richardson et al., 1989; Walraevens et al., 2008). Plaque failure initiation is a very slow process. At the beginning, fibrous cap tissue degradation accumulates due to the cyclic stress from the interaction with blood flow or with a stent within the inner lumen of the artery, which causes micro tearing propagation and stress concentration inside the fibrous cap (Versluis et al., 2006). The mechanical damage is expected to initiate and accumulate, leading to the macro tearing across the total thickness of the fibrous cap. At last, the atherosclerotic plaque will rupture when the damage continues and reaches a critical level (Bentzon et al., 2014). Thus, the material properties or interfacial strength and critical energy release rate across the thickness of the fibrous cap have large effects on the integrity of the atherosclerotic plaque (Leng et al., 2015b; Leng et al., 2016).

Arterial tissue failure may correlate with age-related extracellular matrix remodeling within the aortic wall (London et al., 2004; Sekikawa et al., 2012). This remodeling process is a common potential cause for arterial stiffening, which is related to the development of fatal stroke and heart failure (Graham et al., 2011; Prim et al., 2016). Meanwhile, the age-related aortic remodeling occurs at multiple length scales: at the macroscale, aging aortic diameters and arch length have increased significantly (Lakatta, 2008; Redheuil et al., 2011; Sokolis et al., 2012; Tsamis et al., 2009); at the microscale, the micromechanical remodeling in the aging artery includes: (i) changes in the amount of fibrillar collagen, elastin (Cattell et al., 1993; Tsamis et al., 2013) and subtype of collagen fiber (type I and type III) (Israelowitz et al., 2005; Qiu et al., 2007; Zhou et al., 2014); (ii)

collagen fiber degradation (Ahmann et al., 2010; Driessen et al., 2004; Enderling et al., 2008).

The mechanical properties of arterial tissues at the microscale are essential for determining the failure process in arterial layers. In the references (Leng et al., 2016; Wang et al., 2011), the measured local critical energy release rates of the interface inside arterial walls vary over a wide range, suggesting that the local critical energy release rate depends on the local plaque composition, such as collagen fibers (colorless strands 1 to 100 μm thick (Gentleman et al., 2003; Ushiki, 2002)), which play a crucial role in determining the mechanical behavior of the aortic wall (Yanagisawa et al., 2002; Zhou et al., 2015). These observations suggest that damage accumulation before delamination, oscillations in the force-displacement curve during delamination, and the distribution of the critical energy release rates (Wang et al., 2011) reflect differences in the mechanisms of collagen fiber failure behavior (e.g. collagen fiber pullout and breakage) at the arterial tissue interface.

1.2 Literature Review

Constitutive model for arterial tissue

Fung (Fung, 1967; Fung, 1973) first used an exponential strain energy potential to describe the mechanical behavior of living tissues with nonlinear stress-strain relationship under large deformations. Thereafter, Lanir (Lanir, 1983) introduced fiber dispersion factors in the strain energy based function for the connective tissue. In 1993, a linearly elastic material model was used in the finite element analysis of the concentrations of circumferential tensile stress in the atherosclerotic plaque (Cheng, 1993). Later, to capture the large deformation behavior of human coronary lesions, the isotropic, incompressible, Mooney-Rivlin material model was applied in the evaluation of the impact of calcification

on plaque structural stability (Huang et al., 2001). In order to differentiate contributions from different components of the arterial wall, Holzapfel (Holzapfel and Weizsäcker, 1998) analyzed highly nonlinear biomechanical behavior of the elastic type (abdominal rat aorta) and muscular type (rat artery) of arteries using a classical exponential type material model, which contains an isotropic contribution from the elastin of the arterial wall and an anisotropic contribution from the collagen of the vascular wall. The anisotropic contribution was also characterized by the potential function used in the literature for bio-tissues, which was originally proposed by Fung et al (Fung, 1973; Fung et al., 1979).

In another study by Holzapfel et al. (Holzapfel, 2000b), the artery was modeled as a thick-walled nonlinearly elastic circular tube, in which each arterial layer is treated as a fiber-reinforced material with fibers embedded in a non-collagenous matrix, and the orientations of fibers are obtained from a statistical analysis of histological sections from arterial layers. With the application of this study, Holzapfel (Holzapfel et al., 2002b) first computed the mechanical response of balloon angioplasty with the implementation of a layer-specific three-dimensional model based on *in vitro* magnetic resonance imaging of a human diseased artery. In 2003, Schulze-Bauer and Holzapfel (Schulze-Bauer and Holzapfel, 2003) determined the constitutive equations of human arteries from clinical data based on a two-dimensional Fung-type strain energy function, which characterized nonlinear and anisotropic behavior of arteries. Later, Holzapfel compared the multi-layer structural constitutive model with a three-dimensional form of Fung-type strain-energy function through describing the highly nonlinear and anisotropic characterization of a carotid artery under inflation and extension (Holzapfel et al., 2004a). Meanwhile, Zulliger and Fridez extended a structural model (Holzapfel, 2000b) by adding the wavy nature of

fibers with the fraction of both elastin and collagen and evaluated the new model by fitting experimental data from inflation-extension tests on mouse carotid arteries (Zulliger et al., 2004). Considering the remodeling effects, Hariton proposed a mechanical model by taking into account collagen fiber remodeling for a soft connective tissue. By using this model, the simulation of human common carotid artery fiber morphology correlated well with experimental results (Hariton et al., 2006).

In order to describe the dispersion of collagen fibers in the nonlinear constitutive model, Holzapfel added a dimensionless parameter ρ in an earlier model (Holzapfel, 2000b) to obtain the layer-specific mechanical properties of human coronary arteries (Holzapfel et al., 2005). In a subsequent study by the same authors, a parameter κ was incorporated into the hyperelastic material model to account for the dispersion of collagen fibers in the adventitial and media layers of arterial walls (Gasser et al., 2006), which was widely used in the numerical modeling of arterial tissue deformations. In the work of Li and Robertson, a new fiber strain-based activation criterion was proposed in a nonlinear, anisotropic, multi-mechanism constitutive model, which can be used to capture the mechanical response of cerebral arteries (Li and Robertson, 2009). Based on the previous model, Rodríguez introduced a threshold value for the un-crimped condition of collagen fibers in order to capture the strong stiffness of collagenous tissues (Rodríguez et al., 2008).

The viscoelastic mechanical properties of arterial tissue have been taken into account for modeling the mechanical behaviors of vulnerable arteries in the finite element analysis (Zareh et al., 2015). It has also been shown that the viscoelasticity of arterial tissue plays an important role in the response of arterial wall to vasoactive drugs or pathologies (hypertension and atherosclerosis) (Antonova et al., 2008; Hemmasizadeh et al., 2012).

Meanwhile, quantifying the passive viscoelastic mechanical properties is of great importance to understand the primary determinants of aortic tissue mechanical performance. Understanding the viscoelastic mechanical behavior of the arterial tissue can provide guidelines to evaluate effects of vasoactive medicines and to design appropriate protocols for endovascular interventions.

Viscoelasticity of soft tissues stems from the friction between collagen fibers and the matrix components (e.g., smooth muscle cells and elastin); from the friction from the movement and permeation of water molecules between these matrix components and fibers (Screen, 2008); and from the viscoelastic response of isolated collagen fibrils (Shen et al., 2011). Numerous biomechanical investigations have been focused on characterizing the viscoelastic mechanical properties of native and fabricated arterial tissues. A viscoelastic algorithm with the generalized Maxwell model, containing a free spring on one end and an arbitrary number of dashpot elements arranged in parallel, was incorporated into the hyperelastic model and implemented to predict the hysteresis of arterial tissues (Holzapfel, 2000a; Holzapfel, 2003; Holzapfel, 2000b). Based on the previous studies, a viscoelastic model was proposed to simulate the 'stretch inversion phenomenon' in the low pressure range and to illustrate the anisotropic viscoelastic mechanical characteristics of a fiber-reinforced composite material (Holzapfel and Gasser, 2001), leading to a viscoelastic anisotropic (VA) model (Gasser et al., 2006; Holzapfel, 2000a). Another transversely isotropic and hyperelastic material combined with a Kelvin-Voigt linear viscous model was proposed to characterize the viscoelastic mechanical responses of native and fabricated biological tissues (Peña et al., 2007; Weiss et al., 1996). Moreover, at the micro-scale level, the generalized Maxwell model was used to characterize the viscoelastic mechanical

behaviors of three-dimensional biopolymer networks (Unterberger et al., 2013). A structure-motivated viscoelastic constitutive model of the soft tissue is required to calculate the local stress environment of resident vascular cells and to fully understand the mechanical implications of both vascular injury and clinical intervention.

Cohesive zone model

The cohesive zone model (CZM) is an effective method to solve fracture problems in homogeneous and composite materials and can be implemented in finite element codes. Barrenblatt (Barenblatt, 1959) and Dugdale (Dugdale, 1960) first introduced the concept of CZM. With this idea, Needleman (Needleman, 1987) developed a polynomial CZM to solve the debonding problem of rigid spherical inclusions in a metal matrix and also to analyze the initiation and decohesion along interfaces (Needleman, 1990). In 1990, Tvergaard (Tvergaard, 1990) used a quadratic traction-separation CZM model to analyze the decohesion of the fiber-matrix interface which described the failure with normal and tangential separations. Later, he and Hutchinson (Tvergaard and Hutchinson, 1992) developed a trapezoidal CZM to predict the toughness and interface plasticity of void growth and coalescence processes in order to illuminate the enhancement effect of plasticity to dual-phase solids. For another type of CZM, Xu and Needleman (Xu and Needleman, 1993) implemented the polynomial separation CZM to do the numerical micromechanical study of inclusion debonding in a crystal matrix, which investigated the occurrence of decohesion or localization determined by the triaxial stress state. Thereafter, Camacho and Ortiz (Camacho and Ortiz, 1996) used a CZM with a bilinear tensile cohesive relation to predict the propagation of multiple cracks along arbitrary paths in brittle materials. It is noted that the bilinear CZM is widely used for modeling material failure

processes. Geubelle and Baylor (Geubelle and Baylor, 1998) applied this CZM to conduct an investigation of the delamination process in thin composite plates under low-velocity impact conditions, which had the ability to capture complex delamination events including micro-cracking of the matrix and delamination propagation. Using the same type of CZM, Ortiz (Ortiz and Pandolfi, 1999) developed an irreversible cohesive law to track dynamically growing cracks in steels using three-dimensional cohesive elements.

The cohesive zone model (CZM) has been proven to be an effective way of modeling delamination failure in composite materials (Turon et al., 2006). The CZM approach has also been used to understand the mechanism of arterial tissue failure. Gasser and Holzapfel (Gasser and Holzapfel, 2006) combined CZM with the partition of unity finite element method to study the dissection failure of a rectangular tissue strip of aorta wall. Later, they used the same method to investigate plaque fissuring and dissection in atherosclerosis-prone human iliac arteries under balloon angioplasty conditions. The results indicated that the localized trauma caused by plaque fissuring and dissection can prevent the continuous tissue failure around the stenosis where high stress occurred (Gasser and Holzapfel, 2007). Considering the anisotropic characteristics of arterial tissue, Ferrara and Pandolfi (Ferrara and Pandolfi, 2010) developed an anisotropic CZM to predict dissection in the medial layer of an aorta, which provided an effective model to describe damage events such as intramural dissection and plaque rupture. In order to perform parametric analyses of the arterial tissue dissection behavior, Badel et al. (Badel et al., 2014) used a CZM with an exponential softening process to study dissection events in an atherosclerotic coronary artery during the early stages of balloon angioplasty treatments using a two-dimensional finite element model. The results showed that the initiation of

dissection damage happened very early, which is important for understanding this clinical event.

In the current study, atherosclerotic plaque delamination is considered as analogous to the common delamination damage phenomenon between layers in laminated composites, and thus the CZM approach seems applicable. To the author's knowledge, the CZM approach has not been applied in the literature to the study of plaque delamination. While the CZM has been widely used in the studies of fracture failures in engineering materials, the use of CZM in the studies of failures in arterial materials has been very limited. Thus, CZM-based three-dimensional finite element models are needed to better understand arterial tissue failure events.

For the implementation of CZMs to simulate the micromechanical failure process of composite materials, Difrancia et al. (DiFrancia et al., 1996) reviewed the test methodologies, the experimental and theoretical discussion on the single fiber pull-out test in order to interpret the failure of fiber-reinforced composite materials. Later, Chandra et al. (Chandra et al., 2002) implemented exponential and bilinear CZMs to simulate the single fiber push-out test, and the simulation predictions matched well with experimental data. It is found that the shape of the CZM cohesive law depends on the nonlinear mechanical response at the micromechanical level and on the material properties of the CZM such as the interfacial strength, critical energy release rate and maximum separation. These parameters have large effects on the loading and unloading behaviors of the fiber push-out process.

In order to study the effects of collagen fiber bridging on the arterial tissue failure process, the mechanical behavior of collagen fibers in arterial tissues needs to be

investigated. To this end, a method based on AFM was performed on a single tow of collagen fibrils isolated from collagenous materials, in order to quantify the Young's modulus (van der Rijt et al., 2006; Yang et al., 2007), and the bending and shear moduli (Yang et al., 2008). Another method using nanoindentation by AFM was conducted on a single tow of collagen fibrils to acquire the reduced modulus, which provides new insights into the collagen structure. The yield stress and strain at failure of collagen fibrils from sea cucumber were obtained through uniaxial tensile testing (Shen et al., 2008). In the studies of individual collagen fibers, Kato et al. (Kato et al., 1989) performed tensile tests on collagen fibers from rat tail tendons to obtain the tensile strengths. Miyazaki and Hayashi (Miyazaki and Hayashi, 1999) acquired the modulus, tensile strength and strain at failure through uniaxial tensile tests of collagen fibers from rat tail tendons. Moreover, the modulus, tensile strength and strain at failure of collagen fascicles from the rabbit patellar tendon were quantified by tensile testing (Yamamoto et al., 1999). However, these studies do not provide all mechanical properties such as the modulus and adhesive strength of bundles of collagen fibers from arterial wall. Therefore, experimental and numerical studies of collagen fiber failure processes are required to characterize the arterial tissue failure mechanism.

1.3 Research Objectives

The current dissertation is aimed at investigating the applicability of the CZM-based approach in simulating plaque rupture (peeling tests of mouse atherosclerotic plaques and human fibrous cap, etc.) and related failure events. Three types of CZMs and the HGO model (or VA model for describing the hysteresis phenomenon) will be employed in the CZM-based approach to simulate the delamination and tearing of arterial tissue using 3D

finite element models. Simulation predictions will be compared with experimental measurements in order to validate the CZM-based approach.

This study will provide a quantification of delamination modes in the arterial delamination events by analyzing and comparing two types of delamination experiments ("mixed-mode" and "Mode I" delaminations). In particular, the CZM approach will be validated through comparisons of the load-displacement curve and the distances from the delamination front to the initial front, between simulation predictions and experimental measurements. Results of the current study can offer guidance for arterial tissue delamination tests and insights into the arterial layer delamination events.

The current study will estimate the CZM parameter values of interfaces across the thickness of human fibrous caps through an inverse analysis procedure. With the simulation prediction from the inverse analysis, the mechanism of fibrous cap Mode I tearing will be explored.

Finally, the study will develop a 3D unit cell model to study the arterial tissue failure mechanisms at the microscopic scale. With the input parameter values obtained from tensile tests of collagen fibers harvested from an arterial tissue, the factors at the micromechanical scale affecting the cohesive traction-separation relation of the unit cell model will be investigated.

1.4 Outline of the Dissertation

The current dissertation contains nine chapters. The subsequent chapters are outlined as follows.

Chapter 2 presents the Holzapfel-Gasser-Ogden (HGO) model (a fiber-reinforced hyperelastic model), and a Viscoelastic Anisotropic (VA) model which was extended from the HGO model. These models will be used to characterize the bulk material behavior of arterial tissue or to capture the hysteresis phenomenon of diseased aortic tissue in the simulations from Chapter 4 to Chapter 8.

Chapter 3 focuses on the derivation of three types of cohesive zone models, including the exponential, triangular and trapezoidal CZMs, which describe the relationship between the cohesive traction and the separation across a material interface. These CZM models will used in the simulations from Chapter 4 to Chapter 8.

Chapter 4 describes the procedure to determine and validate HGO and CZM parameter values using experimental measurements of the load vs. load-point displacement curve in the atherosclerotic plaque delamination experiments in mouse abdominal aorta specimens. In addition, the effects of geometric uncertainty on simulation predictions will be discussed.

Chapter 5 first presents the mixed-mode and mode I delamination experiments of porcine aorta and quantifies the critical energy release rates in the media layer, and then compares simulation predictions of the load-displacement curve and the delamination front with experimental measurements. In addition, the ratio of mode I to mode II components in these experiments will be studied. These studies will provide a basis for subsequent arterial tissue delamination tests and simulation predictions.

Chapter 6 identifies the VA model and CZM parameter values through the same procedure as described in Chapter 4, and validates the applicability of the viscoelastic

anisotropic model and the CZM approach for the simulation of diseased arterial tissue failure processes.

Chapter 7 employs an inverse analysis procedure to identify the CZM parameter values of the interface across the thickness of human fibrous cap by matching the simulation predictions of load-displacement curves with experimental measurements of the human fibrous cap mode I tearing tests. Furthermore, the failure mechanism of fibrous cap mode I tearing will be investigated through numerical simulations.

Chapter 8 introduces a micromechanical model describing arterial delamination mechanics at the fibrous cap-underlying plaque tissue interface. A 3D unit cell containing an individual fiber between two arterial tissue material layers is considered. With the unit cell model, micromechanical factors affecting the resulting traction-separation relation of the unit cell will be investigated using a parametric approach.

Chapter 9 concludes the current work.

CHAPTER 2

ANISOTROPIC HYPERELASTIC MODEL FOR ARTERIAL MATERIAL

2.1 Introduction

In the current study, the Holzapfel-Gasser-Ogden (HGO) model (Gasser et al., 2006) was initially considered to provide a hyper-elastic constitutive law for the bulk material behavior of all arterial layers. The HGO model is commonly employed for arterial walls. It treats each artery layer as a fiber-reinforced material with the fibers symmetrically disposed with respect to the circumferential direction of the artery. However, this model was not able to capture the hysteresis behavior observed in the load-displacement curves obtained from the fibrous cap delamination experiments (section 6.2), because there is no viscoelastic component in the HGO model. To extend the HGO model, a viscoelasticity formulation developed by Holzapfel (Holzapfel, 2000a) was adopted in the current study to incorporate a viscoelastic component into the HGO model, leading to a viscoelastic anisotropic (VA) model, which is used in the current study.

To describe the mechanical behavior of diseased arterial materials such as atherosclerotic plaque and fibrous cap, a viscoelastic, anisotropic material model extended from the HGO model (Gasser et al., 2006) (which does not have a viscoelastic component) is proposed, so that the hysteresis behavior seen in the loading-delamination-unloading data from the fibrous cap delamination experiments can be captured.

For convenience of easy reference, the HGO model, its extension to include a viscoelastic component, and some associated concepts are briefly described below.

2.2 Anisotropic Hyperelastic Model: Holzapfel-Gasser-Ogden (HGO) Model

The HGO model (Gasser et al., 2006) assumes that the mean orientation of collagen fibers lies parallel to the arterial wall (as shown in Fig. 2.1), thus neglecting the out-of-plane component. A Helmholtz free energy function $\Psi(\overline{\boldsymbol{C}}, \boldsymbol{H}_1, \boldsymbol{H}_2)$ which is defined per unit reference volume in a decoupled form is expressed as:

$$\Psi(\boldsymbol{C}, \boldsymbol{H}_1, \boldsymbol{H}_2) = \Psi_{vol}(J) + \overline{\Psi}(\overline{\boldsymbol{C}}, \boldsymbol{H}_1, \boldsymbol{H}_2) \tag{2.1}$$

In the above equation, $\boldsymbol{C}$ is the right Cauchy-Green strain tensor, and $\overline{\boldsymbol{C}}$ denotes a modified version of $\boldsymbol{C}$, $\overline{\boldsymbol{C}} = \overline{\boldsymbol{F}}^T\overline{\boldsymbol{F}}$ with $\overline{\boldsymbol{F}} = J^{-1/3}\boldsymbol{F}$, where $\boldsymbol{F}$ is the deformation gradient, and $J = \det(\boldsymbol{F})$. The volumetric part, $\Psi_{vol}(J)$, as given in (ABAQUS, 2013) is

$$\Psi_{vol}(J) = \frac{1}{D}\left(\frac{J^2-1}{2} - \ln J\right) \tag{2.2}$$

where $\frac{1}{D}$ is analogous to the bulk modulus of the material.

The potential $\overline{\Psi}(\overline{\boldsymbol{C}}, \boldsymbol{H}_1, \boldsymbol{H}_2)$ can be represented by a superposition of an isochoric potential $\overline{\Psi}_g(\overline{\boldsymbol{C}})$ for the non-collagenous ground-matrix (indicated by subscript 'g'), which accounts for the material behavior with no fibers, and two transversely isochoric potentials $\overline{\Psi}_{f1}$ and $\overline{\Psi}_{f2}$, which represent the two families of collagen fibers (with subscript 'f'), respectively. Hence, the free-energy function $\overline{\Psi}$ is expressed as

$$\overline{\Psi}(\overline{\boldsymbol{C}}, \boldsymbol{H}_1, \boldsymbol{H}_2) = \overline{\Psi}_g(\overline{\boldsymbol{C}}) + \left[\overline{\Psi}_{f1}\left(\overline{\boldsymbol{C}}, \boldsymbol{H}_1(\boldsymbol{a}_{01}, \kappa)\right) + \overline{\Psi}_{f2}\left(\overline{\boldsymbol{C}}, \boldsymbol{H}_2(\boldsymbol{a}_{02}, \kappa)\right)\right] \tag{2.3}$$

In the above, $\boldsymbol{H}_1, \boldsymbol{H}_2$ are two structure tensors depending on the direction vectors $\boldsymbol{a}_{01}$ and $\boldsymbol{a}_{02}$,

$$\boldsymbol{H}_1(\boldsymbol{a}_{01}, \kappa) = \kappa \boldsymbol{I} + (1 - 3\kappa)(\boldsymbol{a}_{01} \otimes \boldsymbol{a}_{01}) \tag{2.4}$$

$$\boldsymbol{H}_2(\boldsymbol{a}_{02}, \kappa) = \kappa \boldsymbol{I} + (1 - 3\kappa)(\boldsymbol{a}_{02} \otimes \boldsymbol{a}_{02}) \tag{2.5}$$

where $\boldsymbol{I}$ is the identity tensor; κ is the dispersion parameter, which characterizes the dispersion of the two families of fibers along the two mean distributed directions, and $0 \leq \kappa \leq 1/3$; the collagen fibers of one family of fibers are parallel to each other when $\kappa = 0$, whereas the fibers distribute isotropically when $\kappa = 1/3$. The two vectors $\boldsymbol{a}_{01}$ and $\boldsymbol{a}_{02}$ have the following matrix forms in a rectangular coordinate system (as shown in Fig. 2.1):

$$[\boldsymbol{a}_{01}] = \begin{bmatrix} cosr \\ sinr \\ 0 \end{bmatrix}, [\boldsymbol{a}_{02}] = \begin{bmatrix} cosr \\ -sinr \\ 0 \end{bmatrix} \tag{2.6}$$

where r represents the angle between the mean fiber orientation of one family of fibers and the circumferential direction of the artery, as shown in Fig. 2.1.

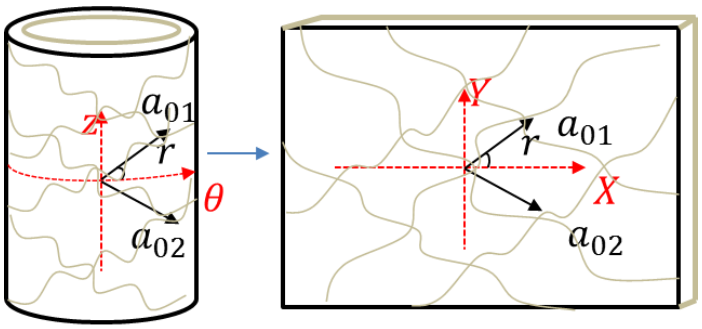


Fig. 2.1 Arterial tube with helicoidal arrangement of two families of fibers in cylindrical and rectangular coordinate systems. The two direction vectors $\boldsymbol{a}_{01}$ and $\boldsymbol{a}_{02}$ are tangent to the fiber directions and $2r$ is the angle between $\boldsymbol{a}_{01}$ and $\boldsymbol{a}_{02}$.

An incompressible isotropic Neo-Hookean model has been used to denote the response of the non-collagenous ground-matrix. Thus,

$$\bar{\Psi}_g(\bar{\boldsymbol{C}}) = \frac{\mu}{2}(\bar{I}_1 - 3) \tag{2.7}$$

In the above, $\bar{I}_1 = tr(\bar{\boldsymbol{C}})$ denotes the first invariant of $\bar{\boldsymbol{C}}$, and μ is the neo-Hookean parameter, which characterizes the shear modulus of the material without fibers. The mechanical behavior of the two families of collagen fibers is represented by the following transversely isotropic free-energy functions

$$\bar{\Psi}_{f1}\big(\bar{\boldsymbol{C}}, \boldsymbol{H}_1(\boldsymbol{a}_{01}, \kappa)\big) = \frac{k_1}{2k_2}\left[e^{k_2[\mathrm{tr}(\boldsymbol{H}_1\bar{\boldsymbol{C}})-1]^2} - 1\right] \tag{2.8}$$

$$\bar{\Psi}_{f2}\big(\bar{\boldsymbol{C}}, \boldsymbol{H}_2(\boldsymbol{a}_{02}, \kappa)\big) = \frac{k_1}{2k_2}\left[e^{k_2[\mathrm{tr}(\boldsymbol{H}_2\bar{\boldsymbol{C}})-1]^2} - 1\right] \tag{2.9}$$

$$\mathrm{tr}(\boldsymbol{H}_1\bar{\boldsymbol{C}}) = \kappa\bar{I}_1 + (1-3\kappa)\bar{I}_{41} \;;\; \mathrm{tr}(\boldsymbol{H}_2\bar{\boldsymbol{C}}) = \kappa\bar{I}_1 + (1-3\kappa)\bar{I}_{42} \tag{2.10}$$

where $\bar{I}_{41} = \boldsymbol{a}_{01}\cdot\bar{\boldsymbol{C}}\boldsymbol{a}_{01}$ and $\bar{I}_{42} = \boldsymbol{a}_{02}\cdot\bar{\boldsymbol{C}}\boldsymbol{a}_{02}$ are tensor invariants equal to the square of the stretch in the directions of $\boldsymbol{a}_{01}$ and $\boldsymbol{a}_{02}$, respectively. Finally, according to relations (2.7), (2.8) and (2.9), we obtain

$$\bar{\Psi}(\bar{\boldsymbol{C}}, \boldsymbol{H}_1, \boldsymbol{H}_2) = \frac{\mu}{2}(\bar{I}_1 - 3) + \frac{k_1}{2k_2}\left[e^{k_2[\kappa\bar{I}_1+(1-3\kappa)\bar{I}_{41}-1]^2} - 1\right] +$$

$$\frac{k_1}{2k_2}\left[\mathrm{e}^{k_2[\kappa\bar{I}_1+(1-3\kappa)\bar{I}_{42}-1]^2} - 1\right] \tag{2.11}$$

Note that constitutive parameter k_1 is related to the relative stiffness of the fibers, which is determined from mechanical tests of arterial tissues; and k_2 is a dimensionless stiffness parameter.

2.3 Stress Tensors

To prepare for the introduction of a viscoelastic anisotropic material model by extending the HGO model with the addition of a viscoelastic component, in the following the superscript "∞" will be used to signify stress quantities derived from the HGO model.

In particular, the second Piola-Kirchhoff stress can be derived from the Clausius-Planck inequality and given by:

$$\boldsymbol{S}^{\infty} = \boldsymbol{S}^{\infty}_{vol} + \boldsymbol{S}^{\infty}_{iso} \tag{2.12}$$

$$\boldsymbol{S}^{\infty} = 2\frac{\partial \Psi(\boldsymbol{C},\boldsymbol{H}_1,\boldsymbol{H}_2)}{\partial \boldsymbol{C}}, \boldsymbol{S}^{\infty}_{vol} = 2\frac{\partial \Psi_{vol}(J)}{\partial \boldsymbol{C}}, \boldsymbol{S}^{\infty}_{iso} = 2\frac{\partial \overline{\Psi}(\overline{\boldsymbol{C}},\boldsymbol{H}_1,\boldsymbol{H}_2)}{\partial \boldsymbol{C}} \tag{2.13}$$

The partial derivative of local volume ratio J and the modified right Cauchy-Green tensor $\overline{\boldsymbol{C}}$ to $\boldsymbol{C}$ are obtained by using the chain rule:

$$\frac{\partial J}{\partial \boldsymbol{C}} = \frac{1}{2}J\boldsymbol{C}^{-1}, \quad \frac{\partial \overline{\boldsymbol{C}}}{\partial \boldsymbol{C}} = J^{-2/3}\left(\mathbb{I} - \frac{1}{3}\boldsymbol{C}\otimes\boldsymbol{C}^{-1}\right) \tag{2.14}$$

In the above, $\mathbb{I}$ is the fourth order identity tensor, which has the form below in indicial notation (Holzapfel, 2000a)

$$(\mathbb{I})_{\mathrm{IJKL}} = \frac{\delta_{IK}\delta_{JL}+\delta_{IL}\delta_{JK}}{2} \tag{2.15}$$

where δ_{IK} is the Kronecker delta.

With the associated property in the first equation in (2.14), the volumetric part of the second Piola-Kirchhoff stress has the form:

$$\boldsymbol{S}^{\infty}_{vol} = 2\frac{\partial \Psi_{vol}(J)}{\partial \boldsymbol{C}} = pJ\boldsymbol{C}^{-1} \tag{2.16}$$

where p is the hydrostatic pressure (Holzapfel, 2000b)

$$p = \frac{d\Psi_{vol}(J)}{dJ} = \frac{1}{D}\left(J - \frac{1}{J}\right) \tag{2.17}$$

According to the second equation in (2.14), the isochoric part of the ground matrix of the arterial material is expressed as:

$$\boldsymbol{S}_{g}^{\infty} = 2\frac{\partial \bar{\Psi}_g(\bar{\boldsymbol{C}})}{\partial \boldsymbol{C}} = J^{-2/3}\mathbb{P}: \mu \boldsymbol{I} \tag{2.18}$$

where $\mathbb{P}$ is the projection tensor which has the form:

$$\mathbb{P} = \mathbb{I} - \frac{1}{3}\boldsymbol{C}^{-1} \otimes \boldsymbol{C} \tag{2.19}$$

With the associated property in the second equation in (2.14), the isochoric part used to describe the behavior of the two families of fibers is given by

$$\boldsymbol{S}_{fi}^{\infty} = 2\frac{\partial \bar{\Psi}_{fi}}{\partial \boldsymbol{C}} = J^{-2/3}\mathbb{P}: 2k_1 e^{k_2 \bar{E}_i^{\,2}} \bar{E}_i \boldsymbol{H}_i \tag{2.20}$$

where $\bar{E}_i$ $(i = 1, 2)$ are the structure strain invariants and $\bar{\boldsymbol{h}}_i$ $(i = 1, 2)$ are the modified structure tensors which can be expressed by

$$\bar{E}_i = \mathrm{tr}\bar{\boldsymbol{h}}_i - 1 \tag{2.21}$$

$$\bar{\boldsymbol{h}}_i = \kappa \bar{\boldsymbol{b}} + (1 - 3\kappa)(\bar{\boldsymbol{a}}_i \otimes \bar{\boldsymbol{a}}_i) \tag{2.22}$$

where $\bar{\boldsymbol{b}}$ denotes the modified left Cauchy-Green strain tensor, $\bar{\boldsymbol{b}} = \bar{\boldsymbol{F}}\bar{\boldsymbol{F}^T}$; $\bar{\boldsymbol{a}}_i = \bar{\boldsymbol{F}}\boldsymbol{a}_{0i}$ $(i = 1, 2)$ represents the push-forward of $\boldsymbol{a}_{0i}$ through tensor $\bar{\boldsymbol{F}}$.

Considering the relations (2.16) , (2.18) and (2.20), the second Piola-Kirchhoff stress can be written as (Holzapfel, 2000a):

$$\boldsymbol{S}^{\infty} = \boldsymbol{S}_{vol}^{\infty} + \boldsymbol{S}_{iso}^{\infty} = \boldsymbol{S}_{vol}^{\infty} + \boldsymbol{S}_{g}^{\infty} + \sum_{i=1}^{2} \boldsymbol{S}_{fi}^{\infty} =$$

$$pJ\boldsymbol{C}^{-1} + J^{-2/3}\mathbb{P}: \mu \boldsymbol{I} + \sum_{i=1}^{2} \left[J^{-2/3}\mathbb{P}: \left(2\mathrm{k}_1 \mathrm{e}^{\mathrm{k}_2 \bar{E}_i^{\,2}} \bar{E}_i \boldsymbol{H}_i \right) \right] \tag{2.23}$$

2.4 Elasticity Tensors

It is noted that the derivation of the elasticity tensors for the hyperelastic constitutive law of the HGO model is important for its implementation in the general-purpose finite element code ABAQUS (ABAQUS, 2013) via its user subroutine option. The closed-form elasticity tensor $\mathbb{C}$ is defined through $\mathbb{C} = 2\frac{\partial \boldsymbol{S}^{\infty}}{\partial \boldsymbol{C}}$, which can be determined by following the process described in (Holzapfel, 2000a), and is denoted in the decoupled form below:

$$\mathbb{C}^{\infty} = \mathbb{C}^{\infty}_{vol} + \mathbb{C}^{\infty}_{iso} \tag{2.24}$$

$$\mathbb{C}^{\infty}_{iso} = \bar{\mathbb{C}}^{\infty}_{g} + \bar{\mathbb{C}}^{\infty}_{f} \tag{2.25}$$

In the current study, the volumetric part $\mathbb{C}^{\infty}_{vol}$ and the isochoric part $\mathbb{C}^{\infty}_{iso}$ of the elasticity tensor (the tangent modulus tensor) are obtained using the approximate expressions (A.6) described in ***Appendix A***.

2.5 Viscoelastic Anisotropic (VA) Model

In the current study, a Viscoelastic Anisotropic (VA) model for arterial materials is extended from the HGO model (Gasser et al., 2006) by introducing a viscoelastic component into the HGO model. This is done by employing a viscoelasticity formulation developed by Holzapfel (Holzapfel, 2000a). According to this formulation, a VA model can be built upon the HGO model by adding a strain-energy function term in Eq. (2.1). This additional term represents the dissipative potential responsible for the viscoelastic contribution. Based on this formulation, the second Piola-Kirchhoff stress tensor of the AV model $\boldsymbol{S}_{n+1}$ at time t_{n+1} can be written as:

$$\boldsymbol{S}_{n+1} = \left(\boldsymbol{S}^{\infty}_{vol} + \boldsymbol{S}^{\infty}_{iso} + \sum_{\alpha=1}^{m} \boldsymbol{Q}_{\alpha}\right)_{n+1} \tag{2.26}$$

where the superscript "∞" denotes the equilibrium condition when the time approaches infinity. The first and second terms with the superscript "∞" in Eq. (2.26) are contributions from the HGO model (see Eq. (2.12)), and the third term in Eq. (2.26) describes the viscoelastic contribution to the stress state.

The non-equilibrium stress tensor $\boldsymbol{Q}_{\alpha\, n+1}$ at time t_{n+1} is expressed as

$$\boldsymbol{Q}_{\alpha\, n+1} = \boldsymbol{\mathcal{H}}_{\alpha\, n} + \beta_{\alpha}\, exp\left(-\frac{\Delta t}{2T_{\alpha}}\right)\left(\boldsymbol{S}^{\infty}_{iso}\right)_{n+1} \tag{2.27}$$

where the history term is defined as:

$$\boldsymbol{\mathcal{H}}_{\alpha\, n} = exp\left(-\frac{\Delta t}{2T_{\alpha}}\right)\left[exp\left(-\frac{\Delta t}{2T_{\alpha}}\right)\boldsymbol{Q}_{\alpha\, n} - \beta_{\alpha}\left(\boldsymbol{S}^{\infty}_{iso}\right)_{n}\right] \tag{2.28}$$

In the above equations, Δt is the time increment from time t_n to t_{n+1}; T_{α} ($\alpha = 1, \ldots, m$) is the relaxation time and β_{α} is a non-dimensional parameter. The viscoelastic parameters T_{α} and β_{α} ($\alpha = 1, \ldots, m$) correspond to the parameters in a generalized Maxwell model for one-dimensional viscoelasticity (Rajesh, 2000) with m Maxwell elements (see Fig. 2.2).

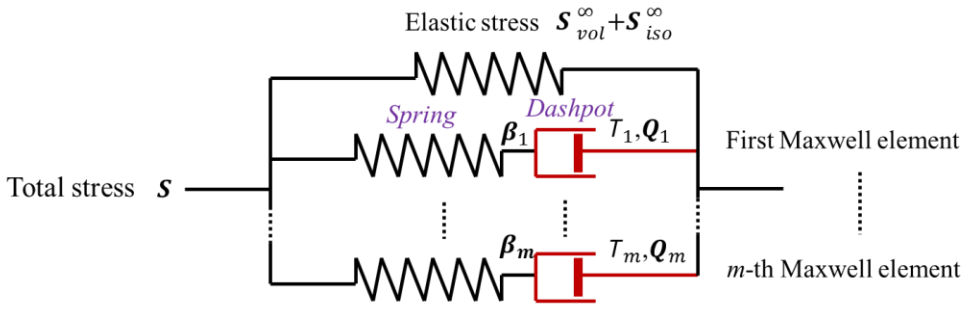


Fig. 2.2 Schematic model of a viscoelastic material (Unterberger et al., 2013).

The corresponding viscous part $(\mathbb{C}_{vis})_{n+1}$ of the elasticity tensor at time t_{n+1} is

$$(\mathbb{C}_{vis})_{n+1} = (\mathbb{C}^{\infty}_{iso})_{n+1} \sum_{\alpha=1}^{m} \beta_{\alpha}\, exp\left(-\frac{\Delta t}{2T_{\alpha}}\right) \tag{2.29}$$

and the total elasticity tensor at time t_{n+1} is

$$(\mathbb{C})_{n+1} = \left[\mathbb{C}^{\infty}_{vol} + \left\{1 + \sum_{\alpha=1}^{m} \beta_{\alpha}\, exp\left(-\frac{\Delta t}{2T_{\alpha}}\right)\right\} \mathbb{C}^{\infty}_{iso}\right]_{n+1} \tag{2.30}$$

Table 2.1 below provides a concise summary of the procedure and associated quantities involved in the VA model for implementation in ABAQUS via a user material subroutine.

In the current study, finite element simulation results show that it is sufficient to use only one viscoelastic term (i.e. m=1 in Eq. (2.26) and subsequent equations) in the VA model to capture the essential hysteresis behavior observed in the fibrous cap delamination experiments (additional terms do not improve the results significantly). Thus, the only viscoelastic parameters involved in the simulations described subsequently are T_1 and β_1.

The nonlinear static analysis option in ABAQUS/Standard (ABAQUS, 2013) with implicit time integration was employed to carry out the fibrous cap delamination simulations. The tangential modulus tensor that is implemented in this study in the ABAQUS user UMAT subroutine can be found in ***Appendix A***.

Table 2.1 Summary of the procedure for creating an efficient user material subroutine implemented in ABAQUS

The deformation gradient of solid elements is provided at the beginning of each increment, $\boldsymbol{F}$

A unimodular distortional part of $\boldsymbol{F}$, $\overline{\boldsymbol{F}} = J^{-1/3}\boldsymbol{F}, J = \det\boldsymbol{F}$

Modified counterparts of Cauchy-Green tensors $\boldsymbol{b}$, $\overline{\boldsymbol{b}} = \overline{\boldsymbol{F}}\overline{\boldsymbol{F}}^{\mathrm{T}}$

Structure tensors

$$\boldsymbol{H}_i = \kappa\boldsymbol{I} + (1-3\kappa)(\boldsymbol{a}_{0i}\otimes\boldsymbol{a}_{0i})$$
$$\overline{\boldsymbol{h}}_i = \kappa\overline{\boldsymbol{b}} + (1-3\kappa)(\overline{\boldsymbol{a}}_i\otimes\overline{\boldsymbol{a}}_i),\ \overline{\boldsymbol{a}}_i = \overline{\boldsymbol{F}}\boldsymbol{a}_{0i}$$

Structure strain invariants

$$\bar{E}_i = \mathrm{tr}\overline{\boldsymbol{h}}_i - 1 = \mathrm{tr}\left(\kappa\overline{\boldsymbol{b}}\right) + (1-3\kappa)\mathrm{tr}(\overline{\boldsymbol{a}}_i\otimes\overline{\boldsymbol{a}}_i) - 1$$

Stress tensor

$$\boldsymbol{S}_g^{\infty} = J^{-2/3}\mathbb{P}:\mu\boldsymbol{I}\ ,\ \boldsymbol{S}_{fi}^{\infty} = J^{-2/3}\mathbb{P}:2k_1e^{k_2\bar{E}_i^2}\bar{E}_i\boldsymbol{H}_i\ ,\ \boldsymbol{S}_{vol}^{\infty} = pJ\boldsymbol{C}^{-1}$$
$$\boldsymbol{S}_{iso}^{\infty} = \boldsymbol{S}_g^{\infty} + \sum_{i=1}^{2}\boldsymbol{S}_{fi}^{\infty}$$
$$\mathbb{P} = \mathbb{I} - \frac{1}{3}\boldsymbol{C}^{-1}\otimes\boldsymbol{C}$$

The second Piola-Kirchhoff stress tensor $\boldsymbol{S}_{n+1}$ at time t_{n+1}

$$\boldsymbol{S}_{n+1} = \left(\boldsymbol{S}_{vol}^{\infty} + \boldsymbol{S}_{iso}^{\infty} + \sum_{\alpha=1}^{m}\boldsymbol{Q}_{\alpha}\right)_{n+1}$$

The Cauchy stress tensor $\boldsymbol{\sigma}_{n+1}$ at time t_{n+1}

$$\boldsymbol{\sigma}_{n+1} = (J^{-1}\boldsymbol{F}\boldsymbol{S}\boldsymbol{F}^{T})_{n+1}$$

The current non-equilibrium stress tensor $\boldsymbol{Q}_{\alpha\,n+1}$ at time t_{n+1}

$$\boldsymbol{Q}_{\alpha\,n+1} = \boldsymbol{\mathcal{H}}_{\alpha\,n} + \beta_\alpha\, exp\left(-\frac{\Delta t}{2T_\alpha}\right)\left(\boldsymbol{S}_{iso}^{\infty}\right)_{n+1}$$

where the history term is defined as:

$$\boldsymbol{\mathcal{H}}_{\alpha\,n} = exp\left(-\frac{\Delta t}{2T_\alpha}\right)\left[exp\left(-\frac{\Delta t}{2T_\alpha}\right)\boldsymbol{Q}_{\alpha\,n} - \beta_\alpha\left(\boldsymbol{S}_{iso}^{\infty}\right)_n\right]$$

The viscous part $(\mathbb{C}_{vis})_{n+1}$ of the elasticity tensor at time t_{n+1} is

$$(\mathbb{C}_{vis})_{n+1} = (\mathbb{C}_{iso}^{\infty})_{n+1}\sum_{\alpha=1}^{m}\beta_\alpha\, exp\left(-\frac{\Delta t}{2T_\alpha}\right)$$

The elastic tensor at time t_{n+1} is

$$(\mathbb{C})_{n+1} = \left[\mathbb{C}_{vol}^{\infty} + \left\{1 + \sum_{\alpha=1}^{m}\beta_\alpha\, exp\left(-\frac{\Delta t}{2T_\alpha}\right)\right\}\mathbb{C}_{iso}^{\infty}\right]_{n+1}$$

2.6 Conclusions

The Holzapfel-Gasser-Ogden constitutive model which aims to describe the basic mechanical response of aortic tissue was introduced at the beginning of this chapter. In

order to capture the viscoelastic effect of the diseased arterial material, a Maxwell model was incorporated in the HGO model. With the derivation of stress tensors and elasticity tensors, the process for developing the user UMAT subroutine in ABAQUS was presented.

CHAPTER 3

INTERFACE DAMAGE MODEL

3.1 Introduction

As a novel method for the simulation of soft tissue failure, an efficient and robust interface damage model formulation is important for the simulation of arterial tissue failure. Hence, a mixed-mode cohesive zone model is introduced at the begging of this chapter. Furthermore, three types of cohesive zone models are considered, which include the exponential, triangular and trapezoidal CZMs. These models are developed with the same parameters and implemented in the commercial finite element code ABAQUS through a user UEL subroutine.

3.2 Interface Cohesive Element

The nodal coordinates of the undeformed interface element is given by (Y. Arun Roy, 2001)

$$\boldsymbol{P} = \{X_1, Y_1, Z_1, \dots, X_8, Y_8, Z_8\} \tag{3.1}$$

where (X_j, Y_j, Z_j) is the coordinate of the j-th node. According to Fig. 3.1, the vector $\boldsymbol{P}$ can be written as

$$\boldsymbol{P}^- = \{X_1, Y_1, Z_1, \dots, X_4, Y_4, Z_4\}^T,\ \boldsymbol{P}^+ = \{X_5, Y_5, Z_5, \dots, X_8, Y_8, Z_8\}^T \tag{3.2}$$

The use of standard shape functions N enables the construction of the material coordinate

$$\widetilde{\boldsymbol{P}}^{-} = \boldsymbol{N}\boldsymbol{P}^{-},\ \widetilde{\boldsymbol{P}}^{+} = \boldsymbol{N}\boldsymbol{P}^{+} \tag{3.3}$$

where $\widetilde{\boldsymbol{P}} = \{X(\eta,\zeta), Y(\eta,\zeta), Z(\eta,\zeta)\}$. The matrix of shape function is expressed as

$$\boldsymbol{N} = \begin{bmatrix} L_1 & 0 & 0 & L_2 & 0 & 0 & L_3 & 0 & 0 & L_4 & 0 & 0 \\ 0 & L_1 & 0 & 0 & L_2 & 0 & 0 & L_3 & 0 & 0 & L_4 & 0 \\ 0 & 0 & L_1 & 0 & 0 & L_2 & 0 & 0 & L_3 & 0 & 0 & L_4 \end{bmatrix} \tag{3.4}$$

And with

$$L_1 = \tfrac{1}{4}(1-\eta)(1-\zeta),\ L_2 = \tfrac{1}{4}(1+\eta)(1-\zeta) \tag{3.5}$$

$$L_3 = \tfrac{1}{4}(1+\eta)(1+\zeta),\ L_4 = \tfrac{1}{4}(1-\eta)(1+\zeta)$$

The nodal displacements are given by vector

$$\boldsymbol{d} = \{\boldsymbol{d}^{-}, \boldsymbol{d}^{+}\} = \{u_1, v_1, w_1, \dots, u_8, v_8, w_8\}^T \tag{3.6}$$

And nodal displacements of the upper and lower surface are showed as follows:

$$\boldsymbol{d}^{-} = \{u_1, v_1, w_1, \dots, u_4, v_4, w_4\}^T,\ \boldsymbol{d}^{+} = \{u_5, v_5, w_5, \dots, u_8, v_8, w_8\}^T \tag{3.7}$$

where $\boldsymbol{d} = \{u(\eta,\zeta), v(\eta,\zeta), w(\eta,\zeta)\}$. The material coordinates of the displacement filed are interpolated with the shape function matrix $\boldsymbol{N}$ as

$$\widetilde{\boldsymbol{d}}^{-} = \boldsymbol{N}\boldsymbol{d}^{-},\ \widetilde{\boldsymbol{d}}^{+} = \boldsymbol{N}\boldsymbol{d}^{+} \tag{3.8}$$

where $\widetilde{\boldsymbol{d}} = \{u(\eta,\zeta), v(\eta,\zeta), w(\eta,\zeta)\}$. The material coordinates of the middle surface of the interfacial element is expressed as

$$\tilde{\boldsymbol{c}} = \frac{1}{2}\left(\tilde{\boldsymbol{P}}^{-} + \tilde{\boldsymbol{P}}^{+} + \tilde{\boldsymbol{d}}^{-} + \tilde{\boldsymbol{d}}^{+}\right) = \frac{1}{2}\boldsymbol{N}(\boldsymbol{P}^{-} + \boldsymbol{P}^{+} + \boldsymbol{d}^{-} + \boldsymbol{d}^{+}) \tag{3.9}$$

The tangential vectors to the interfacial middle surface at $(\eta, \zeta)$are obtained by the following expression:

$$\boldsymbol{r_1} = \frac{\partial \tilde{\boldsymbol{c}}}{\partial \eta}, \ \ \bar{\boldsymbol{r}}_{\boldsymbol{2}} = \frac{\partial \tilde{\boldsymbol{c}}}{\partial \zeta} \tag{3.10}$$

The normal vector to the interfacial middle surface $\boldsymbol{r}_3$ is acquired from the equation:

$$\boldsymbol{r}_3 = \boldsymbol{r}_1 \times \bar{\boldsymbol{r}}_2 = \frac{\partial \tilde{\boldsymbol{c}}}{\partial \eta} \times \frac{\partial \tilde{\boldsymbol{c}}}{\partial \zeta} \tag{3.11}$$

The vector $\bar{\boldsymbol{r}}_2$ is not orthogonal to $\boldsymbol{r}_1$, and the orthogonal vector to $\boldsymbol{r}_1$ is obtained through: $\boldsymbol{r}_2 = \boldsymbol{r}_3 \times \boldsymbol{r}_1$. Hence, the unit vectors are defined as: $\hat{\boldsymbol{r}}_i = \boldsymbol{r}_i/|\boldsymbol{r}_i|$ $(i = 1, 2, 3)$. The rotation tensor $\boldsymbol{R}$ used to transform the global coordinate system (X, Y, Z) to the local material coordinate system (η, ζ, ξ) is given by

$$\boldsymbol{R} = \{\hat{\boldsymbol{r}}_{\boldsymbol{1}}, \hat{\boldsymbol{r}}_{\boldsymbol{2}}, \hat{\boldsymbol{r}}_{\boldsymbol{3}}\} \tag{3.12}$$

In order to calculate the relative displacement jumps and tractions across the cohesive interface element, the displacement jumps in the global coordinate system should transform to the local material coordinate system through the matrix $\boldsymbol{R}$.

Finally, the displacement jumps across the interfacial element are given by

$$\boldsymbol{\delta} = \boldsymbol{B}\boldsymbol{d} = \boldsymbol{R}^{\boldsymbol{T}}[-\boldsymbol{N} \quad \boldsymbol{N}]\boldsymbol{d} \tag{3.13}$$

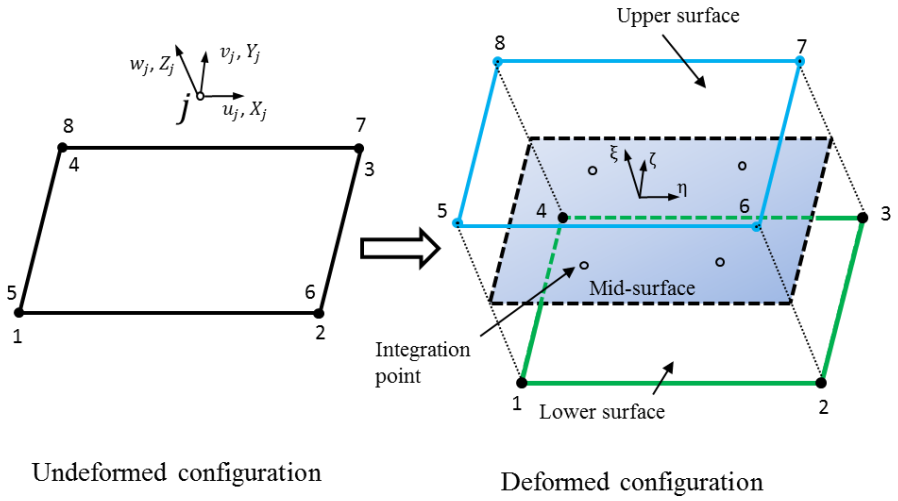


Fig. 3.1 Eight node interface element for three dimensional analysis.

The rate of the relative displacement jumps and tractions can be obtained through a tangent modulus matrix $\boldsymbol{D}$,

$$\dot{\boldsymbol{t}} = \boldsymbol{D}\dot{\boldsymbol{v}} \tag{3.14}$$

where $\boldsymbol{t} = (t_1, t_2, t_3)^T$ and $D_{ij} = \frac{\partial t_i}{\partial v_j}$, $(v_1,\ v_2,\ v_3) = (\delta_{s1},\ \delta_{s2},\ \delta_n)$. The full derivation of tangential modulus is provided in ***Appendix B***.

The global nodal force vector from the virtual principles for the 8 nodes interface element is defined as (Y. Arun Roy, 2001)

$$\boldsymbol{f} = \int_{-1}^{1}\int_{-1}^{1} \boldsymbol{B}^T\, \boldsymbol{t}|r_3|d\eta d\zeta \tag{3.15}$$

where $\boldsymbol{t}$ is the cohesive traction vector. For the implicit solution process, the global tangential stiffness matrix for the cohesive elements is obtained by (Y. Arun Roy, 2001)

$$\boldsymbol{K}_T = \int_{-1}^{1}\int_{-1}^{1} \boldsymbol{B}^T\, \boldsymbol{D}\boldsymbol{B}|r_3|d\eta d\zeta \tag{3.16}$$

3.3 Mixed-Mode Cohesive Zone Model

The mixed-mode CZM is implemented in the current study through a user UEL subroutine in ABAQUS (ABAQUS, 2013). It describes the relationship between the cohesive tractions between the two faces of an interface and the separations (displacement jumps) across the interface. According to the CZM, the delamination failure of the plaque-media interface involves three steps. The first step is damage initiation, which refers to the start of degradation of the cohesive element when an effective displacement jump Δ_m^0 is reached (as shown on the damage initiation locus in Fig. 3.2). The second step is damage evolution, during which damage accumulation occurs in the cohesive element. The third step is complete failure of the cohesive element after the effective displacement jump reaches a critical effective separation value Δ_m^f (as shown on the full failure locus in Fig.3. 2) (Turon et al., 2006).

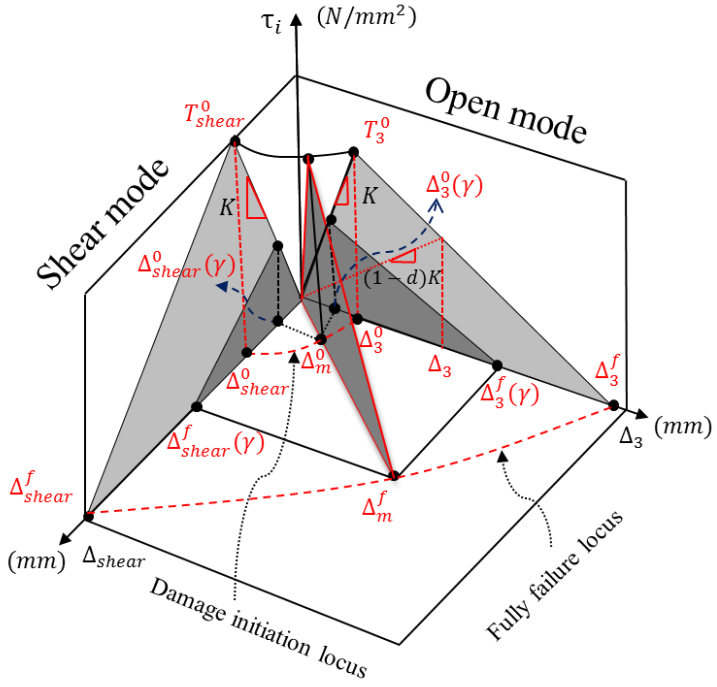


Fig. 3.2 Interfacial triangular mixed-mode cohesive traction-separation law.

The failure criterion proposed by Benzeggagh and Kenane (M.L. Benzeggagh, 1996) has been found to fit experimental results accurately and is employed in the current study to govern the failure of the cohesive element. It can be expressed as:

$$G_c = G_T \tag{3.17}$$

$$G_c = G_{Ic} + (G_{IIc} - G_{Ic}) \left(\frac{G_{shear}}{G_T}\right)^{\alpha} \tag{3.18}$$

$$G_T = G_I + G_{shear} \quad , G_{shear} = G_{II} + G_{III} \tag{3.20}$$

where G_c is the fracture toughness of the material; G_{Ic}, G_{IIc} are the fracture toughness values of the material for mode I and mode II, respectively; G_I, G_{II} and G_{III} represent the mode I, mode II and mode III energy release rate, respectively.

The triangular cohesive law that governs material separation process under mix-mode loading can be written as:

$$\tau_3 = \begin{cases} K\Delta_3 , & 0 \le \Delta_3 < \Delta_3^0(\gamma) \\ (1-d)K\Delta_3 , & \Delta_3^0(\gamma) \le \Delta_3 < \Delta_3^f(\gamma) \\ 0 , & \Delta_3 \ge \Delta_3^f(\gamma) \end{cases} \tag{3.21}$$

$$\tau_{shear} = \begin{cases} K\Delta_{shear} , & \Delta_{shear} < \Delta_{shear}^0(\gamma) \\ (1-d)K\Delta_{shear} , & \Delta_{shear}^0(\gamma) \le \Delta_{shear} < \Delta_{shear}^f(\gamma) \\ 0 , & \Delta_{shear} \ge \Delta_{shear}^f(\gamma) \end{cases} \tag{3.22}$$

where τ_3 and τ_{shear} are the cohesive tractions, which are the function of the displacement jumps Δ_i (i =1,2,3) in the local coordinates and $\Delta_{shear} = \sqrt{(\Delta_1)^2 + (\Delta_2)^2}$; $\tau_3 = K\Delta_3$ when $\Delta_3 < 0$ in order to avoid interpenetration of the delaminated plaque-media interface; K is a penalty stiffness; d is the damage variable which ranges from 0 to 1; Δ_1^0, Δ_2^0 and Δ_3^0 are the displacement jumps corresponding to damage initial under pure Mode I, Mode

II and Mode III conditions ($\Delta_1^0 = \Delta_2^0 = \Delta_{shear}^0 = T_{shear}^0/K$ and $\Delta_3^0 = T_3^0/K$), respectively; $\Delta_3^f = 2G_{Ic}/T_3^0$ and $\Delta_{shear}^f = 2G_{shear_c}/T_{shear}^0$ ($G_{shear_c} = G_{IIc}$) are the displacement jumps corresponding to full failure under pure open mode and shear mode conditions, respectively; and T_3^0 and T_{shear}^0 are the strengths of the cohesive interface along the normal direction and tangential direction, respectively (as shown in Fig.3.2); $\gamma = \frac{\Delta_{shear}}{\Delta_{shear}+\Delta_3}$ ($\Delta_3 \geq 0$) and $\gamma = 1$ ($\Delta_3 < 0$), γ is a given mode ratio for mix-mode loading condition.

The energy release rate for open mode and shear mode under mix-mode loading can be written as:

$$G_I = \begin{cases} \frac{1}{2}\tau_3\Delta_3\,, & 0 \leq \Delta_3 < \Delta_3^0(\gamma) \\ \frac{1}{2}K\Delta_3^0(\gamma)\Delta_3^f(\gamma) - \frac{1}{2}\tau_3\Delta_3^f(\gamma), & \Delta_{3(\gamma)}^0 \leq \Delta_3 \leq \Delta_3^f(\gamma) \end{cases} \tag{3.23}$$

$$G_{shear} =$$

$$\begin{cases} \frac{1}{2}\tau_{shear}\Delta_{shear}\,, & 0 \leq \Delta_{shear} < \Delta_{shear}^0(\gamma) \\ \frac{1}{2}K\Delta_{shear}^0(\gamma)\Delta_{shear}^f(\gamma) - \frac{1}{2}\tau_{shear}\Delta_{shear}^f(\gamma), & \Delta_{shear}^0(\gamma) \leq \Delta_{shear} \leq \Delta_{shear}^f(\gamma) \end{cases} \tag{3.24}$$

where $\Delta_3^0(\gamma)$ and $\Delta_{shear}^0(\gamma)$ are the normal and shear displacement jumps corresponding to damage initial under mix-mode loading, respectively; $\Delta_3^f(\gamma)$ and $\Delta_{shear}^f(\gamma)$ are the normal and shear displacement jumps corresponding to full failure under mix-mode loading, respectively; From equation (3.20), the effective displacement jump of damage initiation Δ_m^0 and critical effective separation value Δ_m^f can be expressed as:

$$\Delta_m^0 = \sqrt{(\Delta_3^0)^2 + [(\Delta_{shear}^0)^2 - (\Delta_3^0)^2]\left(\frac{G_{shear}}{G_T}\right)^{\alpha}} \tag{3.25}$$

$$\Delta_m^f = \frac{2\left[G_{Ic} + (G_{IIc} - G_{Ic})\left(\frac{G_{shear}}{G_T}\right)^{\alpha}\right]}{K\,\Delta_m^0} \tag{3.26}$$

where α is a parameter obtained from the experiment (Camanho, 2003); Clearly, single open mode or shear mode is particular case of the proposed formulation, as $\Delta_m^0 = \Delta_3^0$, $\Delta_m^f = \Delta_3^f$ for open mode (Mode I), and $\Delta_m^0 = \Delta_{shear}^0$, $\Delta_m^f = \Delta_{shear}^f$ for shear mode. Details of the cohesive finite element can be found in (Camanho, 2003; Turon et al., 2006).

3.4 Exponential CZM

An exponential form for the free energy potential (φ) per unit (undeformed) area can be expressed as (Ortiz and Pandolfi, 1999; Y. Arun Roy, 2001)

$$\varphi = e\sigma_c\delta_c\left[1 - \left(1 + \frac{\delta}{\delta_c}\right)exp(-\frac{\delta}{\delta_c})\right] \tag{3.27}$$

where $e = \exp(1) \approx 2.71828$ and σ_c denote the strength of the material; δ_c is the maximum effective displacement at $t = \sigma_c$. Considering the loading conditions:

With the reference to Fig. 3.3, $\boldsymbol{\delta}_n = (\boldsymbol{\delta}\cdot\boldsymbol{n})\boldsymbol{n} = \delta_n\boldsymbol{n} > 0$ for opening separation, and $\boldsymbol{\delta}_s = \boldsymbol{\delta} - \delta_n\boldsymbol{n} = (\boldsymbol{I} - \boldsymbol{n}\otimes\boldsymbol{n})\boldsymbol{\delta}$ represents the sliding displacement across the cohesive surfaces (S), $\boldsymbol{\delta}_n$ and $\boldsymbol{\delta}_s$ characterizing the projection of $\boldsymbol{\delta}$ onto the line spanned by $\boldsymbol{n}$ and onto the plane normal to $\boldsymbol{n}$, respectively. Similarly, $\boldsymbol{t}_n$ is the normal traction and the two shear tractions, $\boldsymbol{t}_{s1}$ and $\boldsymbol{t}_{s2}$, across the cohesive surfaces. A possible equation to show that a local traction ($\boldsymbol{t}$) across the cohesive surfaces (S) can be derive from a free energy potential per unit (undeformed) area, $\varphi(\boldsymbol{\delta}, \boldsymbol{q})$, denotes as

$$t = \frac{\partial\varphi}{\partial\boldsymbol{\delta}}(\boldsymbol{\delta}, \boldsymbol{q}) \tag{3.28}$$

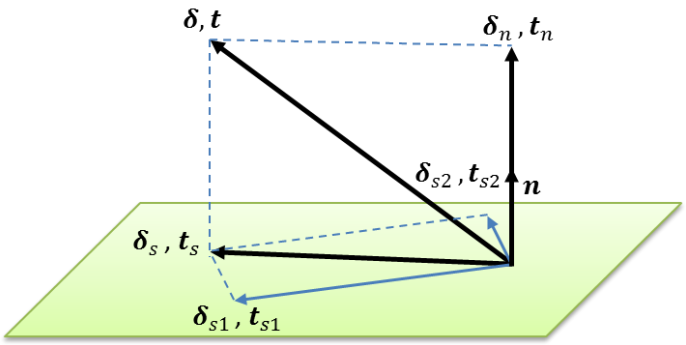


Fig. 3.3 Schematic of the tractions and displacement jump perpendicular and across to the cohesive surface.

where $\boldsymbol{\delta}$ is the displacement jump across the cohesive surfaces, and $\boldsymbol{q}$ represents the internal variables which denote the inelastic behavior of the separation of the cohesive interfaces. The single scalar function, $\varphi(\boldsymbol{\delta}, \boldsymbol{q})$, can be expressed as $\varphi(\delta_n, \delta_s, \boldsymbol{q})$ when the displacement jump ($\boldsymbol{\delta}$) is simplified by δ_n, which denote the displacement jump along the normal direction; and $\boldsymbol{\delta}_s$, which is the sliding displacement across the cohesive surfaces, in the form

$$\delta_s = \|\boldsymbol{\delta}_s\| = \sqrt{\delta_{s1}^2 + \delta_{s2}^2} \tag{3.29}$$

where δ_{s1} and δ_{s2} denote components of the two directions of the sliding displacement ($\boldsymbol{\delta}_s$) across the cohesive surfaces and the quantity$\|\mathbf{A}\|$ is called the magnitude of a tensor **A**. Hence, the local traction ($\boldsymbol{t}$) becomes

$$\boldsymbol{t} = \frac{\partial \varphi}{\partial \delta_n}(\delta_n, \delta_s, \boldsymbol{q})\boldsymbol{n} + \frac{\partial \varphi}{\partial \delta_s}(\delta_n, \delta_s, \boldsymbol{q})\frac{\boldsymbol{\delta}_s}{\delta_s} = \boldsymbol{t}_n + \boldsymbol{t}_s \tag{3.30}$$

The effective displacement jump is shown

$$\delta = \sqrt{\lambda^2 \delta_s^2 + \delta_n^2}\,. \tag{3.31}$$

where λ is a scalar parameter which introduced to assign different weights to the opening and sliding displacements. Using eqs. (3.28) and (3.30) we obtain the cohesive tractions in the form

$$\boldsymbol{t} = \frac{t}{\delta}(\lambda^2 \boldsymbol{\delta}_s + \delta_n \boldsymbol{n}) \tag{3.32}$$

where

$$t = \frac{\partial \varphi}{\partial \delta}(\delta, \boldsymbol{q}) \tag{3.33}$$

The effective traction can be obtained from eqs. (3.32) and (3.33), which expressed as

$$t = \sqrt{\beta^{-2}\|\boldsymbol{t}_s\|^2 + t_n^2}\,, \tag{3.34}$$

$$t = \frac{\partial \varphi}{\partial \delta} = e\sigma_c \frac{\delta}{\delta_c} exp(-\frac{\delta}{\delta_c}) \text{ if } \delta \geq \delta_{max} \text{ or } \dot{\delta} \geq 0 \tag{3.35}$$

And for the unloading conditions:

$$t = \left(\frac{t_{max}}{\delta_{max}}\right)\delta \text{ if } \delta < \delta_{max} \text{ or } \dot{\delta} < 0 \tag{3.36}$$

The work of separation per unit cohesive surface follows the form

$$G_c = e\sigma_c \delta_c \tag{3.37}$$

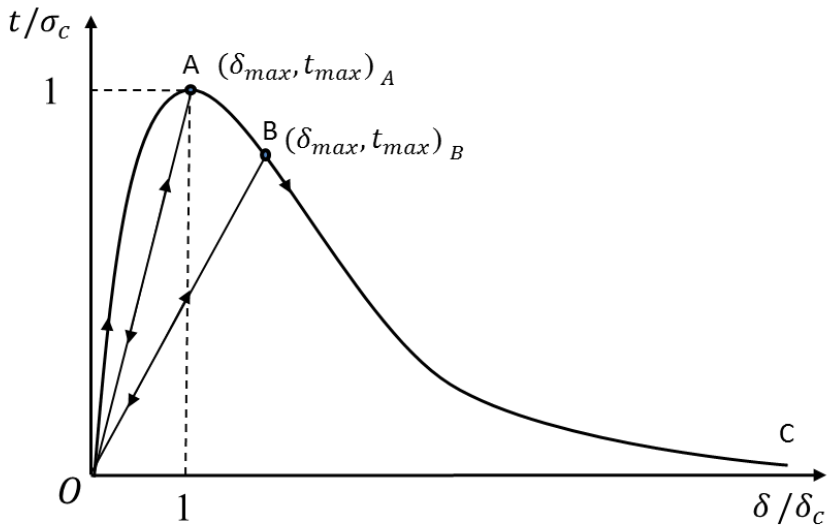


Fig. 3.4 Exponential irreversible cohesive model denotes with normalized effective traction and effective displacement.

For the purposes to express the irreversible mechanism, we introduce a damage parameter in order to represent the damage of the cohesive surfaces during the loading and unloading conditions, it defined as

$$d = \frac{\varphi(\delta_{max})}{G_c} \tag{3.38}$$

Evidently, d ranges from 0 to 1, corresponding to no damage of the cohesive surface and a complete separation of the cohesive surface, respectively. Fig. 3.4 illustrates the loading and unloading processes of the exponential cohesive traction-separation law, the damage will accumulate when effective traction t exceeds zero. Thus, the force-displacement relation will go along line AO and BO when unloading at point A and B, respectively, because permanent damage occurs on the cohesive surface at point A and B.

Summary of the quantities required for an efficient finite element implementation of exponential CZM in writing UEL subroutine for ABAQUS is expressed in Table 3.1. The derivation of elastic tensor is presented in ***Appendix B***.

Table 3.1 Summary of the quantities required for an efficient finite element implementation of exponential CZM in writing UEL subroutine for ABAQUS.

Cohesive parameters: G_c, σ_c, K, λ (Given)
THEN:
Initial condition $r_0 = 0$, $d_0 = 0$, $f_0 = 0$ (Intermediate variable), $g_0 = 0$ (Intermediate variable)
DO $i = 1, m$ (the number of integration points)
Cohesive damage parameter $d_i = d_{i-1}$
Maximum effective displacement $\delta_c = G_c / e\sigma_c$
Sliding displacements and normal displacement jump: $\delta_{s1\,i}$, $\delta_{s2\,i}$ and $\delta_{n\,i}$ (Calculate with the nodal displacements from ABAQUS)
Effective displacement $\delta_i = \sqrt{\lambda^2 \delta_{s\,i}^2 + \delta_{n\,i}^2}$, $\delta_{s\,i} = \sqrt{\delta_{s1\,i}^2 + \delta_{s2\,i}^2}$
Mixed-mode damage threshold $p_i = p_{i-1}$
Update internal variables
If ($\delta_i > p_i$) then (loading)

$$p_i = \delta_i,\ f_i = 1$$

else (Unloading)

$$f_i = 0$$

End if

$$d_i = 1 - \left(1 + \frac{\delta_i}{\delta_c}\right) e^{-\frac{\delta_i}{\delta_c}}$$

Determination of tractions

$$g_i = g_{i-1}$$

$$t_i = e\sigma_c(1 - d_i) - e\sigma_c e^{-\frac{\delta_i}{\delta_c}}$$

If ($f_i = 0$) then

$$t_i = (g_i / p_i)\delta_i$$

End if

$$t_{1\,i} = t_i \lambda^2 \delta_{s1\,i}/\delta_i,\ t_{2\,i} = t_i \lambda^2 \delta_{s2\,i}/\delta_i,\ t_{3\,i} = t_i \delta_{n\,i}/\delta_i$$

If ($\delta_{n\,i} < 0$) then

$t_{3\,i} = K\delta_{n\,i}$ (Avoid interpenetration of the elements)

End if
If ($t_i > g_i$) then

$$g_i = t_i$$

End if
If ($t_i < \sigma_c$ and $\delta_i > \delta_c$ and $f_i = 1$) then

$$g_i = t_i$$

End if

$$\varphi'_i = (g_i/p_i)\delta_i,\ \varphi''_i = g_i/p_i,$$

If ($f_i = 1$) then

$$\varphi'_i = t_i,\ \varphi''_i = \frac{\varphi'_i}{\delta_i}(1 - \frac{\delta_i}{\delta_c})$$

End if

Update the elasticity tensor

$$S_i = \varphi''_i - \frac{\varphi'_i}{\delta_i}$$

$D_{11\,i} = \frac{\varphi'_i\lambda^2}{\delta_i} + \frac{\lambda^4\delta_{s1\,i}^2}{\delta_i^{\,2}}S_i,\ D_{12\,i} = D_{21\,i} = \frac{\lambda^4\delta_{s1\,i}\delta_{s2\,i}}{\delta_i^{\,2}}S_i,\ D_{13\,i} = D_{31\,i} = \frac{\lambda^2\delta_{s1\,i}\delta_{n\,i}}{\delta_i^{\,2}}S_i,$

$D_{12\,i} = D_{21\,i} = \frac{\lambda^4\delta_{s1\,i}\delta_{s2\,i}}{\delta_i^{\,2}}S_i,\ D_{22\,i} = \frac{\varphi'_i\lambda^2}{\delta_i} + \frac{\lambda^4\delta_{s2\,i}^2}{\delta_i^{\,2}}S_i,\ D_{23\,i} = D_{32\,i} = \frac{\lambda^2\delta_{s2\,i}\delta_{n\,i}}{\delta_i^{\,2}}S_i,$

$D_{13\,i} = D_{31\,i} = \frac{\lambda^2\delta_{s1\,i}\delta_{n\,i}}{\delta_i^{\,2}}S_i,\ D_{23\,i} = D_{32\,i} = \frac{\lambda^2\delta_{s2\,i}\delta_{n\,i}}{\delta_i^{\,2}}S_i,\ D_{33\,i} = \frac{\varphi'_i}{\delta_i} + \frac{\delta_{n\,i}^2}{\delta_i^{\,2}}S_i$

END DO

3.5 Triangular CZM

A triangular form of energy release rate for the cohesive surface can be expressed as:

$$G_c = \frac{1}{2}\sigma_c\delta_c \tag{3.39}$$

The displacement jump for the damage initiation and complete damage of the cohesive element denote by

$$\delta_0 = \frac{\sigma_c}{K} \tag{3.40}$$

$$\delta_c = \frac{2G_c}{\sigma_c} \tag{3.41}$$

where K is a penalty stiffness.

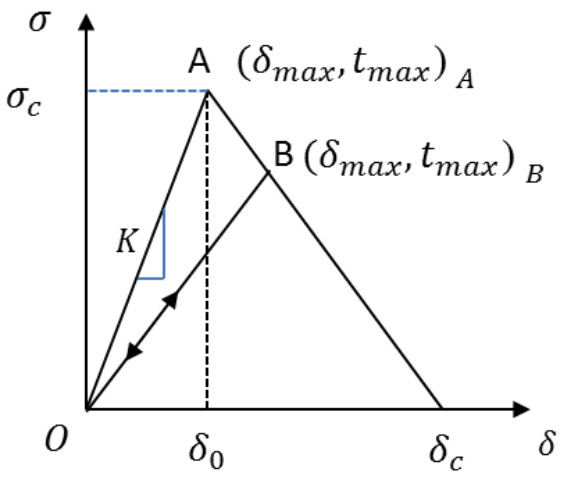


Fig. 3.5 Triangular irreversible cohesive model denotes with effective traction and effective displacement.

The effective traction can be expressed as

$$\varphi' = t = \begin{cases} \frac{\delta}{\delta_0}\sigma_c \ , \ \delta \le \delta_0 \\ \sigma_c\left(\frac{\delta_c - \delta}{\delta_c - \delta_0}\right) = \sigma_c(1-d) \ , \ \delta_0 \le \delta < \delta_c \\ 0 \ , \ \delta_c \le \delta \end{cases} \tag{3.42}$$

where δ is the 'effective' opening displacement which is given by

$$\delta = \sqrt{\lambda^2\delta_s^2 + \delta_n^2} \tag{3.43}$$

where λ is a scalar parameter which introduced to assign different weights to the opening displacement δ_n and sliding displacement, which is denoted by

$$\delta_s = \sqrt{\delta_{s1}^2 + \delta_{s2}^2} \tag{3.44}$$

where δ_{s1} and δ_{s2} denote components of the two directions of the sliding displacement δ_s across the cohesive surfaces.

The first-order partial derivative of the effective traction t with respective to effective opening displacement is given by

$$\varphi'' = \frac{\partial t}{\partial \delta} = \begin{cases} \frac{\sigma_c}{\delta_0} \ , & \delta \le \delta_0 \\ \frac{-\sigma_c}{\delta_c - \delta_0} = \frac{-\sigma_c d}{\delta - \delta_0} \ , & \delta_0 \le \delta < \delta_c \\ 0 \ , & \delta_c \le \delta \end{cases} \tag{3.45}$$

where d is the Damage variable defined to represent the softening of the cohesive element

$$d = \begin{cases} 0 \ , & \delta \le \delta_0 \\ \frac{G_c - \left[\sigma_c \left(\frac{\delta_c - \delta}{\delta_c - \delta_0}\right) \delta_c \frac{1}{2}\right]}{G_c} = \frac{\delta - \delta_0}{\delta_c - \delta_0} \ , & \delta_0 \le \delta < \delta_c \\ 1 \ , & \delta_c \le \delta \end{cases} \tag{3.46}$$

Evidently, d ranges from 0 to 1, which corresponding to that there is no damage of the cohesive surface and a fully separate of the cohesive surface, respectively. Fig. 3.5 illustrates the loading and unloading processes of the triangular cohesive traction-separation law, the damage will accumulate when effective traction t exceeds σ_c, where at the point A in Fig. 3.5. Thus, the traction-separation relation will go along line AO and BO when unloading at point A and B, respectively, because a permanent damage occurs on the cohesive surface at point A and B. On the contrary, the traction-separation relation will go along the original curve when no damage occurs on the cohesive surface. The derivations of the triangular CZM implemented in ABAQUS are shown in Table 3.2.

Table 3.2 Summary of the quantities required for an efficient finite element implementation of triangular CZM in writing UEL subroutine for ABAQUS.

Cohesive parameters: G_c, σ_c, K, λ (Given)
THEN:
Initial condition $r_0 = 0$, $d_0 = 0$, $f_0 = 0$ (Intermediate variable), $g_0 = 0$ (Intermediate variable)
DO $i = 1, m$ (the number of integration points)
Cohesive damage parameter $d_i = d_{i-1}$
Effective displacement of damage initiation $\delta_0 = \frac{\sigma_c}{K}$
Maximum effective displacement $\delta_c = \frac{2G_c}{\sigma_c}$
Sliding displacements and normal displacement jump: $\delta_{s1\,i}$, $\delta_{s2\,i}$ and $\delta_{n\,i}$ (Calculate with the nodal displacements from ABAQUS)
Effective displacement $\delta_i = \sqrt{\lambda^2\delta_{s\,i}^2 + \delta_{n\,i}^2}$, $\delta_{s\,i} = \sqrt{\delta_{s1\,i}^2 + \delta_{s2\,i}^2}$
Mixed-mode damage threshold $p_i = p_{i-1}$
Update internal variables
If ($\delta_i > p_i$) then (loading)

$$p_i = \delta_i,\ f_i = 1$$

else (Unloading)

$$f_i = 0$$

End if
If ($\delta_i < \delta_0$) then

$$d_i = 0$$

else

$$d_i = \frac{\delta - \delta_0}{\delta_c - \delta_0}$$

End if
Determination of tractions

$$g_i = g_{i-1}$$

If ($\delta_i < \delta_0$) then

$$t_i = \frac{\delta}{\delta_0}\sigma_c$$

else

$$t_i = \sigma_c(1 - d)$$

End if
If ($f_i = 0$) then

$$t_i = (g_i/p_i)\delta_i$$

End if

$$t_{1\,i} = t_i\lambda^2\delta_{s1\,i}/\delta_i,\ t_{2\,i} = t_i\lambda^2\delta_{s2\,i}/\delta_i,\ t_{3\,i} = t_i\delta_{n\,i}/\delta_i$$

If ($\delta_{n\,i} < 0$) then

$t_{3\,i} = K\delta_{n\,i}$ (Avoid interpenetration of the elements)

End if
If ($t_i > g_i$) then

$$g_i = t_i$$

End if

If ($t_i < \sigma_c$ and $\delta_i > \delta_0$ and $f_i = 1$) then

$$g_i = t_i$$

End if

$$\varphi'_i = (g_i/p_i)\delta_i,\ \varphi''_i = g_i/p_i$$

If ($f_i = 1$) then

If ($\delta_i < \delta_0$) then

$$\varphi'_i = t_i,\ \varphi''_i = \frac{\sigma_c}{\delta_0}$$

else

$$\varphi'_i = t_i,\ \varphi''_i = \frac{-\sigma_c d}{\delta - \delta_0}$$

End if

End if

Update the elasticity tensor

$$S_i = \varphi''_i - \frac{\varphi'_i}{\delta_i}$$

$$D_{11\,i} = \frac{\varphi'_i \lambda^2}{\delta_i} + \frac{\lambda^4 \delta_{s1\,i}^2}{\delta_i^2} S_i,\ D_{12\,i} = D_{21\,i} = \frac{\lambda^4 \delta_{s1\,i}\delta_{s2\,i}}{\delta_i^2} S_i,\ D_{13\,i} = D_{31\,i} = \frac{\lambda^2 \delta_{s1\,i}\delta_{n\,i}}{\delta_i^2} S_i,$$

$$D_{12\,i} = D_{21\,i} = \frac{\lambda^4 \delta_{s1\,i}\delta_{s2\,i}}{\delta_i^2} S_i,\ D_{22\,i} = \frac{\varphi'_i \lambda^2}{\delta_i} + \frac{\lambda^4 \delta_{s2\,i}^2}{\delta_i^2} S_i,\ D_{23\,i} = D_{32\,i} = \frac{\lambda^2 \delta_{s2\,i}\delta_{n\,i}}{\delta_i^2} S_i,$$

$$D_{13\,i} = D_{31\,i} = \frac{\lambda^2 \delta_{s1\,i}\delta_{n\,i}}{\delta_i^2} S_i,\ D_{23\,i} = D_{32\,i} = \frac{\lambda^2 \delta_{s2\,i}\delta_{n\,i}}{\delta_i^2} S_i,\ D_{33\,i} = \frac{\varphi'_i}{\delta_i} + \frac{\delta_{n\,i}^2}{\delta_i^2} S_i$$

END DO

3.6 Trapezoidal CZM

A trapezoidal form of energy release rate for the cohesive surface can be expressed as (RDSG Campillho, 2013):

$$G_c = \frac{1}{2}\sigma_c[(\delta_2 - \delta_1) + \delta_c] \tag{3.47}$$

The displacement jump for the damage initiation, traction softening initiation and complete damage of the cohesive element denote by

$$\delta_1 = \frac{\sigma_c}{K} \tag{3.48}$$

$$\delta_2 = \frac{G_c}{\sigma_c} \tag{3.49}$$

$$\delta_c = \delta_1 + \delta_2 \tag{3.50}$$

where K is a penalty stiffness.

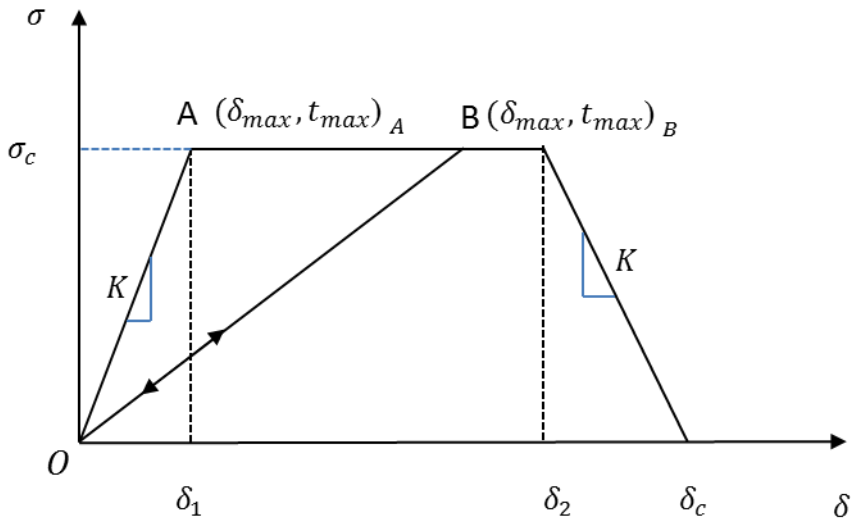


Fig. 3.6 Trapezoidal irreversible cohesive model denotes with effective traction and effective displacement.

The effective traction can be expressed as

$$\varphi' = t = \frac{\partial \varphi}{\partial \delta} = \begin{cases} \frac{\delta}{\delta_1}\sigma_c \ , & \delta \le \delta_1 \\ \sigma_c \ , & \delta_1 \le \delta < \delta_2 \\ \frac{(1-d)(\delta_2 - \delta_1 + \delta_c)}{\delta_c}\sigma_c \ , & \delta_2 \le \delta < \delta_c \\ 0 \ , & \delta_c \le \delta \end{cases} \tag{3.51}$$

where δ is the 'effective' opening displacement which is given by

$$\delta = \sqrt{\lambda^2 \delta_s^2 + \delta_n^2} \tag{3.52}$$

where λ is a scalar parameter which introduced to assign different weights to the opening displacement δ_n and sliding displacement, which is denoted by

$$\delta_s = \sqrt{\delta_{s1}^2 + \delta_{s2}^2} \tag{3.53}$$

where δ_{s1} and δ_{s2} denote components of the two directions of the sliding displacement δ_s across the cohesive surfaces.

The first-order partial derivative of the effective traction t with respective to effective opening displacement is given by

$$\varphi'' = \frac{\partial t}{\partial \delta} = \begin{cases} \frac{\sigma_c}{\delta_1} \ , & \delta \le \delta_1 \\ 0 \ , & \delta_1 \le \delta < \delta_2 \\ -\sigma_c \frac{(1-d)(\delta_2 - \delta_1 + \delta_c)}{\delta_c(\delta_c - \delta)} \ , & \delta_2 \le \delta < \delta_c \\ 0 \ , & \delta_c \le \delta \end{cases} \tag{3.54}$$

where d is the Damage variable defined to represent the softening of the cohesive element

$$d = \begin{cases} 0 \ , & \delta \le \delta_1 \\ \frac{(\delta - \delta_1)}{(\delta_2 - \delta_1 + \delta_c)} \ , & \delta_1 \le \delta < \delta_2 \\ 1 - \frac{\delta_c(\delta_c - \delta)}{(\delta_c - \delta_2)(\delta_2 - \delta_1 + \delta_c)} \ , & \delta_2 \le \delta < \delta_c \\ 1 \ , & \delta_c \le \delta \end{cases} \tag{3.55}$$

Evidently, d ranges from 0 to 1, which corresponding to that there is no damage of the cohesive surface and a fully separate of the cohesive surface, respectively. Fig. 3.6 illustrates the loading and unloading processes of the Trapezoidal cohesive traction-

separation law, the damage will accumulate when effective traction t exceeds σ_c, where at the point A in Fig. 3.6. Thus, the force-displacement relation will go along line AO and BO when unloading at point A and B, respectively, because a permanent damage occurs on the cohesive surface at point A and B. On the contrary, the force-displacement relation will go along the original curve when no damage occurs on the cohesive surface. The derivations of the trapezoidal CZM implemented in ABAQUS are shown in Table 3.3.

Table 3.3 Summary of the quantities required for an efficient finite element implementation of trapezoidal CZM in writing UEL subroutine for ABAQUS.

Cohesive parameters: G_c, σ_c, K, λ (Given)
THEN:
Initial condition $r_0 = 0$, $d_0 = 0$, $f_0 = 0$ (Intermediate variable), $g_0 = 0$ (Intermediate variable)
DO $i = 1, m$ (the number of integration points)
Cohesive damage parameter $d_i = d_{i-1}$
Effective displacement of damage initiation $\delta_1 = \frac{\sigma_c}{K}$
Effective displacement of traction softening initiation $\delta_2 = \frac{G_c}{\sigma_c}$
Maximum effective displacement $\delta_c = \delta_1 + \delta_2$
Sliding displacements and normal displacement jump: $\delta_{s1\,i}$, $\delta_{s2\,i}$ and $\delta_{n\,i}$ (Calculate with the nodal displacements from ABAQUS)
Effective displacement $\delta_i = \sqrt{\lambda^2 \delta_{s\,i}^2 + \delta_{n\,i}^2}$, $\delta_{s\,i} = \sqrt{\delta_{s1\,i}^2 + \delta_{s2\,i}^2}$
Mixed-mode damage threshold $p_i = p_{i-1}$
Update internal variables
If ($\delta_i > p_i$) then (loading)

$$p_i = \delta_i,\ f_i = 1$$

else (Unloading)

$$f_i = 0$$

End if
If ($\delta_i < \delta_1$) then

$$d_i = 0$$

End if
If ($\delta_i < \delta_2$ and $\delta_i \geq \delta_1$) then

$$d_i = \frac{(\delta_i - \delta_1)}{(\delta_2 - \delta_1 + \delta_c)}$$

End if
If ($\delta_i > \delta_2$) then

$$d_i = 1 - \frac{\delta_c(\delta_c - \delta_i)}{(\delta_c - \delta_2)(\delta_2 - \delta_1 + \delta_c)}$$

End if

Determination of tractions

$$g_i = g_{i-1}$$

If (δ_i<δ_1) then

$$t_i = \frac{\delta_i}{\delta_1}\sigma_c$$

End if

If (δ_i<δ_2 and $\delta_i \geq \delta_1$) then

$$t_i = \sigma_c$$

End if

If (δ_i>δ_2) then

$$t_i = \frac{(1 - d_i)(\delta_2 - \delta_1 + \delta_c)}{\delta_c}\sigma_c$$

End if

If ($f_i = 0$) then

$$t_i = (g_i/p_i)\delta_i$$

End if

$$t_{1\,i} = t_i\lambda^2\delta_{s1\,i}/\delta_i,\ t_{2\,i} = t_i\lambda^2\delta_{s2\,i}/\delta_i,\ t_{3\,i} = t_i\delta_{n\,i}/\delta_i$$

If ($\delta_{n\,i} < 0$) then

$t_{3\,i} = K\delta_{n\,i}$ (Avoid interpenetration of the elements)

End if

If ($t_i > g_i$) then

$$g_i = t_i$$

End if

If ($t_i = \sigma_c$ and $\delta_i > \delta_1$ and $f_i = 1$) then

$$g_i = t_i$$

End if

If ($t_i < \sigma_c$ and $\delta_i > \delta_2$ and $f_i = 1$) then

$$g_i = t_i$$

End if

$$\varphi'_i = (g_i/p_i)\delta_i,\ \varphi''_i = g_i/p_i$$

If ($f_i = 1$) then

If (δ_i<δ_1) then

$$\varphi' = t_i,\ \varphi'' = \frac{\sigma_c}{\delta_1}$$

End if

If (δ_i<δ_2 and $\delta_i \geq \delta_1$) then

$$\varphi' = t_i,\ \varphi'' = 0$$

End if

If (δ_i>δ_2) then

$$\varphi' = t_i,\ \varphi'' = -\sigma_c\frac{(1-d_i)(\delta_2-\delta_1+\delta_c)}{\delta_c(\delta_c-\delta_i)}$$

End if

End if

Update the elasticity tensor

$$S_i = \varphi''_i - \frac{\varphi'_i}{\delta_i}$$

$D_{11\,i} = \frac{\varphi'_i \lambda^2}{\delta_i} + \frac{\lambda^4 \delta_{s1\,i}^2}{\delta_i^2} S_i$, $D_{12\,i} = D_{21\,i} = \frac{\lambda^4 \delta_{s1\,i} \delta_{s2\,i}}{\delta_i^2} S_i$, $D_{13\,i} = D_{31\,i} = \frac{\lambda^2 \delta_{s1\,i} \delta_{n\,i}}{\delta_i^2} S_i$,

$D_{12\,i} = D_{21\,i} = \frac{\lambda^4 \delta_{s1\,i} \delta_{s2\,i}}{\delta_i^2} S_i$, $D_{22\,i} = \frac{\varphi'_i \lambda^2}{\delta_i} + \frac{\lambda^4 \delta_{s2\,i}^2}{\delta_i^2} S_i$, $D_{23\,i} = D_{32\,i} = \frac{\lambda^2 \delta_{s2\,i} \delta_{n\,i}}{\delta_i^2} S_i$,

$D_{13\,i} = D_{31\,i} = \frac{\lambda^2 \delta_{s1\,i} \delta_{n\,i}}{\delta_i^2} S_i$, $D_{23\,i} = D_{32\,i} = \frac{\lambda^2 \delta_{s2\,i} \delta_{n\,i}}{\delta_i^2} S_i$, $D_{33\,i} = \frac{\varphi'_i}{\delta_i} + \frac{\delta_{n\,i}^2}{\delta_i^2} S_i$

END DO

3.7 Summary

The interface cohesive element implemented for the user UEL subroutine was provided. After that, a mixed-mode cohesive zone model used most in simulation of composite material was introduced. In order to find out the effects to the simulation results derived from different types of CZM, the exponential, triangular and trapezoidal shape of traction-separation laws were provided with detail derivations. The material parameters required to define the constitutive relations are the critical energy release rate, the strength of the interface, the penalty stiffness and the displacement jump ratio. These parameters are kept the same for the three different types of CZM.

CHAPTER 4

MODELING OF EXPERIMENTAL ATHEROSCLEROTIC PLAQUE DELAMINATION

4.1 Introduction

Atherosclerotic plaque delamination depends both on the deformation and stress experienced by the arterial wall and on the interfacial strength between the plaque and the vascular wall. One measure of the interfacial strength is the critical energy release rate, which is the energy required to delaminate a unit area of the plaque from the underlying vascular wall. This critical energy release rate can be measured in plaque delamination experiments and can serve as an input to a mechanics model (such as the cohesive zone model) that describes the interfacial strength mathematically.

To this end, a finite element modeling and simulation approach for atherosclerotic plaque delamination experiments has been developed. In particular, plaque delamination experiments performed on apolipoprotein E-knockout (ApoE-KO) mouse aorta specimens are modeled in order to gain an understanding of the role of mechanical failure in human atherosclerosis because the ApoE-KO mouse aorta has been shown to develop atherosclerotic lesions similar in many respects to those seen in humans (Meir and Leitersdorf, 2004). It is noted that the modeling approach developed in this study can deal with mixed-mod delamination failure. The particular delamination experiments noted

above, in which a Mode I type delamination occurs due to the peeling of the delaminated portion of the plaque from the aorta wall, are used to demonstrate and validate this approach because of their availability and the lack of other types of experimental data in the literature. This study tries to establish the credibility and viability of this approach in order to provide a strong basis for its application to other clinically relevant failure modes such as those involving shear failure.

In the current study, the atherosclerotic plaque delamination phenomenon is investigated through modeling and simulation of experiments performed on ApoE-KO mouse aorta specimens in which a plaque is peeled off from an arterial wall. A three-dimensional (3D) finite element model for the experiments is developed, in which the Holzapfel-Gasser-Ogden (HGO) model (Gasser et al., 2006; Holzapfel, 2000b) in Section 2.2 for the bulk arterial material behavior and a mixed-mode CZM in Section 3.3 for the plaque-media interface behavior are adopted. Simulation predictions of the load vs. load-point displacement curve are compared with experimental measurements as validation for the proposed modeling approach. Also, uncertainties about the specimen geometry are analyzed in order to understand how these factors affect the predicted load vs. load-point displacement responses.

4.2 Experimental Procedure

The current study is focused on the modeling of atherosclerotic plaque deamination experiments performed on mouse aorta specimens reported in (Wang et al., 2011). In these experiments, ApoE-KO mice were fed a high-fat (42% of total calories) Western-style diet for 8 months, starting at the age of six weeks, in order to develop atherosclerosis throughout the aorta (Nakashima et al., 1994). At the start of the experiment, a small initial

delamination was carefully introduced by a scalpel at the proximal end of the plaque, so that the micro-clamp can clamp the plaque edge, as shown in Fig. 4.1. The plaque was delaminated in situ. Pins were placed at both ends of a specimen to prevent excessive outward motion of the aorta, as shown in Fig. 4.1c and Fig 4.2. The tissues surrounding and underlying the aorta provide considerable structural support and restrict the outward motion of the aorta during the delamination procedure; in particular, the dorsally-oriented intercostal branches prevent the outward motion of the thoracic aorta (Wang et al., 2011).

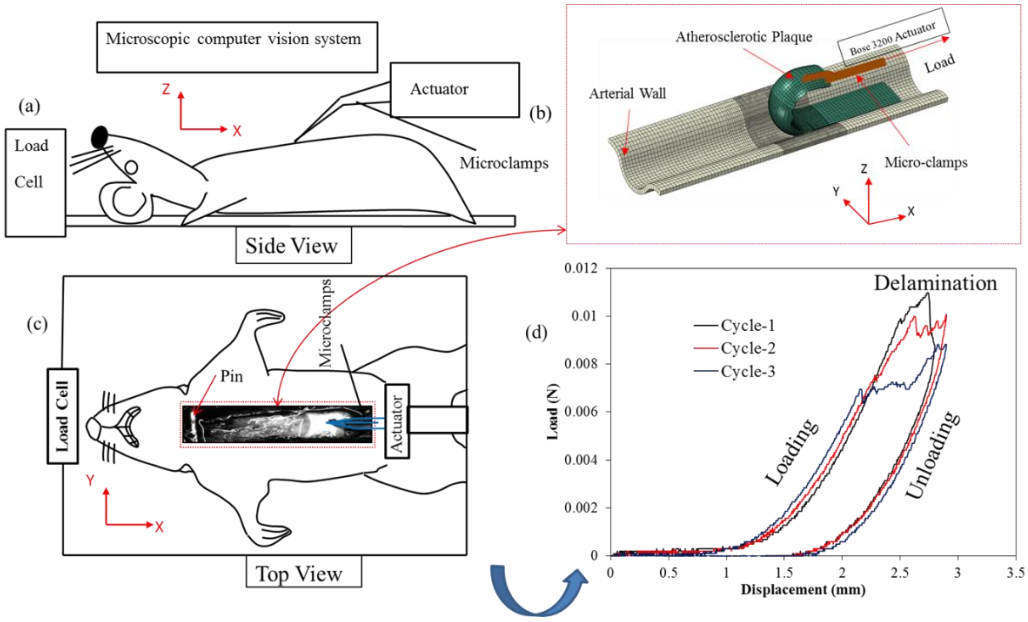


Fig. 4.1 A schematic of the atherosclerotic plaque delamination experimental setup: (a) Side view of the schematic diagram of the experiment, a mouse specimen on a loading table; (b) a schematic diagram of the experimental process represented by a finite element; ; (c) top view of the schematic diagram of the experiment; (d) three typical consecutive experimental load vs. load-point displacement curves.

A mouse carcass with exposed aorta was fastened to a small plate connected to the load cell of a Bose ELF 3200 for load data recording. The small delamination on the proximal end of the plaque was gripped by a pair of micro-clamps connected to the Bose ELF 3200 actuator, which applies sequential loading-delamination-unloading cycles, as

shown in Fig 4.1d. The delamination process was recorded by a computer vision system which was placed a certain distance above the mouse carcass, and one of the recorded images is shown in the center insert box in Fig. 4.1c. For each experiment, a load-displacement curve with multiple loading-delamination-unloading cycles was obtained, and three sequential loading-unloading cycles from specimen #1 are shown in Fig. 4.1d. After the experiment, the specimens were prepared for histological analyses, which reveal that the plaque delamination took place between the plaque and the underlying internal elastic lamina (IEL), instead of within the media (Wang et al., 2011).

4.3 Numerical Simulations of Atherosclerotic Plaque Delamination

4.3.1 Simulation Model

An important part of the plaque delamination simulation model is the geometric dimensions of the aorta (e.g. diameter, thickness of wall, length and curvature) and plaque (e.g. thickness and length of plaque along the longitudinal direction of aorta) since errors in the geometric dimensions will lead to errors in simulation predictions. Since limited geometric values were obtained from the delamination experiments being modeled in this study, several considerations and assumptions are found necessary to create the simulation model (the finite element model).

First, the digitized images from the plaque delamination experiments are used to measure certain geometry data directly, including the length and width of the plaque. Second, reference geometry data from the literature are considered in approximating the arterial wall thickness because the variation of thickness for mouse aorta with the same age, diet and genotype is small.

Based on these considerations, an approximate geometry model of the plaque specimen is created. The effects of the uncertainties in the geometric values will be examined in section 4.6.

4.3.2 Two Contributions to Define Geometry of Finite Element Model

a. Delamination Experimental Images

The width and length of the delamination area can be measured directly from the available experimental images. For example, one experimental image of specimen #1 is shown in Fig. 4.2. Considering the curvature of the lower face, the geometrical values for the plaque are measured from the upper face, in which W1, W2 and W3 are three values of the width used to approximate the cross-section of the mouse atherosclerotic plaque specimen, and L1 and L2 are the distances from the proximal end of the specimen to the positions where W1 and W2 are measured, respectively. The total length of the plaque specimen is determined by the distance from the left pinned end (the proximal end) to the right pinned end (the distal end) of the plaque specimen. The thickness of the plaque, T, can be estimated only at the proximal end from the experimental image. Thus, as an approximation, T is taken to be constant along the total length of the specimen in the finite element model. The radius R of the interface between the aortic wall and the plaque is also available only approximately from experimental images.

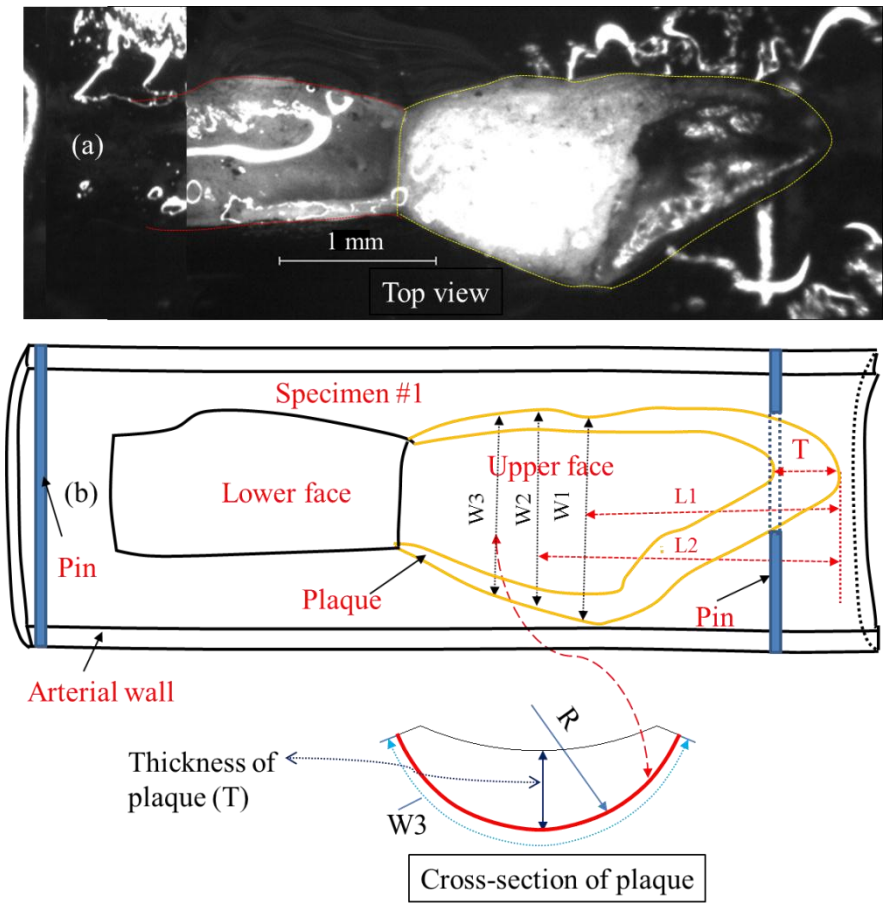


Fig. 4.2 An experimental delamination image of a mouse plaque specimen (specimen #1). The "upper face" is the separated surface pulled by the micro-clamp, and the "lower face" is the exposed surface. Scale bar=1 mm.

b. Geometry Values from the Literature

The literature provides some reference values for the aorta geometry useful in the current study. For example, reference (Gregersen et al., 2007) studied the remodeling of the zero-stress state of the aorta in apoE-deficient mice at the ages of 10, 28 and 56 weeks, in which aortic rings were excised from several locations along the aorta. The geometry values of the aortic rings at zero-stress state measured from mice at the ages of 28 and 56 weeks from reference (Gregersen et al., 2007) are employed in the current study to provide a range of approximate geometry values for mice at the age of 43 weeks which were used

in the delamination experiments being modeled in the current study. Therefore, for the arterial wall, the range of the inner circumference (C_i) is 1.4 mm to 2.8 mm, the range of the outer circumference (C_o) is 2.0 mm to 3.3 mm, and the range of the thickness is 0.08 mm to 0.16 mm.

4.3.3 FE Model of the Plaque Delamination Experiments

For the in-situ experiments, it is difficult to obtain the geometry of the atherosclerotic plaque and the arterial wall, not only because of the complexity of the geometry, but also because of the very small dimensions of the mouse aorta. The geometrical dimensions of the width and length of the atherosclerotic plaque are more accurate because these values can be directly measured from the experimental images, as shown in Fig. 4.2. In addition, the delaminated area between the plaque and underlying vascular wall shows large variations during the delamination process. Therefore, in building the finite element model, the two contributions in section 4.3.2 are incorporated into the model based on available information. The resulting 3D finite element model with a reasonable approximation of the actual specimen contains an asymmetrical atherosclerotic plaque as shown in Fig. 4.3.

In the model, the widths of the plaque are measured at different locations along the longitudinal direction of the arterial wall from the experimental images, as shown in Fig. 4.2. The thickness of the plaque is taken as a constant value for the delamination length of each loading-delamination-unloading cycle (which is around 0.2 mm).

In the experiments, both ends of the specimen were constrained by pins, but the pins could not completely constrain the movement of the specimen along the longitudinal direction, as if the pinned vessel acted as an elastic foundation in the longitudinal direction.

Therefore, in the finite element model, the arterial wall is made longer than the plaque, so that the extra length of the arterial wall can provide the needed freedom to model this elastic foundation effect. For simplicity, the lengths of the arterial wall on either side of the plaque, from the two ends of the plaque to the two ends of the arterial wall, are set to equal half the length of the plaque, as shown in Fig. 4.3a.

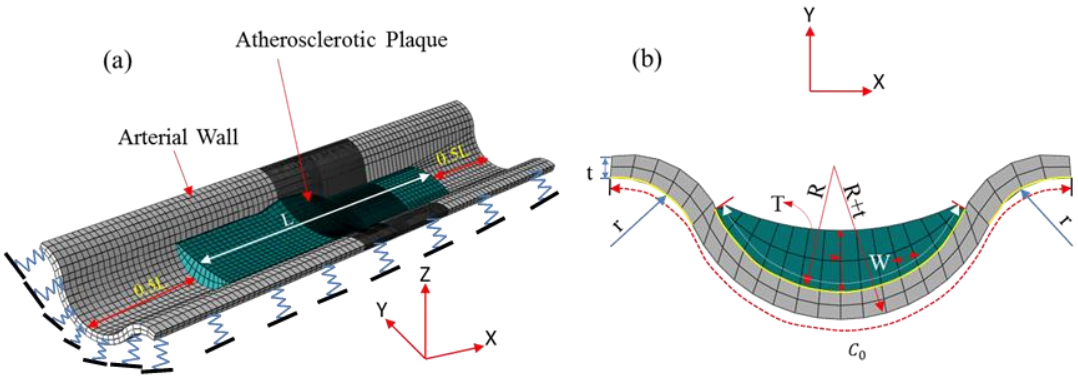


Fig. 4.3 A FE model of the mouse aorta (specimen #1): (a) a FE model for delamination simulation, where L is the length of the atherosclerotic plaque; elastic springs under the arterial wall in x, y and z directions. (b) a cross-sectional view of the aorta and parameters, where r is the radius of the aortic wall curvature away from the plaque, R is the radius of curvature of the interface between the plaque and the arterial wall, t is the thickness of the aortic wall, W is the width of the plaque, T is the height of the atherosclerotic plaque, and C_o is the total circumferential width of the aortic wall.

4.3.4 Boundary Conditions

Because perivascular adipose tissue (Szasz et al., 2013; Verhagen and Visseren, 2011) and other surrounding connective tissues are in close association with the arterial wall and serve as the vascular bed, they are expected to constrain the movement of the arterial wall. Due to limited information regarding the structure and material properties for those tissues, the effects of the underlying tissues are modeled by an elastic foundation under the aortic wall. To this end, the boundary of the arterial wall is approximated by elastic springs that connect points to the ground in x, y and z directions, as shown in Fig.

4.3a. The proximal and distal ends of the wall are approximated by fixed boundary conditions.

The equations used to describe the response of the tissues connecting to the arterial wall are $F_x = k_x u_x$, $F_y = k_y u_y$ and $F_z = k_z u_z$. The parameters k_x, k_y, k_z are the stiffness values, u_x, u_y, u_z are the displacements, and F_x, F_y, F_z are the spring forces in the three directions, respectively.

Reasonable values of the spring stiffness are chosen as part of a numerical identification procedure that matches simulation predictions of the overall load vs. load-point displacement curve with experimental measurements. In selecting the spring stiffness values, only the loading phase of the load vs. load-point displacement curve is used.

Fig. 4.3 shows a complete finite element model using the geometry described earlier. The mesh is generated using ABAQUS (ABAQUS, 2013). The arterial wall and plaque regions are meshed with 8-node brick elements, C3D8H, while the cohesive zone interface is meshed with zero thickness 8-node 3D user-defined elements. A layer of cohesive elements is placed along the delamination path, starting from the initial crack front to the end of the plaque. It is noted that while the CZM approach can handle material separation without a given separation path, it will greatly save the computational cost if the separation path is not part of the simulation prediction. In the current study, since the material separation path in the experiments being simulated is known in advance, the delamination path is taken as known in order to save computational effort and to avoid complexities associated with the need to predict the separation path. The global bulk element size (for the arterial wall and plaque) is 0.1 mm and the cohesive element size is 0.02 mm.

4.3.5 Parameter Value Identification

The parameter values for the bulk arterial material, the elastic springs, and the CZM, are obtained through an inverse identification procedure that matches simulation predictions of the overall load vs. load-point displacement curve with experimental measurements. Since the current study involves many parameters, and only a limited amount of experimental data are available, a fully automated inverse procedure (Chen et al., 2014) will be very time consuming and thus was not employed. Instead, approximations were made (e.g. most of the bulk material parameter values were set to be the same for the arterial wall and for the plaque), simple values were chosen (e.g. single-digit rounded values were chosen for the elastic foundation spring constants), and a manual numerical procedure (Chen et al., 2013) was performed. The experimental load vs. load-point displacement curve for the first loading-delamination-unloading cycle from specimen #1 and reference parameter values from the literature are used as the input data for the identification procedure. In this study, a set of parameter values is determined when the average error, $e_{avg} = \left[\sum_{i=1}^{N}\left(\frac{f_{sim}-f_{exp}}{f_{exp}}\right)\right]/N$, between simulation predicted reaction forces, f_{sim}, and experimentally measured reaction forces, f_{exp}, is less than 10%, where N is the number of data points which spread over the loading, delamination and unloading phases of the load-displacement curve for the first loading cycle. A relatively large error (10%) is accepted because the match between simulation predictions and experimental data is expected not to be perfect due to several uncertainties in the simulation model and input data.

4.3.6 Parameter Values for the HGO Model and Elastic Springs

Reference (Van Herck, 2009) investigated the stress strain response of aortas from $ApoE^{-/-}Fbn1^{+/C1039G}$ and $ApoE^{-/-}$ mice that were fed with normal chow or Western-style (high-fat) diets for 10 and 20 weeks. It was observed that the stiffness of the mouse aorta not only increases with age but also correlates with the diet. For the experiments being modeled in the current paper, the mice were fed a Western-style diet for 34 weeks, which means that the stiffness of the mouse aorta is expected to be greater than those reported in Reference (Van Herck, 2009). Similarly, the values of the HGO model parameters reported in the literature for mouse aorta refer to mice at the age near 10 weeks (Collins, 2011; Collins, 2012; Eberth, 2009), which means that they are not directly applicable in the current study.

Therefore, the values for HGO model parameters for the bulk material and the values of the stiffness of elastic springs are determined based on values suggested in the literature (Collins, 2011) and by matching simulation predictions with measurements using the loading phase of the load-displacement curve from the 1st loading-unloading cycle of specimen #1 ($e_{avg} = 6.37\%, N = 54$), as shown in Fig. 4.4a. In carrying out this identification procedure, the deformations of arterial wall and plaque are also checked to make sure that they are consistent with those observed experimentally.

The arterial wall and plaque are treated as two layers of heterogeneous materials. As a first-order approximation, their HGO model parameter values are chosen mostly to be the same, due to the lack of proper literature reference data and the lack of sufficient experimental data for more adequate inverse identification. These HGO model parameter values are shown in Table 1. The values of the stiffness of elastic springs in the elastic

foundation under the arterial wall are listed in Table 2. Meanwhile, with the same HGO model parameter values (Table 1) identified from specimen #1, the values of the elastic springs for specimen #2 (Table 2) were obtained through matching simulation predictions with measurements using the loading phase of the load-displacement curve from the 1st loading-delamination-unloading cycle of specimen #2, as shown in Fig. 4.4b. The stiffness values are smaller than those for human and porcine adipose tissues (which have elastic moduli of approximately 1 kPa) (Alkhouli N, 2013; Comley K, 2009).

Table 4.1 Material parameters of mouse arterial wall and plaque identified from specimen #1

	μ (kPa)	k_1 (kPa)	k_2	κ	r (degree)
Arterial wall	4	4e3	525	0.226	46.4
Plaque	4	4e3	525	0.226	27.2

Table 4.2 Stiffness of spring for specimen #1 and specimen #2

Specimen	$k_x(N/mm^3)$	$k_y(N/mm^3)$	$k_z(N/mm^3)$
#1	1e-4	1e-4	1e-4
#2	3e-5	5e-5	1e-4

The simulation predicted von Mises stress contours for three typical points along a loading-delamination-unloading cycle from specimen #1 are shown in Fig. 4.5. The stress contour levels shown in the zoomed-in views (a), (b) and (c) are consistent with the corresponding loading levels in the load-displacement diagram. For example, the loading level in (b) is the highest and is sufficient to grow the delamination, and the resulting von Mises stress field shows that it has the highest contour level of the three cases. In all three cases, the highest stress contour level occurs in the middle portion of the plaque near the

delamination front, which is expected. In (b), the highest stress level is located somewhat behind the delamination front, which is consistent with the fact that the loading level in (b) occurs somewhat after the peak load is reached in the load-displacement diagram.

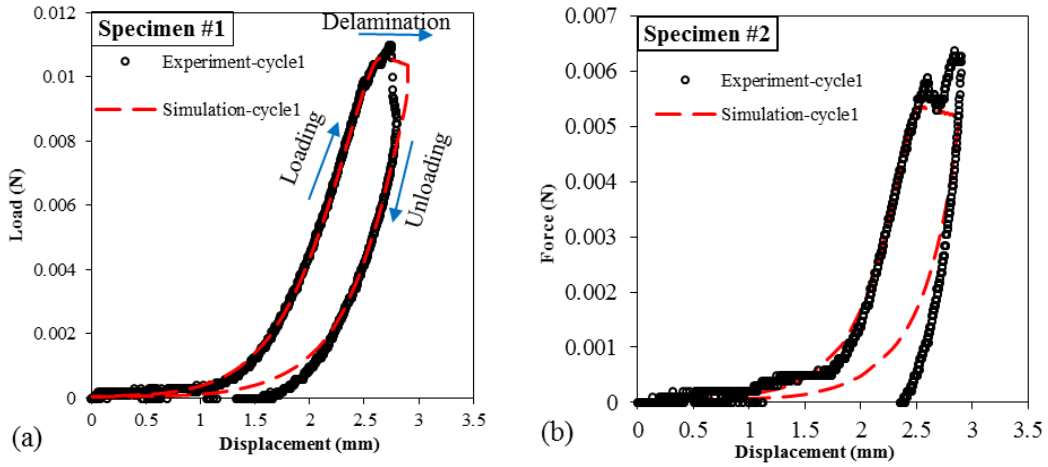


Fig. 4.4 (a) The simulated load-displacement curve of the first loading-unloading cycle from specimen #1 is compared with the measured curve, $G_c = 0.019\ \mathrm{N/mm}$. (b) The simulated load-displacement curve of the first loading-unloading cycle from specimen #2 is compared with the measured curve, $G_c = 0.01\ \mathrm{N/mm}$. The entire cycle includes the loading phase in which the plaque is pulled without delamination, the delamination phase in which the plaque is pulled and separated from the underlying internal elastic lamina (IEL), and the unloading phase in which the plaque is returned to the initial position.

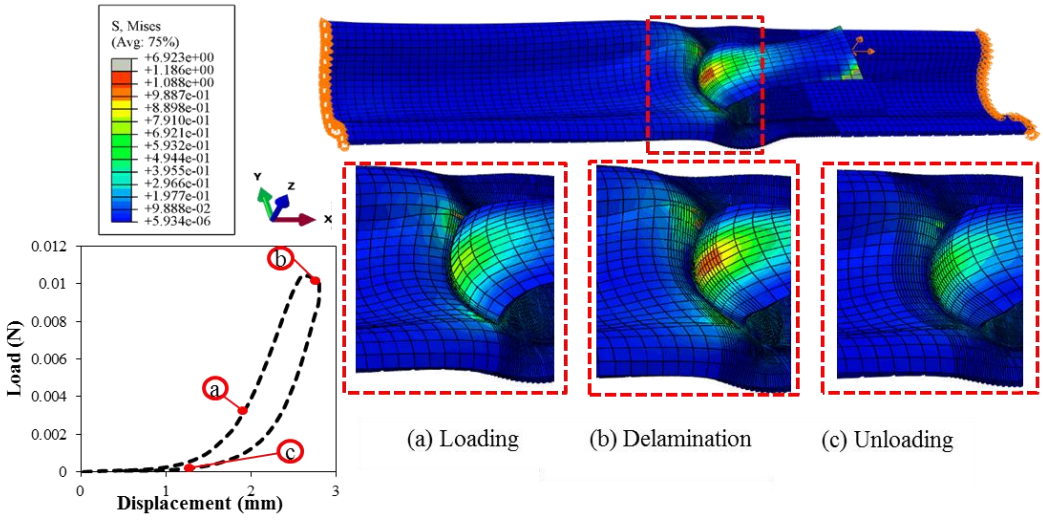


Fig. 4.5 von Mises stress (MPa) contours for three typical points of loading-unloading cycle of plaque delamination simulation from specimen #1.

4.3.7 CZM Material Properties

In the current study, the delamination of atherosclerotic plaque is approximated as a pure Mode I process (Wang et al., 2011), in which the dominant cohesive traction is the tensile cohesive traction normal to the plane of delamination. Therefore, for simplicity, the values of G_{IIc} for all cycles are set to be equal to G_{Ic}, because the exact value of this Mode II parameter in a Mode I event has negligible effect on the simulation results. Due to the variation in geometry of the delamination area and material heterogeneities along the longitudinal direction of the aorta, the energy release rate in pure Mode I, G_{Ic}, varied from one delamination cycle to another (Wang et al., 2011). The measured G_{Ic} values are used as the input cohesive parameter values.

The rest of the CZM parameter values, as shown in Table 3, are selected based on values suggested in the literature, such as the tensile strength of the interface between the plaque and the underlying tissue (the arterial wall) (Gasser and Holzapfel, 2006), and by matching simulation predictions of the load-displacement curve with measurements using the delamination phase of the first loading-delamination-unloading cycle of specimen #1 (as shown in Fig. 4.4a). Care was taken to ensure that the deformations of the arterial wall and the plaque during the delamination phase are consistent with those from experimental measurements, as described earlier for determining parameter values of the HGO model for the bulk arterial wall and plaque behavior.

Table 4.3 CZM parameter values

CZM parameters	T_3^0 (MPa)	T_{shear}^0 (MPa)	K (N/mm^3)	α
Values	0.14	0.14	1e4	1.2

For the numerical convergence, the stiffness of the cohesive zone model and the size of the cohesive element need to be taken into consider (Chen et al., 2013; Chen et al., 2014).

(a) Stiffness of the Cohesive Element

In order to avoid introducing a fictitious structure compliance, the stiffness of the cohesive surface between the plaque and the arterial wall must meet the condition (Chen et al., 2013; Chen et al., 2014):

$$K \geq \frac{aE_3}{\mathrm{t}} \tag{4.1}$$

where E_3 is the through-thickness Young's modulus of the bulk material, t is the thickness of the plaque or aorta wall, and a is a parameter much larger than 1 (e.g. 50). In the current study, the maximum thickness was chosen where t is equal to the thickness of the plaque. A suitable stiffness must be selected to inhibit numerical convergence difficulty and spurious oscillations of the tractions values in the elements.

It was reported in Reference (Asawinee Danpinid, 2009) that the Young's modulus of the arterial wall in six mice in vivo for elastin, elastin-collagen and engaged collagen fibers has a mean values of 91.6 kPa, 229.0 kPa and 137.5 kPa, respectively. Considering these stiffness values and the thickness of the plaque in the current study, it is found that a value of 10^4 N/mm^3 for K is sufficient.

(b) Length of the Cohesive Element

The length of the cohesive zone l_{cz} is defined as the distance from the delamination front to the point ahead of the front where the maximum cohesive traction is attained. In order to predict the cohesive zone length l_{cz} of the interface between the materials of

plaque and arterial wall, a form related to the fracture properties of the interface is shown below (Turon et al., 2006):

$$l_{cz} = ME\frac{G_c}{(T_c)^2} \quad , \quad l_e = \frac{l_{cz}}{N_e} \tag{4.2}$$

where G_c is the critical energy release rate, E is the Young's modulus of the material, T_c is the maximum interface strength, and M is a parameter that depends on the cohesive zone model. For cycle 1 of specimen #1, G_c is equal to 0.019 N/mm, T_c has the value as 0.14 MPa, and M was chose equal to unity, Using equation (4.2) with Young's modulus of elastin, elastin-collagen and engaged collagen fibers, respectively, the values of the cohesive zone length are 0.09 mm, 0.22 mm, and 0.13 mm. When the number of elements in the cohesive zone, N_e, is chose as 5, the cohesive element size in the direction of crack propagation, l_e, is equal to 0.02 mm, 0.04 mm and 0.03 mm for the three values of the Young's modulus , respectively. In the current study, a cohesive element size of 0.02 mm is chosen.

4.4 Convergence Analysis

A convergence study was performed on the bulk material element and the cohesive element in order to exclude mesh dependency effects. Mesh 1 is a coarse mesh with 3,472 nodes and 1,972 brick elements (C3D8H), mesh 2 (the reference mesh) is refined from Mesh 1 (the element size in Mesh 2 is half of that in Mesh 1, along x, y and z directions) with 19,446 nodes and 14,136 brick elements, and mesh 3 is refined from mesh 2 with 119,365 nodes and 99,423 brick elements (the cross-sections of three meshes are shown in Fig. 4.6a).

The cohesive element size is dictated by the bulk material element size along the delamination path. Specifically, the cohesive element size, l_e, is 0.04 mm, 0.02 mm, 0.01 mm, respectively, for the three different meshes. It is observed that, from one mesh to another, there is little change in the predicted loading and unloading phases of the load-displacement curve, as shown in Fig. 4.6b. The average value of the pulling load during the delamination phase is constant and defines a plateau, which decreases with the decrease of the element size. The average relative errors for mesh 1 and mesh 3 compared to mesh 2 are 3.6% and 2.3%, respectively. Overall, mesh 2 is found to give reasonably converged predictions.

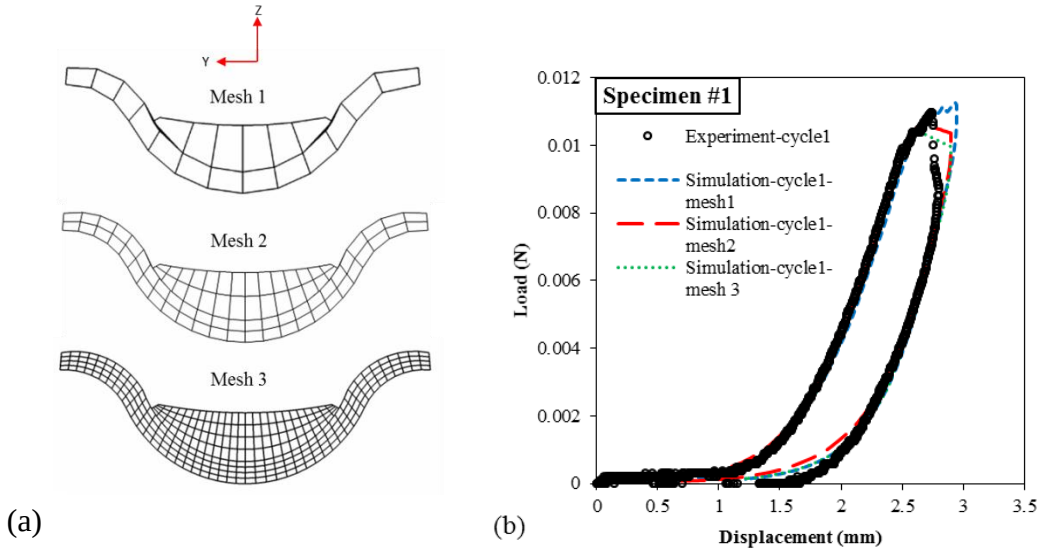


Fig. 4.6 (a) Cross-section of three different meshes, (b) predicted 1st-cycle load-displacement curves using the three meshes, with comparison to the experimental curve.

4.5 Prediction and Validation

Simulation predictions and validation of the predictions are performed for loading-delamination-unloading cycles 2 and 3 from both specimen #1 and specimen #2, using the

HGO model and CZM parameter values determined according to the parameter identification procedure, based on the 1st loading-delamination-unloading cycle of the experimental load-displacement curve for specimen #1. The stiffness values of the elastic foundation springs for the two specimens are determined, respectively, from cycle 1 of each specimen, and are listed in Table 2.

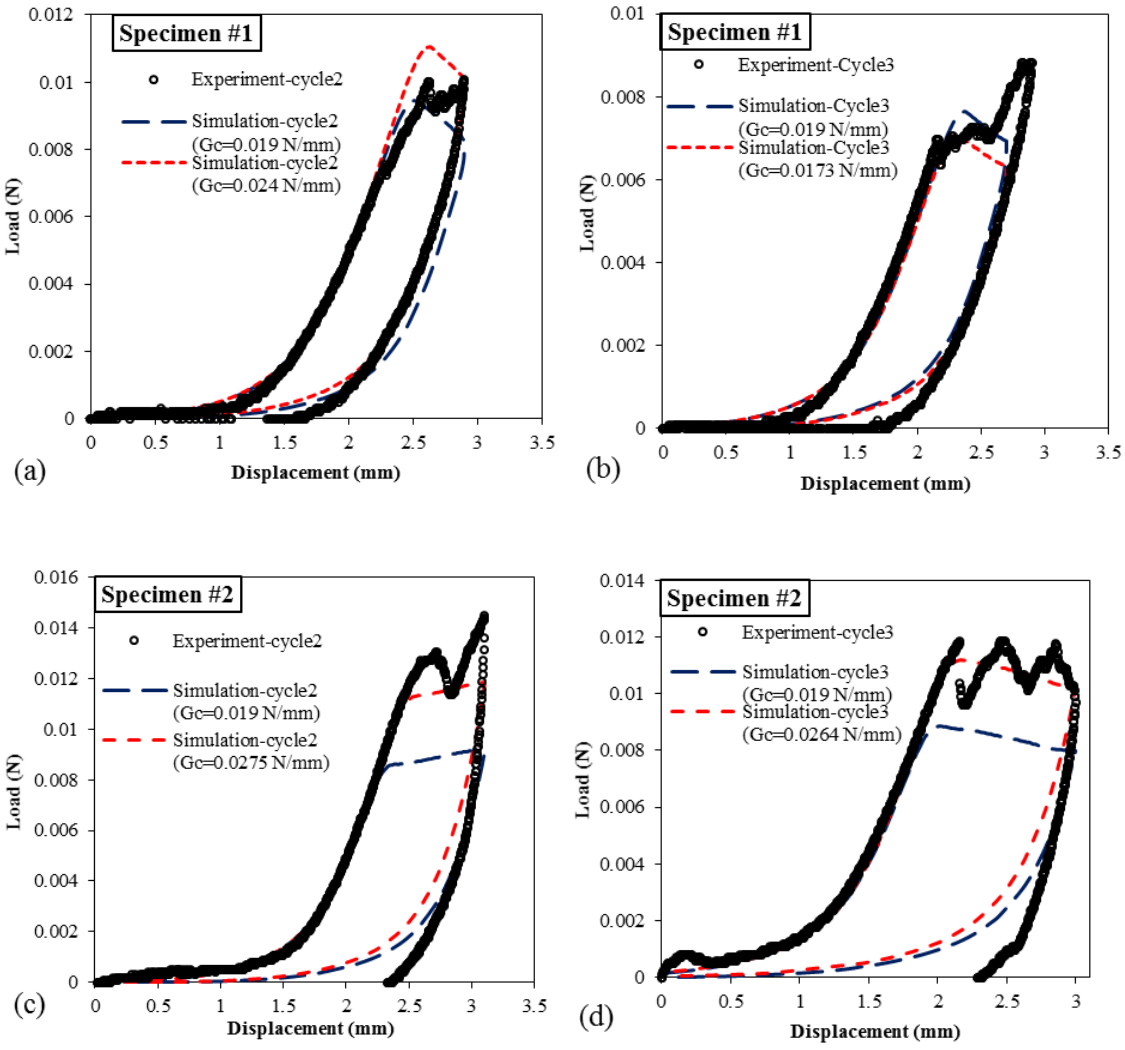


Fig. 4.7 Comparisons of the predicted and measured load-displacement curves for loading-unloading cycles. (a) cycle 2 and (b) cycle 3 of specimen #1; (c) cycle 2 and (d) cycle 3 of specimen #2.

Two simulations for each cycle are carried out due to two input choices for each cycle. Specifically, for each cycle, there are two choices for the critical energy release rate input value: (1) the experimental value from the corresponding cycle (see the red short dashed line in Fig. 4.7), and (2) the value is kept the same as in cycle 1 of specimen #1 (see the blue long dashed line in Fig. 4.7). The first choice is more reasonable because it reflects the variation of the experimental critical energy release rate value from cycle to cycle. Simulations with the second choice are made for comparison purposes.

It can be seen from Fig. 4.7 that the simulation predictions using the critical energy release rate from the corresponding loading cycles provide better predicted average values for the load during the delamination phase of the loading cycle. There are some differences between the predictions and measurements, especially for the delamination and unloading phases. There are several possible reasons for these differences. In the experiments, the tissue along the delamination path may not be homogeneous. It may contain weak material (e.g., lipid cores) and strong material (e.g., bridging fibers and calcification in the tissue), which can lead to oscillations in the delamination load. In the simulations, however, material inhomogeneity is not taken into consideration, thus oscillations in the delamination load are not predicted. The larger difference in the unloading curve is believed to be caused by the fact that the HGO model is not capable of modeling the viscoelastic behavior in the bulk material, while in the delamination experiments the viscoelastic effect may be non-negligible. Moreover, the differences may be caused by the approximations and simplifying assumptions made in the simulation models due to the lack of experimental data for geometrical dimensions and material model parameters, and by the choices of the material models themselves. Overall, the simulation predictions match

reasonably well with the experimental measurements. Thus, it can be said that a good validation for the CZM-based simulation approach for the plaque delamination process has been achieved, although further improvements in the overall simulation model are still necessary.

4.6 Analysis of the Effects of the Geometric Uncertainty

There are several uncertainties in the simulation model for the plaque delamination experiments, which may partly be responsible for the differences observed in the comparisons between simulation predictions and experimental results shown in Fig. 4.7. Besides uncertainties in the material parameter values, a key uncertainty is in the geometry of the mouse aorta. The effects of this uncertainty are analyzed in this section and specimen #1 is chosen for this purpose.

In the simulations, the thickness of the plaque and curvature of the arterial wall are taken to be constant along the length of the aorta due to the lack of experimental data. In reality, the thickness of the plaque and curvature of the arterial wall vary along the longitudinal direction of the aorta. To gain some insight into the effect of plaque thickness on simulation predictions, three plaque thickness values are considered: 0.15 mm (thickness-1), 0.26 mm (thickness-2) and 0.35 mm (thickness-3) (Fig. 4.8a). Furthermore, to study the effect of the aortic curvature in the cross-section on simulation predictions, three shapes of the cross-section are considered based on the curvature of the aorta below the plaque: 0.00 mm^{-1} (Curvature-1), 1.69 mm^{-1} (Curvature-2), and 2.22 mm^{-1} (Curvature-3) (Fig. 4.8c). All other aspects of the simulation model stay the same.

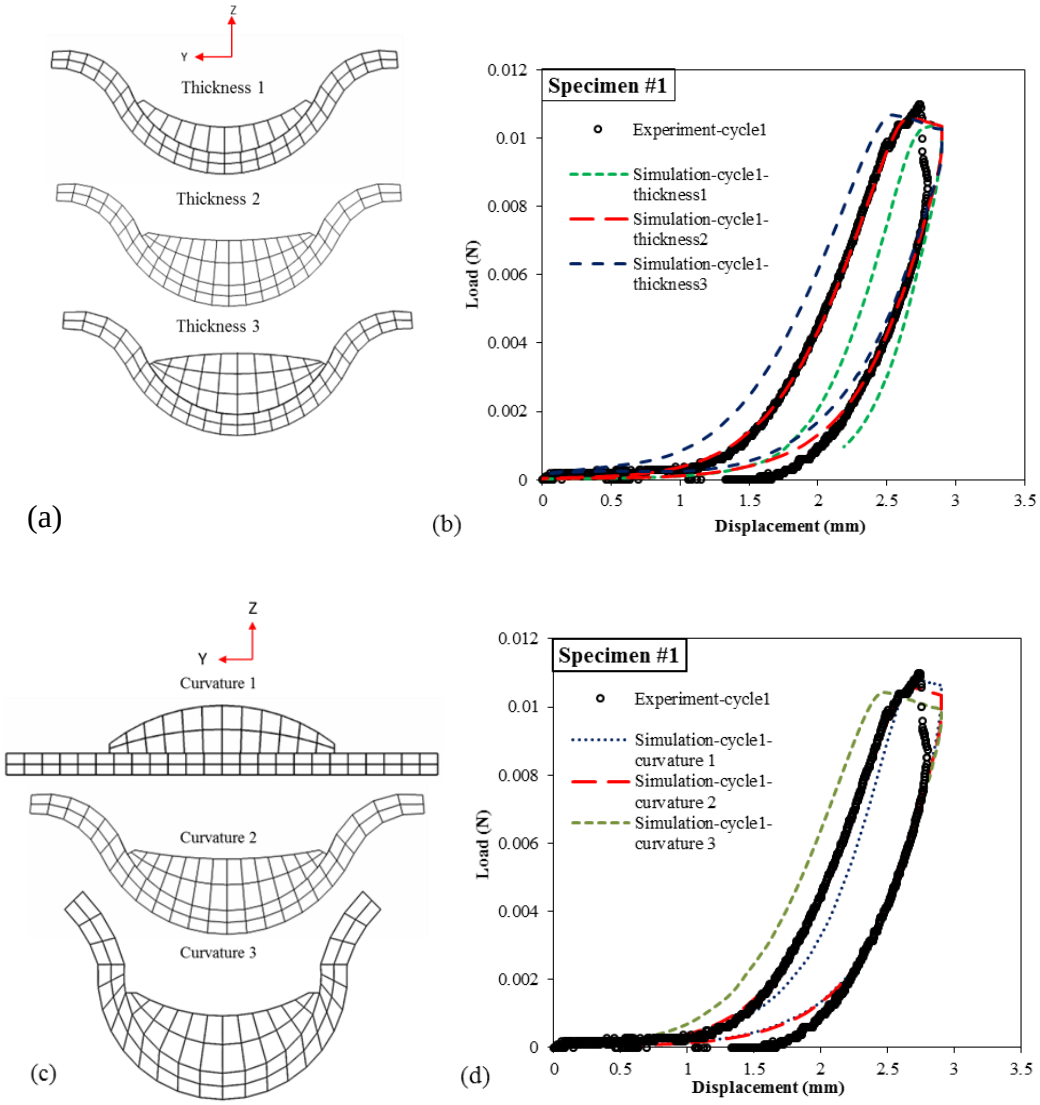


Fig. 4.8 Analysis of the effects of the geometric uncertainty: (a) The cross-sections of finite element models with three typical atherosclerotic plaque thicknesses. (b) Predicted load-displacement curves from simulations with three different thicknesses. (c) The cross-sections of finite element models with three typical atherosclerotic plaque curvatures. (d) Predicted load-displacement curves from simulations with three different curvatures.

The simulation predicted load-displacement curves are shown in Fig. 4.8 along with experimental data. It is seen that the predicted maximum load is only slightly affected by the plaque thickness, as shown in Fig. 4.8b. However, the loading and unloading phases (especially the loading phase) of the load-displacement curve are strongly affected by the

plaque thickness. The reason for these observed thickness effects seems to be related to the fact that when the thickness is changed, the structural stiffness of the model is changed (but not the delamination resistance of the interface), which is why the loading/unloading response is strongly affected (but not the peak load, which is more dictated by the delamination resistance).

In addition, the unloading phase of the load-displacement curve is not much affected by the curvature, but the loading and delamination phases of the load-displacement curve are more strongly affected by the curvature, as shown in Fig. 4.8d. A straightforward explanation for the predicted effects of the curvature is not clear at this time. This is because, when the curvature changes, several possibly coupled effects may be involved, including differences in the reactions of the foundation springs, the effects on the overall structural stiffness, and the effects on the energy release rate.

4.7 Conclusions

Plaque delamination often occurs at the shoulder region of the fibrous cap. Studies of atherosclerotic plaque delamination in mouse specimens provide a way to understand the mechanisms of arterial failure and damage evolution at material layer interfaces. There are studies that focus on the analysis of stress-strain behavior and tissue dissection inside the arterial material (Ferrara and Pandolfi, 2010; Gasser and Holzapfel, 2007; Gasser and Holzapfel, 2006), but few studies have investigated the delamination of atherosclerotic plaque from the underlying arterial wall.

In the present work, a finite element based modeling approach for simulating atherosclerotic plaque delamination events has been developed and demonstrated.

Simulations of plaque delamination experiments on mouse aorta specimens have been carried out, in which the HGO model for the bulk arterial material behavior and the CZM for the delamination behavior along the plaque-media interface are adopted. The 3D geometry model is generated based on images from the plaque delamination experiments and on geometric values from the literature.

Parameter values for the HGO model and the CZM were determined based on values suggested in the literature, by matching simulation predictions of the first loading-delamination-unloading cycle of the load-displacement curve from specimen #1 with the measured curve, and by requiring that the predicted deformations be consistent with those from experimental measurements. As validation of the CZM approach, the parameter values identified from the first loading-delamination-unloading cycle of specimen #1 were employed for one group of simulations for loading cycles 2, 3 from specimen #1 and another group of simulations for loading-unloading cycles 2, 3 from specimen #2. The simulation predictions of the load-displacement curves for these cycles were found to match reasonably well with experimental curves.

Furthermore, the simulation model was used to study the effects of geometric uncertainty on simulation predictions. It was found that the predicted load in the delamination phase was not affected by the plaque thickness, but it was strongly affected by the curvature of the arterial wall in cross-section.

While the geometric uncertainty and associated simplifications and approximations for the simulation model may be partly responsible for the differences seen in the comparisons between simulation predictions and experimental results, approximations in modeling the bulk material behavior for the arterial wall and for the plaque are also

expected to contribute to the observed differences. First, it is known that the mechanical behavior of the plaque is in general different from that of the arterial wall. In the current study, the plaque was modeled using the HGO constitutive model which was developed for the arterial wall. The HGO model may not be appropriate for the plaque because the histological components of the plaque are different from those of the arterial wall (Huang et al., 2001). Hence, a more suitable constitutive model for the plaque is needed. Second, due to the lack of experimental data, several of the HGO model parameter values for the arterial wall and for the plaque were simply chosen to be the same in the current study, which may be grossly inadequate. Third, adventitia, media and intima are three layers in the arterial wall which in general have different material properties, but they are lumped together in the current study as a single layer. Fourth, experimental data show the existence of hysteresis behavior in the load-displacement curve, which suggests that there may be a need to consider the viscoelastic behavior of the arterial wall and the plaque.

CHAPTER 5

EXPERIMENTAL AND NUMERICAL STUDIES OF MIXED-MODE AND MODE I DELAMINATION OF ARTERIAL WALL

5.1 Introduction

In the previous chapter, a mouse atherosclerotic plaque delamination test was conducted. This experiment is different from the arterial tissue peeling test performed by Sommer (Sommer et al., 2008). In order to explore mechanisms of the two types of delamination tests (a "mixed-mode" type and a "mode I" type), the comparison of these two tests is conducted and the findings from the experimental and numerical studies of the two types of tests will provide more guidance for further investigations of arterial tissue failure.

For the numerical simulation of arterial layer delamination, numerous studies employed a CZM approach to characterize interfacial debonding and delamination processes of fiber-reinforced composite materials (Roy and Dodds, 2001; Turon et al., 2006). This method has also been implemented to study the failure of arterial tissue in two dimensions (2D) (Ferrara and Pandolfi, 2010; Gasser and Holzapfel, 2006) and three dimensions (3D) (Leng et al., 2015a; Leng et al., 2015b; Leng et al., 2016).

It is well known that elastin is the major load bearing structural component of the arterial wall at low strain and that collagen fibers contribute to the stiffening of the arterial

tissue at high strain (Ferrara and Pandolfi, 2010; Zhou et al., 2015). With the advantage of quantifying the separate mechanical contribution of each component to the overall mechanical behavior of the arterial tissue, the Holzapfel-Gasser-Ogden (HGO) model has widely been employed for modeling the mechanical behavior of arterial wall and calculating the local stress of the vascular cells in the arterial wall under large deformation (Ferrara and Pandolfi, 2010; Leng et al., 2015b).

Existing studies in the literature have investigated the dissection of the arterial wall, but experimental investigations of arterial wall delamination events and the analyses and numerical simulations of such events have been limited. To this end, delamination experiments on porcine abdominal aorta focusing on mixed-mode and mode I failures are performed. In addition, the interfacial strength and critical energy release rate of the interface within the media are quantified, and these experiments have been simulated numerically using the finite element method and the cohesive zone model approach. In the current study, a three-dimensional (3D) finite element model for the experiments is developed, in which the Holzapfel-Gasser-Ogden (HGO) model (Gasser et al., 2006; Holzapfel, 2000b) in Section 2.2 for the bulk arterial material behavior and an exponential CZM in Section 3.4 for the interface (inside the media layer) behavior are adopted. Through the simulation of arterial tissue delamination, the CZM method can be validated by the comparison of loading-delamination-unloading curves and the distances from the delamination front to the initial front between simulation and experimental measurements. Meanwhile, the level of constraint along the delamination path and the shape of delamination front are investigated, which focus on the study of the effects from the interfacial strength and critical energy release rate of the interface of arterial material.

Finally, the dominant fracture mode of the two types of arterial material delamination processes has been discussed in order to better understand the arterial tissue failure mechanism.

5.2 Experimental Procedure

The delamination experimental protocol in this study and the method to obtain the critical energy release rate follow our previous studies (Wang et al., 2013; Wang et al., 2014; Wang et al., 2011). One set of intact kidneys was obtained from the local slaughterhouse, rinsed in iced phosphate-buffered saline (PBS) solution and transported back to the laboratory. The abdominal aorta was isolated from the surrounding tissue, washed in PBS and dissected from the perivascular tissue. An approximately 30 mm long segment was cut, followed by a radial cut imposed onto the sample along the vessel axis, yielding a strip. Two groups of specimens oriented at the angle of 0° and 90° with respect to the circumferential vessel axis were cut from two porcine aortas (Fig. 5.1), respectively.

There are twelve specimens for each group, half of the twelve specimens oriented at the angle of 0° with respect to the circumferential vessel axis were used for mixed-mode delamination and the remainder were used for mode I delamination. The same experiments were also performed on specimens cut at an angle of 90° with respect to the circumferential vessel axis, as shown in Fig. 5.1. In each case, to initiate a delamination process in the media layer of the arterial wall, a small initial delamination flaw with a straight delamination front was carefully introduced at one end of the specimen inside the media layer. In the “mixed-mode” experiment (see Figs. 5.2a and 5.2c), the bottom surface of the lower portion of the specimen was glued to a glass plate in order to restrict its motion during loading, and the proximal end of the upper delaminated portion was peeled away

by a micro-clamp. During the delamination process, the delaminated upper portion became almost parallel to the lower portion and to the not-yet delaminated interface (Fig. 5.2c). In the "Mode I" experiment (see Figs. 5.2b and 5.2d), the proximal end of one of the two initially separated portions of the specimen was fixed by tissue glue to a glass plate and the proximal end of the other separated portion was pulled away by a micro-clamp. During the delamination process, the two delaminated portions stay parallel to each other but are approximately perpendicular to the not-yet delaminated interface (Fig. 5.2d).

During each experiment, the prescribed displacement and reaction load were recorded via the system actuator and load cell (Bose ELF 3200, Biodynamic Co, MN). The delamination process was recorded by a computer vision system in which two cameras were perpendicularly positioned to get both front and side views of the specimen.

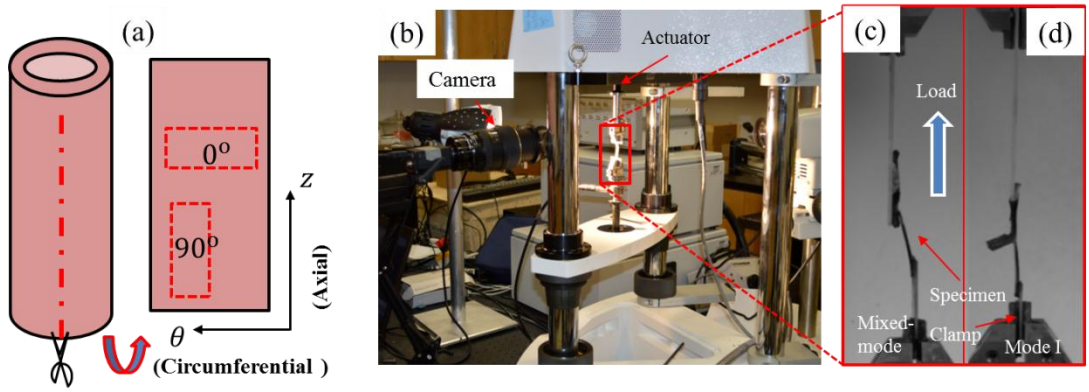


Fig. 5.1 Schematic of experimental setup. (a) A radial cut was made on the porcine abdominal aorta and strips oriented at the angle of 0° and 90° with respect to the circumferential vessel axis were obtained; (b) Experimental setup of delamination tests; (c) mixed-mode and (d) mode I delamination experiment setup (zoomed-in view).

5.3 Numerical Implementation

Simulations of the arterial delamination process are implemented via the general-purpose finite element software ABAQUS 6.13 (ABAQUS, 2013). The mechanical data in

terms of the load vs. displacement relationship from the first cycle of the media delamination experiment was used for the identification of the HGO constitutive model. Simulations of loading-delamination-unloading for the subsequent cycles were performed by using the intact set of identified parameters, validating the CZM-based approach by comparing the numerical predictions of load-displacement curves and distances from delamination front to the initial front with experimental measurements.

5.3.1 Finite element model

The images (Fig. 5.2a, 5.2b) taken during the experiments were used to reconstruct the material geometry (Fig. 5.2c, 5.2d). The delamination areas during a delamination experiment were quantified directly from the experimental images taken at different times during the testing.

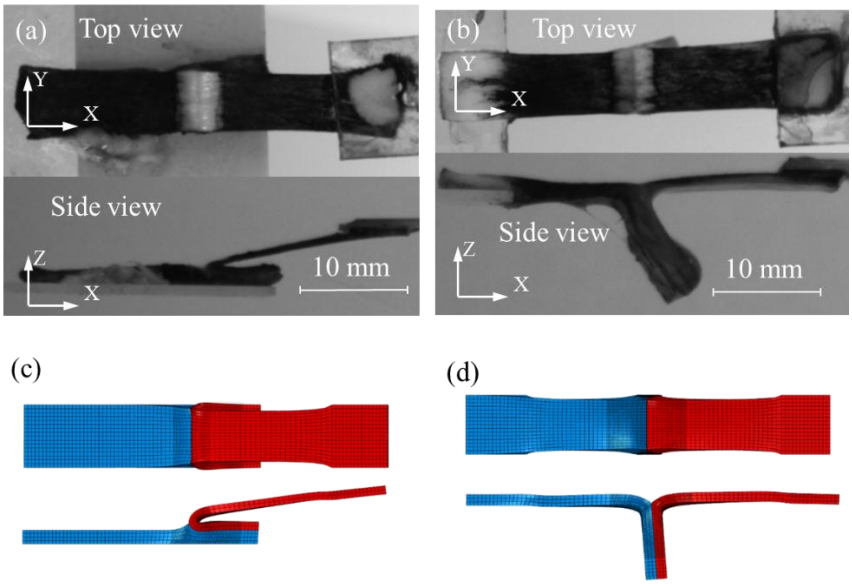


Fig. 5.2 Images of (a) mixed-mode and (b) mode-I delamination experiments on porcine abdominal aorta specimens, and deformed shapes of (c) the mixed-mode and (d) mode-I specimens from finite element simulations. The right delaminated part of the specimen (red section) contains intima and part of media, and the left delaminated part (blue section) contains adventitia and part of media. The delamination of aorta propagated inside the media layer.

Meshing

The arterial layers are meshed with eight-node brick elements (C3D8H). The cohesive interface is meshed with zero thickness eight-node 3D user-defined elements, which are placed along the delamination path starting from the initial delamination front to the end of the media. The global size of the element for the arterial wall is 0.4 mm and the cohesive element size is 0.1 mm, as shown in Fig. 5.2.

Boundary conditions

At the beginning of the mixed-mode delamination experiment, the bottom surface of the lower portion of the specimen was fixed and a certain area of the proximal end of the upper delaminated portion was applied displacement loading causing delamination at the media layer (Fig. 5.2b, 5.2d**)**. For the mode I delamination experiment, the proximal end of one of the two initially separated portions of the specimen was fixed and the proximal end of the other separated portion was pulled away causing delamination at the media layer (Fig. 5.2a, 5.2c). The displacement loading rate in the experiments was prescribed as 0.05mm/s.

5.3.2 Identification of material parameters for HGO model

Material parameter values associated with the HGO model for the aortic layer and the CZM for the delamination interface were identified via matching the simulation predictions of the overall load-displacement curve from the loading phase and the delamination phase with experimental measurements of mixed-mode and mode I delamination tests, respectively (Fig. 5.3) (Chen et al., 2013; Leng et al., 2015b).

In this study, the criteria for identifying material parameters associated with the HGO and CZM models is based on the root of mean square error (Leng et al., 2016; Zhou et al., 2015; Zhou et al., 2014) ,

$$f_r = \frac{\sqrt{\frac{\chi^2}{n-q}}}{F_{ref}} < 0.15 \ , \chi^2 = \sum_{i=1}^{n} \left[\left(F_{exp} - F_{sim} \right)_i^2 \right] \tag{5.1}$$

where F_{exp} and F_{sim} are the experimentally measured and numerically predicted force, respectively; F_{ref} is the mean value of force over all data points; n is the total number of data points distributed over the whole delamination cycle that were used for the parameter identification process; q is the number of parameters of the HGO function. A proper set of HGO material parameter values for mixed-mode ($f_r = 0.104$, N=68,$q = 6$) and mode I tests ($f_r = 0.078$, N=71,$q = 6$) are shown in Table 5.1, respectively.

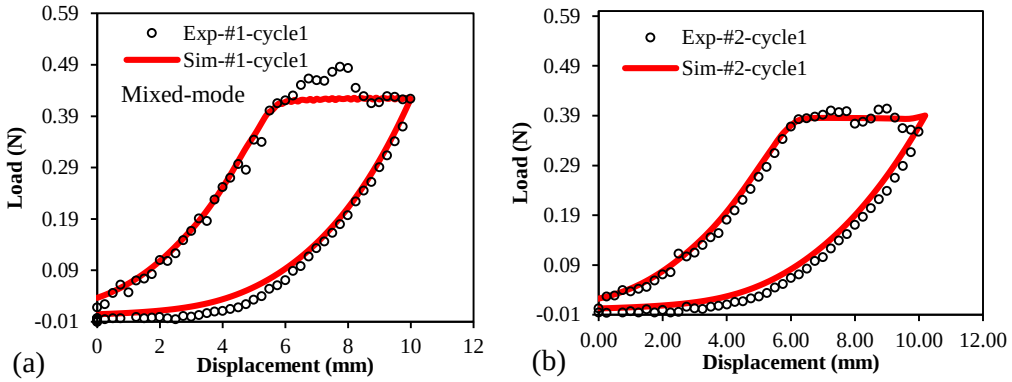


Fig. 5.3 The predicted load-displacement curves of one loading-unloading cycle are compared with the measured curves. (a) mixed-mode delamination; (b) mode I delamination.

Table 5.1 Material parameter values of HGO model

	μ (kPa)	k_1 (kPa)	k_2	κ	r (degree)
Mixed-mode	40[b]	350[b]	0.8[b]	0.226[a]	49[b]
Mode I	40[b]	500[b]	0.8[b]	0.226[a]	45[b]

([a] from reference (Leng et al., 2016); [b] from parameter value identification)

5.3.3 Material parameters associated with the CZM

In the current study, two failure modes, mixed-mode and mode I, were investigated. The values of critical energy release rate of the arterial tissue were quantified from the experiments refer to section 5.2, and the CZM parameters K and λ were chosen from the literature (Leng et al., 2016). A material property identification process described in section 5.3.2 was used to determine the interfacial strength σ_c for the CZM through matching simulation predictions of the delamination phase of the load-displacement curve from cycle 1 with experimental measurements. Those values are shown in Table 5.2 (the same error function in Eq. (5.1) was used).

Table 5.2 CZM parameter values

CZM parameters	G_c (N/mm)	σ_c (MPa)	K ($\mathrm{N/mm^3}$)	λ
Mixed-mode	0.22[d]	0.44[b]	1[e]	1[e]
Mode I	0.186[d]	0.44[b]	1[e]	1[e]

([d] from experimental measurement; [b] from parameter value identification; [e] assumed for simplicity)

5.4 Results

5.4.1 Arterial tissue delamination

The delamination behaviors of the arterial tissue are manifested as the load-displacement relationships, which are characterized by the jagged plateau regions (Fig. 5.4, 5.5). The distances of positions for the start and the end of the delamination phase from point O in one loading-delamination-unloading cycle are represented by a_0 and a_e, respectively. The lengths from the loading point to point O when the delamination front is at a_0 and a_e are represented by l_0 and l_e, respectively (Fig. 5.4a and 5.4b).

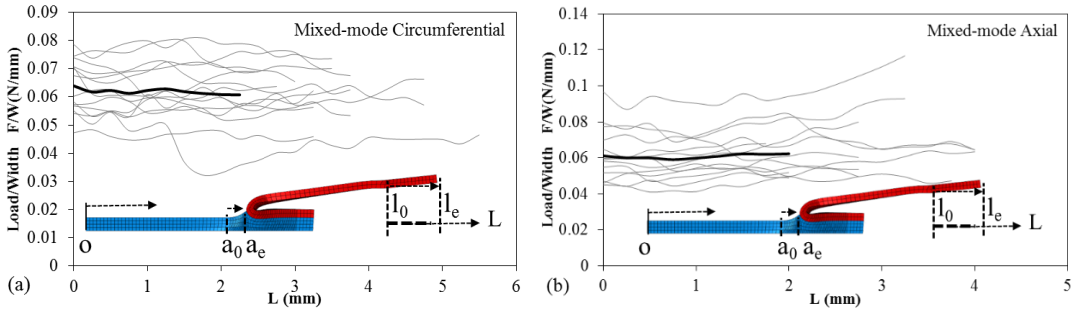


Fig. 5.4 Load/width versus load-point displacement curves for 6 circumferential and 6 axial strip specimens of mixed-mode delamination tests. The thick black curves represent the arithmetic mean values.

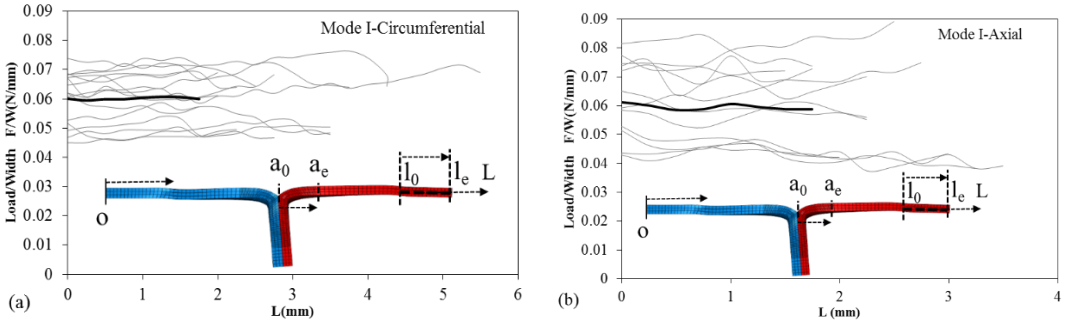


Fig. 5.5 Load/width versus load-point displacement curves for 6 circumferential and 6 axial strip specimens of Mode I delamination tests. The thick black curves represent the arithmetic mean values.

The arithmetic means of load/width vs. load-point displacement curves show no difference for the fracture modes (mixed-mode and mode I) and directions of specimens (circumferential and axial), because the values are all approximately 0.06 N/mm. However, the distributions of the force/width for the axial specimens (0.063 N/mm±0.015 N/mm and 0.058 N/mm±0.014 N/mm for mixed-mode and mode I experiments, respectively) cover a larger range than those for the circumferential specimens (0.061 N/mm±0.01 N/mm and 0.06 N/mm±0.009 N/mm for mixed-mode and mode I experiments, respectively) (Fig. 5.4, 5.5).

The average values of energy release rate with their related standard deviations (mean±S.D.) for circumferential and axial strip specimens under mixed-mode and mode I delamination are shown in Table 5.3.

Table 5.3 The values of energy release rate (G_c) for mixed-mode and mode I delamination of porcine aortic tissue: Mix-C1~Mix-C6, Mix-A1~Mix-A6, MI-C1~MI-C6 and MI-A1~MI-A6 are the specimens of mixed-mode and mode I delamination tests from circumferential and axial directions, respectively.

Circumferential				**Axial**			
Mixed-mode		**Mode I**		**Mixed-mode**		**Mode I**	
Specimen	Gc(N/mm)	Specimen	Gc(N/mm)	Specimen	Gc(N/mm)	Specimen	Gc(N/mm)
Mix-C1	0.215 ± 0.007	MI-C1	0.19 ± 0.023	Mix-A1	0.166 ± 0.043	MI-A1	0.137 ± 0.04
Mix-C2	0.163 ± 0.033	MI-C2	0.179 ± 0.01	Mix-A2	0.329 ± 0.084	MI-A2	0.22 ± 0.014
Mix-C3	0.136 ± 0.022	MI-C3	0.111 ± 0.011	Mix-A3	0.137 ± 0.005	MI-A3	0.301 ± 0.096
Mix-C4	0.133 ± 0.004	MI-C4	0.184 ± 0.016	Mix-A4	0.14 ± 0.015	MI-A4	0.111 ± 0.029
Mix-C5	0.151 ± 0.003	MI-C5	0.123 ± 0.007	Mix-A5	0.227 ± 0.032	MI-A5	0.111 ± 0.008
Mix-C6	0.2 ± 0.01	MI-C6	0.126 ± 0.028	Mix-A6	0.172 ± 0.019	MI-A6	0.104 ± 0.008
Total	0.167 ± 0.036		0.151 ± 0.037		0.19 ± 0.072		0.165 ± 0.083

For circumferential strip specimens, the arithmetic mean of G_c for mixed-mode experiments (0.167±0.036, mean±SD, n=6) is larger than that of mode I experiments (0.151±0.037, mean±SD, n=6); for axial strip specimens, the arithmetic means of G_c for mixed-mode experiments (0.19±0.072, mean±SD, n=6) is also larger than that of mode I experiments (0.165±0.083, mean±SD, n=6). Moreover, the arithmetic means of energy release rate for axial specimens is larger than that for circumferential specimens from both mixed-mode and mode I delamination tests, which is in accord with observations of peeling

tests in the literature (Tong et al., 2011). This phenomenon demonstrates the anisotropic delamination properties of aortic media.

5.4.2 Validation of the CZM method

Validation by prediction of the load-displacement curves

In the previous sections, two finite element models were developed for the mixed-mode (specimen Mix-C1) and Mode I (specimen MI-C2) aortic media delamination experiments, and the parameter values for the HGO model and for the exponential CZM were identified. This section will focus on the prediction of the load vs. load-point displacement curve, because it can be used as a validation of the CZM-based modeling approach for porcine aortic media delamination processes through comparison with experimental measurements of cycle 2 and cycle 3 for mixed-mode and mode I delamination events, respectively.

Simulation predictions of the load-displacement curves for cycle 2 ($G_c = 0.219\ N/mm$) and cycle 3 ($G_c = 0.205\ N/mm$) of mixed-mode delamination are shown in Fig. 5.6a and 5.6b, and those for cycle 2 ($G_c = 0.191\ N/mm$) and cycle 3 ($G_c = 0.161\ N/mm$) of mode I delamination are shown in Fig. 5.6c and 5.6d, respectively. The overall simulation predictions match reasonably well with the experimental data, especially the loading phases of cycle 2 and cycle 3 for mixed-mode delamination.

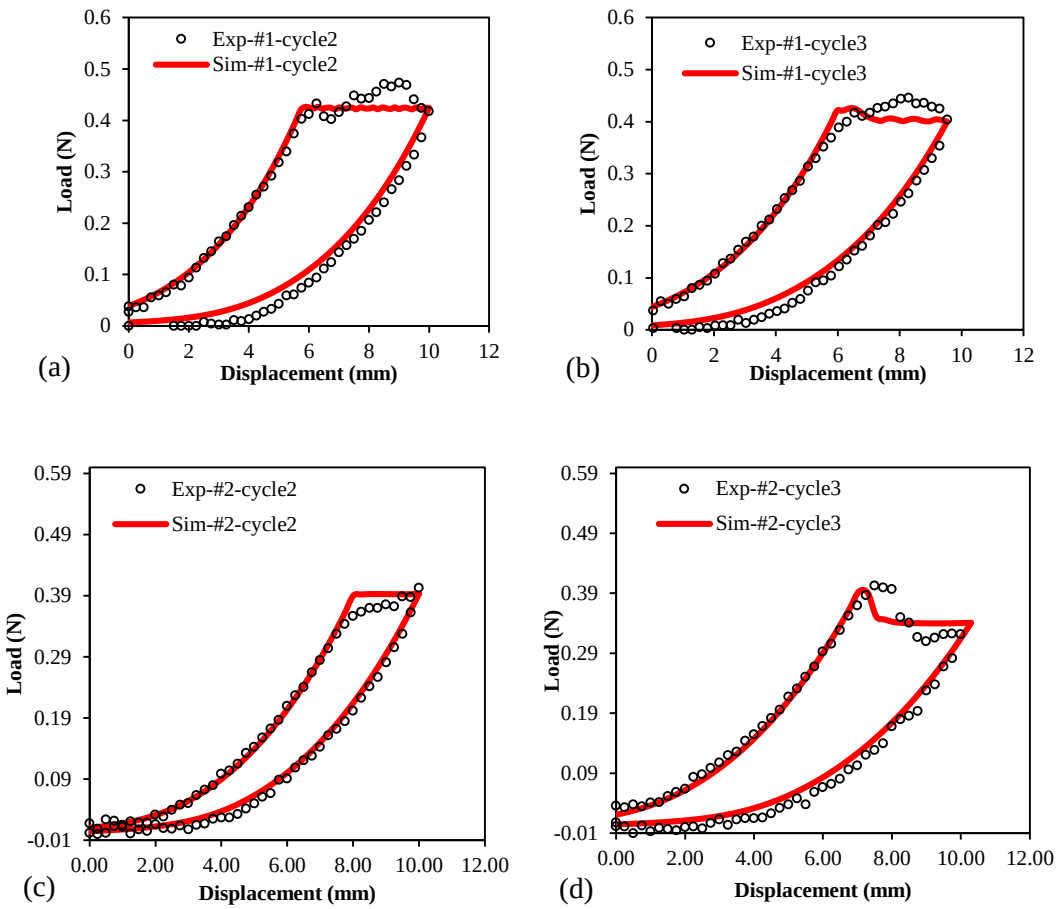


Fig. 5.6 The simulation predicted load-displacement curves of four loading-delamination-unloading cycles are compared with the experimentally measured curves: (a) cycle 2 and (b) cycle 3 of mixed-mode delamination; (c) cycle 2 and (d) cycle 3 of mode I delamination.

Validation through the delamination fronts

In the previous section, the comparison of simulation predictions of the load vs. load-point displacement curves with the experimental measurements was used as a way to validate the CZM-based approach. In the current section, the simulation predictions of delamination fronts for each cycle of mixed-mode and mode I delamination are used for comparison with those from experimental measurements in order to validate the CZM modeling method. For the mouse plaque delamination (Leng et al., 2015b) and human fibrous cap delamination studies (Leng et al., 2016), the delamination fronts were not

recorded during the delamination process. Therefore, it is impossible to compare the delamination fronts predicted by simulation with those from experimental measurements. At steady propagation conditions, the delamination fronts move forward with the separation of two aortic layers. Fig. 5.7 compares the total delamination distances from cycle 1 to cycle 3 with respect to the initial crack front for mixed-mode (Fig. 5.7a) and mode I (Fig. 5.7b), respectively. The distance from one lateral side to the opposite side along the width direction is characterized by W, and the distance from the initial crack front to that of the last time point of the delamination phase of one cycle is represented by *a*. It can be seen that the overall simulation predictions of delamination fronts match reasonably well with the experimental data for each cycle.

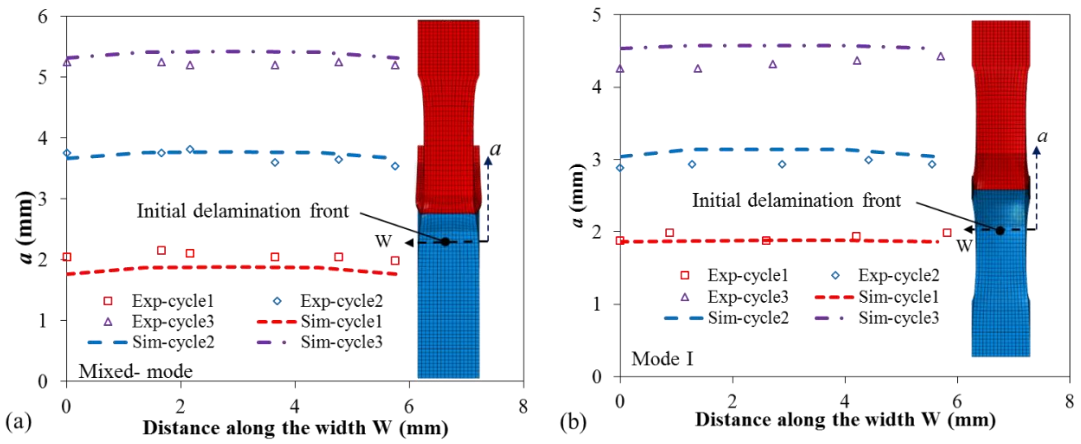


Fig. 5.7 Comparison of predicted and measured delamination front profiles: (a) mixed-mode experiment; (b) mode I experiment.

5.4.3 Ratios of $(\boldsymbol{\delta_{s1}/\delta})^2$ *and* $(\boldsymbol{\delta_n/\delta})^2$

In most cases, mixed-mode delamination tests involve mode I-dominated fracture processes (Wang et al., 2014). However, the delamination of soft tissues reveals a different phenomenon, in that sliding (shearing) displacement has a large effect on the mixed-mode

delamination test. This effect is indicated by a value of 0.8 for the ratio of $(\delta_{s1}/\delta)^2$, which is four times the value of $(\delta_n/\delta)^2$ (Fig. 5.8c and 5.8d). In addition, the ratios of $(\delta_{s1}/\delta)^2$ and $(\delta_n/\delta)^2$ for mode I experiments are 0 and 1, respectively, indicating that tissue damage occurs only by opening separation.

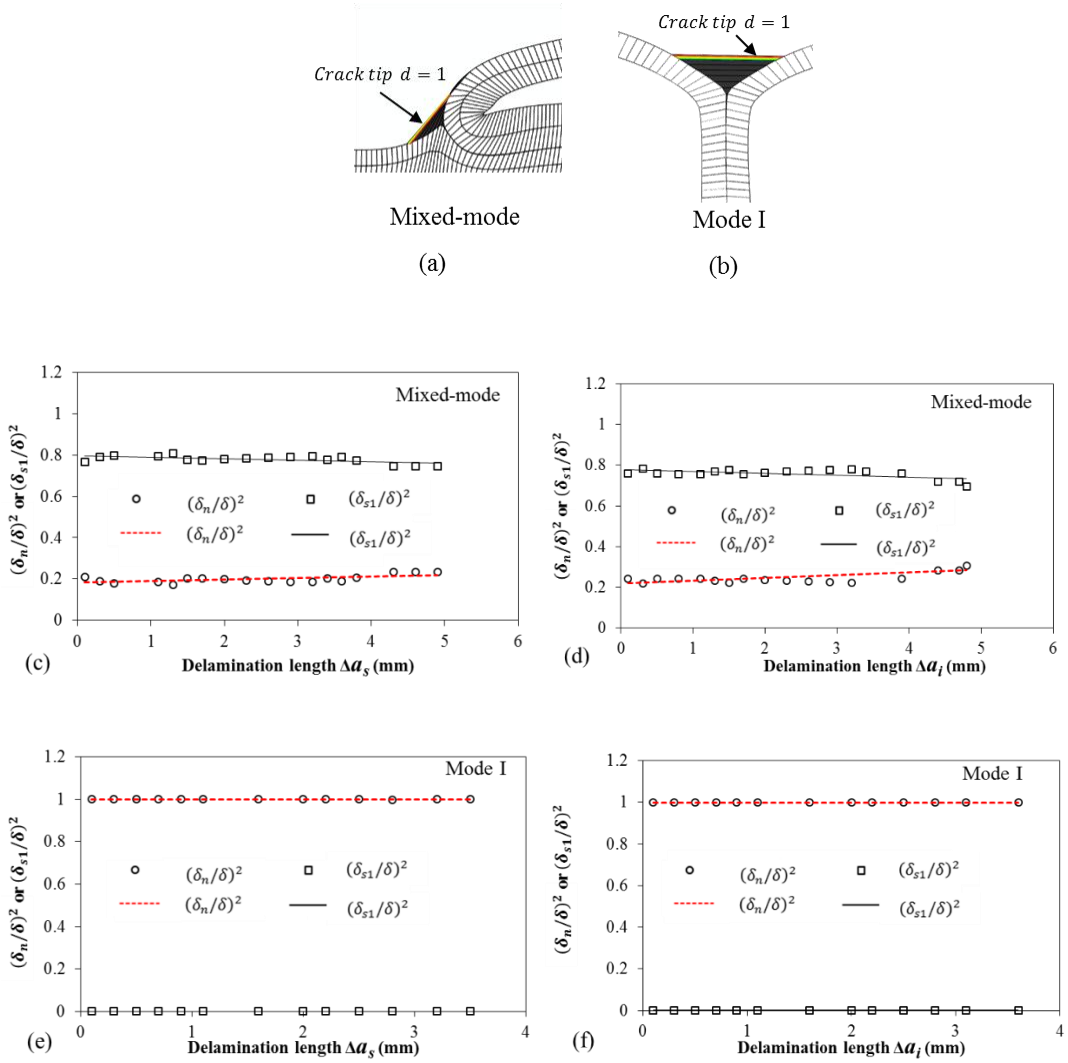


Fig. 5.8 Predicted ratios of $(\delta_n/\delta)^2$ and $(\delta_{s1}/\delta)^2$; figurative depiction of the definition of delamination fronts (damage parameter equals to one) for (a) mixed mode and (b) mode I fracture; ratios of $(\delta_n/\delta)^2$ and $(\delta_{s1}/\delta)^2$ of delamination tests for mixed mode (c) at the outside surface and (d) at the mid-plane as well as for mode I (e) at the outside surface and (f) at the center plane, respectively.

Taking into account the loading angles (Fig. 5.9a) of the mixed-mode delamination, the ratio of $(\delta_n/\delta)^2$ increased with the loading angle, whereas the ratio of $(\delta_{s1}/\delta)^2$ decreased with the loading angle. Moreover, the values of $(\delta_n/\delta)^2$ are larger for the position at the mid-plane than those at the outside surface, but this is reversed for the ratios of $(\delta_{s1}/\delta)^2$ because there is more constraint at the center plane.

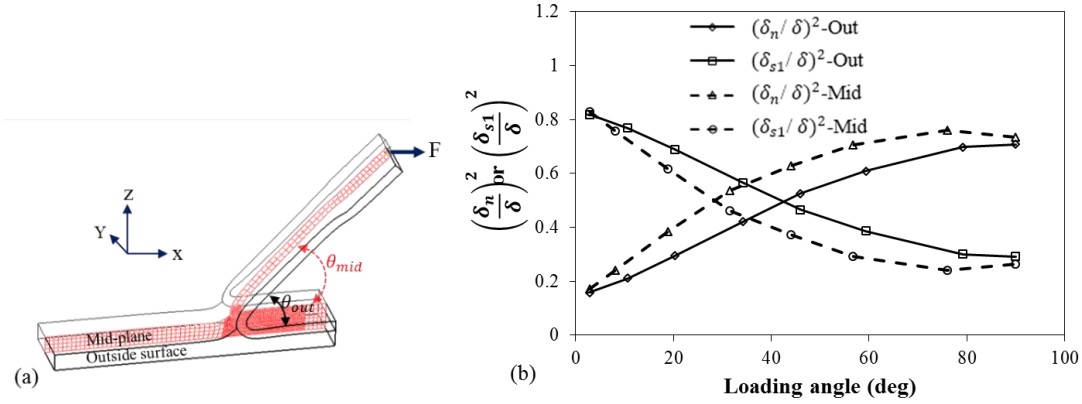


Fig. 5.9 (a) Loading angles at middle plane θ_{mid} and outside surface θ_{out}; (b) predicted ratios of $(\delta_{s1}/\delta)^2$ and $(\delta_n/\delta)^2$ related to loading angles for mixed-mode experiment.

5.5 Discussion

The aim of this study was to quantify the delamination behavior for circumferential and axial strip specimens of porcine aorta using mixed-mode and mode I delamination tests and to develop a mathematical formulation to model the arterial tissue delamination behaviors. The experimental data were processed to calculate the energy release rate that describes the strength of the arterial tissue. A structure-motivated constitutive model (HGO) and a cohesive zone model of the arterial tissue were proposed and verified to allow solving aortic media delamination events.

The aim of this study was to quantify the delamination behavior for circumferential and axial strip specimens of porcine aorta using mixed-mode and mode I delamination tests

and to develop a mathematical formulation to model the arterial tissue delamination behaviors. The experimental data were processed to calculate the energy release rate that describes the strength of the arterial tissue. A structure-motivated constitutive model (HGO) and a cohesive zone model of the arterial tissue were proposed and verified to allow solving aortic media delamination events.

For the aortic media delamination tests, the arithmetic means of load/width ratios are approximately 0.06 N/mm for all the fracture modes and specimen orientations, which are larger than the force/width ratios of human aortic media, 0.023±0.003 N/mm and 0.035±0.002 N/mm, from peeling tests of specimens in the circumferential and axial directions (Li et al., 2013). Numerous biomechanical studies have quantified the critical energy release rate. From published results, the dissection work for the upper descending thoracic porcine aorta is 0.159±0.009 N/mm (Badimon and Vilahur, 2014), and the work/area has a range from 0.019±0.009 N/mm to 0.113±0.004 N/mm for the porcine abdominal aorta (Lawlor et al., 2011). In addition, the dissection energies per area are 0.051±0.006 N/mm and 0.076±0.003 N/mm for circumferential and axial specimens of human aortic media (Li et al., 2013), respectively. The values of the critical energy release rate from the current delamination tests are somewhat larger than the data presented in the literature, but the values are still in the range described above (Badimon and Vilahur, 2014; Lawlor et al., 2011; Li et al., 2013). With the numerical simulation of the delamination response for the subsequent loading-delamination-unloading cycles of the porcine media delamination process, the good quantitative agreement of essential features of the load-displacement curves and distances of delamination front from experimental measurements

provided a validation for the CZM based approach for modeling and simulating aortic media delamination processes.

The ratio of $(\delta_n/\delta)^2$ increased with loading angle, whereas the ratio of $(\delta_{s1}/\delta)^2$ decreased with increasing loading angle. In other words, the delamination process is mode I-dominated failure when the loading angle is approximately 90^0. Meanwhile, the values of $(\delta_n/\delta)^2$ are larger for the position along the mid-plane than those at the outside surface, but this is reversed for the ratios of $(\delta_{s1}/\delta)^2$ because there is more constraint at the center plane.

There are two regions where the predictions have the largest differences from the experimental measurements. One is the unloading phase of mixed-mode delamination (as shown in Fig. 5.6a and 5.6b) when the load is small, and the other is the delamination phase. First, approximation of the geometrical values of thickness and width plays an important role in determining the response of the aortic material with small loading forces. The material properties of the artery wall were identified from cycle 1 for mixed-mode and mode I delamination processes, and the stress strain response may vary with variation of the thickness along the delamination path, causing differences in the loading and unloading phases between simulation predictions and experimental measurements (Leng et al., 2015b). Moreover, the set of material parameter values for the bulk material is a reasonable group of values which may not capture all stages of the behavior of this kind of material. Second, the local composition of the aortic media, especially the fiber bridging along the delamination path, plays an essential role in determining the local energy release rates. The heterogeneous distribution of strong extracellular matrix components (e.g., collagen fibers)

and weaker ECM components (e.g., elastin) is expected to lead to material property variations throughout the specimen, which can largely influence the local mechanical response and hence alter the load-displacement curve. Third, the critical energy release rate data for three cycles of mixed-mode and mode I delamination were averages of the whole delaminated area for each cycle, while in reality the data vary along the delamination path from cycle to cycle revealing oscillation of the values in a certain range, as shown in Table 5.3. Hence, the approximation of the material properties is expected to affect agreement between simulation predictions and experimental measurements of the delamination phase.

Considering validation of the simulations through measurements of the delamination front, no studies have been found focusing on the application of this approach in aortic tissue. In the current work, there is still some difference between the simulation predictions and experimental measurements. First, the delamination fronts from experiments show some difference between simulations especially for cycle 2 and cycle 3, which may due to the fibers bridging that parts of the fibers enduring large deformation without breakage and the delamination front stop moving forward during the experiments (Pal et al., 2014). Moreover, another reason may relate to the strengths of the CZM, σ_c, which were kept the same at 0.44 MPa for cycles with different values of energy release rate. According to Eq. (3.37) and Fig. 3.4, δ_c increases with increasing G_c and decreasing σ_c. Thus, the delamination front (crack front) should vary with different values of σ_c, which needs further study in the future.

The ratios of $(\delta_{s1}/\delta)^2$ and $(\delta_n/\delta)^2$ revealed that mixed-mode delamination tests of aortic tissue involve a shear mode-dominated fracture process when the loading angle is less than 28^o at the middle plane and 41^o at the outside surface of delamination specimens,

respectively. However, the ratios of $(\delta_{s1}/\delta)^2$ and $(\delta_n/\delta)^2$ may vary according to changes in material parameter values of the bulk material model and the interface model (CZM), as well as the geometry of the specimen (width, thickness and length of the upper and bottom layers, respectively), factors which require additional study in the future.

5.6 Conclusions

For both basic science and clinical studies, including disease diagnosis and risk evaluation, it is advantageous to understand the arterial mechanical response during delamination under various loading conditions. The major goals of vascular biomechanics are to determine the appropriate mathematical formulations that describe tissue mechanical properties and interface damage strength, allowing the solution of boundary value problems with predictive power. In this study, the use of an arterial wall structure-motivated constitutive law and a cohesive zone model has enabled the simulation of aortic media delamination behavior based on the critical energy release rate determined from mechanical testing. This integrated theoretical-experimental approach was demonstrated by comparing the loading-delamination-unloading curves and the crack fronts between numerical simulation predictions and experimental measurements for two types of experiments. The delamination simulation facilitates quantification of the delaminated mechanical response of arterial walls and understanding of the pathophysiological mechanical performance, and may shed light on the genesis and progression of certain forms of arterial aneurysms and dissections.

CHAPTER 6

NUMERICAL MODELING OF EXPERIMENTAL HUMAN FIBROUS CAP DELAMINATION

6.1 Introduction

This chapter will focus on the experimental and numerical study of another type of plaque rupture (Fig. 1.1a, red arrow), which is often in the form of fibrous cap separation (delamination) from the underlying tissue (Fig. 1.1d). With the conclusions from chapter 5, the fibrous cap delamination process can be taken as a mode II dominated failure events.

In the current study, the Holzapfel-Gasser-Ogden (HGO) model (Gasser et al., 2006) was initially considered to provide a hyper-elastic constitutive law for the bulk material behavior of all arterial layers (including the fibrous cap and the underlying plaque tissue). The HGO model is commonly employed for arterial walls. It treats each artery layer as a fiber-reinforced material with the fibers symmetrically disposed with respect to the circumferential direction of the artery. However, this model was not able to capture the hysteresis behavior observed in the load-displacement curves obtained from the fibrous cap delamination experiments, because there is no viscoelastic component in the HGO model. To extend the HGO model, a viscoelasticity formulation developed by Holzapfel (Holzapfel, 2000a) was adopted in the current study to incorporate a viscoelastic

component into the HGO model, leading to a viscoelastic anisotropic (VA) model (section 2.5), which is used in the current study.

To capture the material separation (delamination) process along the interface between the fibrous cap and the underlying plaque tissue, the cohesive zone model (CZM) approach is employed in the current study. The CZM approach has been shown to be an effective way of modeling separation failure processes in composite materials, including debonding and delamination across interfaces (Turon et al., 2006).This approach has also been applied in limited cases to the study of material separation failure in arteries (Ferrara and Pandolfi, 2010; Gasser and Holzapfel, 2007; Gasser and Holzapfel, 2006; Leng et al., 2015a; Leng et al., 2015b). In the current study, an exponential traction-separation law (section 3.4) is adopted for the CZM, which utilizes the critical energy release rates obtained directly from the fibrous cap delamination experiments.

Both the VA model and the CZM are implemented in the general-purpose finite element code ABAQUS (ABAQUS, 2013) via user subroutines, which enables the finite element simulations of the fibrous cap delamination experiments. In order to make the simulations possible, one challenge in the current study is the determination of the material parameter values for both the VA model and the CZM model, which are not readily available from the literature. To overcome this difficulty, in the current study a set of parameter values is determined based on limited values suggested in the literature and through matching simulation predictions of the load vs. load-point displacement curve with one set of measurements from the fibrous cap delamination experiments, which involves multiple loading-delamination-unloading cycles (cycle #1, cycle #2, etc.) of the fibrous cap. This set of experimental measurements for determining the material model parameter

values is taken from the load-displacement curve for cycle #1 and from the loading phase of the curve for cycle #2 (see later in Fig. 6.5a). Once the set of parameter values is determined, it is kept intact and used to enable simulations of subsequent loading-delamination-unloading cycles, so that comparisons of the simulation predictions of the load-displacement curves with experimental measurements for the subsequent cycles provide a validation of the parameter values and of the CZM-based finite element modeling and simulation approach for understanding fibrous cap delamination phenomena in arterial failure processes.

6.2 Experimental Details

6.2.1 Human Fibrous cap Delamination Experiments

The current study is focused on numerical modeling and simulation of fibrous cap delamination experiments performed on human carotid artery plaque specimens obtained from endarterectomies. The experiments are similar to the mouse plaque and human media-intima delamination experiments reported in the literature (Wang et al., 2013; Wang et al., 2014; Wang et al., 2011).

Six fresh carotid endarterectomy samples were obtained at the time of surgery from six patients, and one specimen from each sample was successfully prepared, leading to a total of six fibrous cap (FC) delamination experiments. The fresh carotid endarterectomy samples were sliced transversely into segments 5-7 mm in width. Each ring-shaped segment was opened with fine scissors on the side opposite the plaque.

At the start of an experiment, a longitudinal cut was made at one plaque shoulder. At this edge, a scalpel was used to carefully introduce a small initial delamination between the fibrous cap and the underlying plaque tissue. A micro-clamp was used to grip the free

edge of the cap, as shown in Fig. 6.1. The medial face of the carotid artery was glued with DermaBond to a glass plate connected to the load cell of a Bose ELF 3200 test system for load data recording. The delaminated tissue tab on the lateral edge of the fibrous cap was gripped by a pair of micro-clamps connected to the Bose ELF 3200 actuator, which controls the sequential loading-delamination-unloading cycles. For each experiment, a load vs. load-point displacement curve with multiple loading-delamination-unloading cycles was obtained. The delamination process was recorded by a microscopic computer vision system which was placed at a fixed distance above the specimen. After the experiment, the specimen was prepared for histological analysis, which showed that fibrous cap delamination took place between the fibrous cap and the underlying plaque tissue, as shown in Fig. 6.2.

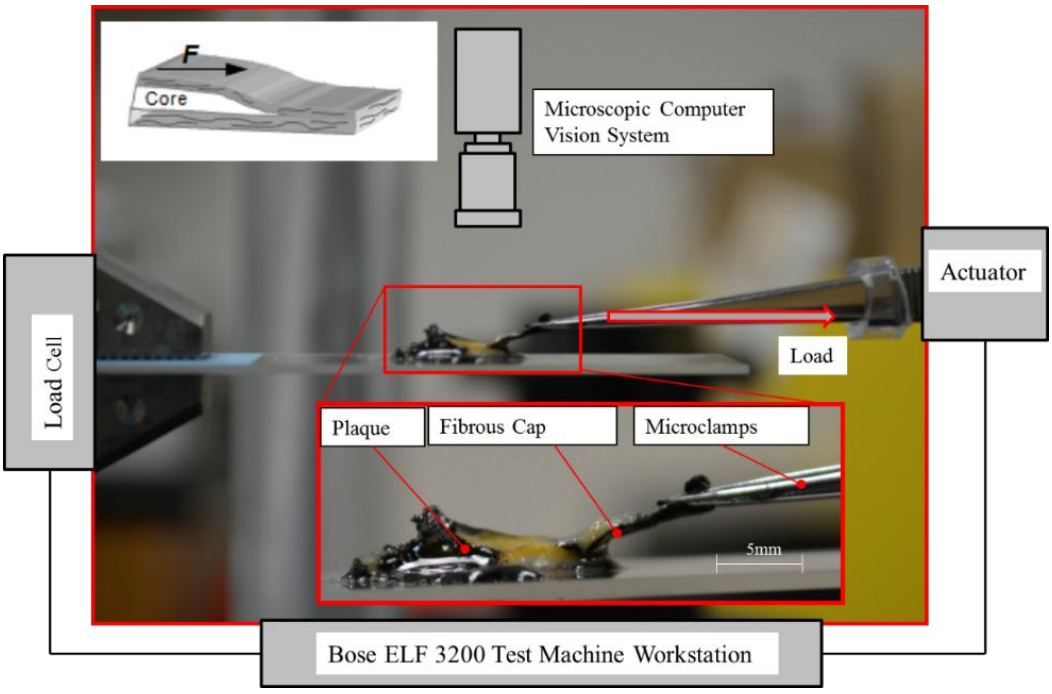
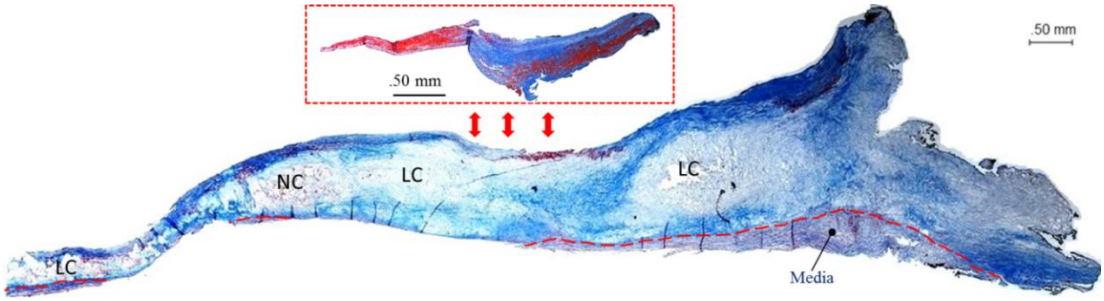
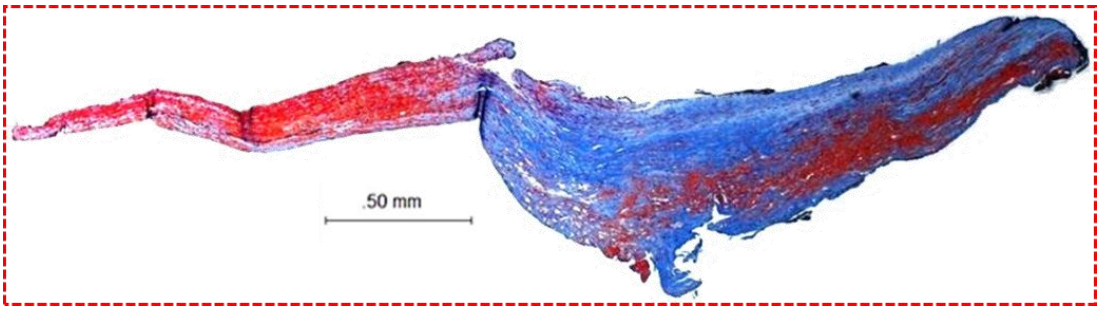


Fig. 6.1 Fibrous cap delamination experiments: experimental setup (scale bar=5 mm).

6.2.2 Histological Images



(a)



(b)

Fig. 6.2 Histological images of the fibrous cap delamination surfaces after Masson's Trichrome staining: (a) a longitudinal section of a completely delaminated specimen, including a partial media and the tissues of atherosclerotic plaque and fibrous cap; (b) a fibrous cap delaminated from the underlying plaque tissue. In these images, the collagen is stained blue, the nuclei are stained purple-black, and the smooth muscle cells (SMCs) are stained red. (Lipid rich core and necrotic core are identified by LC and NC labels, respectively)

Two histological images of paraffin sections of the human fibrous cap delamination specimen stained with Masson's Trichrome are shown in Fig. 6.2. The double-headed arrows show the delamination surface (Fig. 6.2a). It is noted that part of the media layer remained on the glass plate after the fibrous cap was peeled off because of the adhesion of the glue. The boundary of the remaining part of the media in the specimen is marked by red dotted lines, as shown in Fig. 6.2a.

According to Tong et al. (Tong et al., 2011), because the fibrous cap was delaminated along the circumferential direction where the tearing strength is lower than that along the axial direction, the delaminated surface appears smooth when the delamination occurs along the interface between the fibrous cap and the underlying plaque tissue.

6.3 Modeling and Simulation

Although six fibrous cap delamination experiments were performed, at the time of the experiments the focus was on the experimental determination of the critical strain energy release rate, not on the reconstruction of the specimen geometry. As a result, sufficient images of the specimen geometry were taken only for two of the six specimens. These two specimens are labeled samples FC1 and FC2 and are utilized in the modeling and simulation effort.

The geometric models of these two specimens were reconstructed from the images recorded at the start of the experiments. Since the geometry reconstruction procedure is the same for both samples, the specimen geometry model is described in detail below for sample FC1 only.

Further, since the subsequent modeling and simulation procedure is also the same for both samples, it is described in detail below also for sample FC1 only.

6.3.1 Finite Element Model

Through a Boolean operation, the shape of the specimen created according to an image of the side view (as shown in Fig. 6.3a) was merged with the shape created from an image of the top view (as shown in Fig. 6.3b). The delamination area was measured directly from the available experimental images recorded by the microscopic vision system during

a delamination experiment. The area to be delaminated is marked in red in Fig. 6.3c. The resulting three-dimensional (3D) FE model based on the geometric model is shown in Fig. 6.3d (the edge portion (tab) of the initial delaminated fibrous cap away from the delamination front was not included in the FE model because it does not affect the stress state along the delamination front, and its exclusion improves computational efficiency).

It is noted that the geometric model and the subsequent FE model are not perfect due to approximations and uncertainties inherent in the recorded images and from the shape reconstruction process. Thus, approximation errors in the geometric model are expected to affect the accuracy of the FE simulation results and their agreement with experimental measurements. The effect of geometry approximation was studied in an earlier paper on a related topic (Leng et al., 2015b) in which a sensitivity analysis was performed about the effects of geometric approximations on simulation predictions.

The FE mesh is generated using ABAQUS (ABAQUS, 2013). The media and plaque regions are meshed with 6,302 eight-node brick elements, C3D8H, while the cohesive interface is meshed with 255 zero thickness eight-node 3D user-defined elements which are placed along the delamination path starting from the initial delamination front to the end of the fibrous cap. The global size of the element for the media and plaque is 0.5 mm and the cohesive element size is 0.1 mm. The CZM can be implemented for simulating interfacial material separation events with a high computational efficiency when the delamination path is known in advance or pre-defined. In the current study, the delamination path was known from experimental observations and thus was pre-defined at the beginning of simulations.

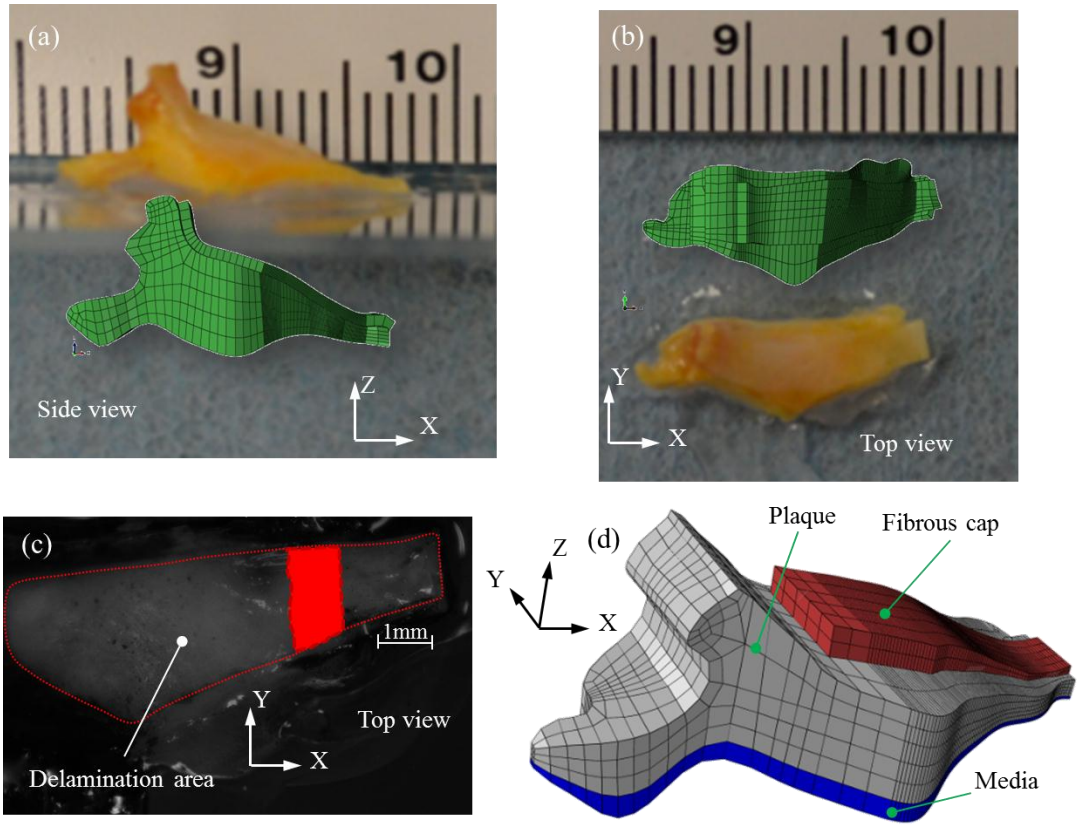


Fig. 6.3 Representative experimental images of the fibrous cap delamination specimen: (a) a front view of the specimen and the finite element (FE) model; (b) a top view of the specimen and the FE model; (c) the delamination area and the area for simulation predictions are marked by red color (the delamination direction is along the X axis); (d) the FE model based on the geometric model reconstructed from the images.

6.3.2 Boundary Conditions

The human carotid artery plaque specimens were obtained from endarterectomies, which contain part of the media layer along with the fibrous cap and the underlying plaque tissue from the carotid artery. At the beginning of an experiment, the bottom media surface of the specimen was glued with DermaBond to a glass plate. Therefore, in the finite element model the boundary condition for the bottom surface of the specimen was taken to be that all nodes on the bottom surface were fixed so that they could not move in any direction.

The delaminated tissue tab on the lateral edge of the fibrous cap was gripped by a pair of microclamps which were translated with a certain displacement parallel to the glass

plate, as shown in Fig. 6.1. Thus, in the finite element model, nodes at the lateral edge of the fibrous cap were given a displacement boundary condition in which the displacement parallel to the glass plate followed the experimentally recorded loading-delamination-unloading cycle values. The displacement loading rate in the experiments was 0.05 mm/s.

Except for the fixed bottom surface and the lateral edge of the fibrous cap where displacement loading was applied, all other surfaces of the finite element model were given a traction-free boundary condition.

6.3.3 Parameter Value Identification

The parameter values for the bulk arterial material models and for the CZM were obtained through a numerical identification procedure (Chen et al., 2013; Leng et al., 2015a) that matches simulation predictions of the overall load vs. load-point displacement curve with experimental measurements. Since the material models used for the simulation involved many parameters and only a limited number of experimental data were available, a fully automated inverse procedure (Chen et al., 2014) was not adopted (hence a manual procedure was used) and not all parameter values were determined from the numerical identification procedure. A subset of the material model parameter values were taken from the literature (or assigned simple values when literature data were not available) and were used as input for the identification procedure. The material model parameter values for the media were taken from the study by Cilla et al. (Cilla et al., 2012) (see Table 6.1); the value for the parameter D in eq. (2.2) was taken to be 10^{-4} (Holzapfel et al., 2002a) (see Table 6.1); and the values for K and λ for the CZM were assigned assumed values (see Table 6.2) that were simple but meaningful.

The experimental load vs. load-point displacement curve for the first loading-delamination-unloading cycle and for the loading phase of the second loading-delamination-unloading cycle (shown in Fig. 6.6a) were used as input data for the identification procedure to determine the remaining material model parameter values. Material model parameter values from the literature (e.g. the material model parameter values for the fibrous cap for human carotid arteries (Balzani et al., 2012; Kiousis et al., 2009) and for the plaque for human carotid arteries (Sommer and Holzapfel, 2012)) were also used as reference values. For CZM parameters, the ultimate tensile stress σ_c was acquired through matching simulation predictions with the experimental measurements using the delamination phase of the load-displacement curve for loading-delamination-unloading cycle #1, and the value for the critical energy release rate G_c was taken to be the mean measured value from the fibrous cap experiments averaged over three loading-delamination-unloading cycles for each delamination group (e.g. cycles 1 to 3 for group 1 and cycles 4 to 6 for group 2).

In the numerical identification process, the HGO and VA material model parameter values and CZM parameter values were considered "acceptable" when the root mean square error (Holzapfel et al., 2005; Zhou et al., 2015; Zhou et al., 2014) satisfies

$$f_r = \frac{\sqrt{\frac{\chi^2}{N-M}}}{F_{avg}} < 0.2 \text{ , with } \chi^2 = \sum_{i=1}^{N} \left[\left(F_{exp} - F_{sim} \right)_i^2 \right] \tag{6.1}$$

where F_{sim} is the reaction force from simulations and F_{exp} is the experimentally measured force; F_{avg} is the sum of all experimentally measured forces for each data point divided by the number of data points; N is the number of data points on the load-displacement curve

that were used in the parameter value identification procedure; and M is the number of parameters whose values were determined from the identification procedure.

A set of HGO and VA material model parameter values is shown in Table 6.1, which were obtained when the root mean square error defined in Eq. (50) was $f_r = 0.152$ with N=183 and $M = 15$.

Table 6.1 HGO and VA material model parameter values

	μ (kPa)	D (kPa^{-1})	k_1 (kPa)	k_2	κ	r (degree)	T_1 (s)	β_1
Media	1.4[a]	1E-4[c]	206.16[a]	58.55[a]	0.29[a]	28.35[a]	5.8[b]	10[b]
Plaque	49.45[b]	1E-4[c]	23.7[b]	2630[b]	0.226[b]	30[b]	2.06[b]	20[b]
Fibrous cap	21.89[b]	1E-4[c]	93.63[b]	7957[b]	0.226[b]	17.22[b]	-	-

([a] from reference (Cilla et al., 2012); [b] from parameter value identification; [c] from reference (Holzapfel et al., 2002a))

Table 6.2 CZM parameter values

CZM parameters	G_c (N/mm)	σ_c (MPa)	K (N/mm^3)	λ
Cycles 1-3 (group 1)	0.23[d]	0.42[b]	10[e]	1[e]
Cycles 4-6 (group 2)	0.294[d]	0.42[b]	10[e]	1[e]

([d] from experimental measurement; [b] from parameter value identification; [e] assumed for simplicity)

A set of CZM parameter values is shown in Table 6.2 (this set is from the same error function in Eq. (6.1)). It is noted that, although simple values for K and λ were assumed, they are relevant and meaningful. The value of 10 N/mm^3 for K is sufficiently large so that artificial compliance from the cohesive interface can be prevented (a different but sufficiently large value will not change the outcome of the simulation). In the absence of experimental data, the value of 1 for the mode mixity parameter λ implies the choice

that Mode I and Mode II components have the same significance in the delamination process.

6.3.4 Three Types of CZMs for the Interface Damage

In order to study the effects to the simulation results from different types of CZM, three types of cohesive zone models are employed, including exponential, triangular and trapezoidal CZMs (material parameter values are kept the same as cycles 1-3 as shown in Table 6.2), which describe the relationship between cohesive traction and separation across a material interface subjected to delamination failure. The detail information about three types of CZM is described in Chapter 3. The simulation results (Fig. 6.4) show that the exponential CZM is a proper model for fibrous cap delamination simulation.

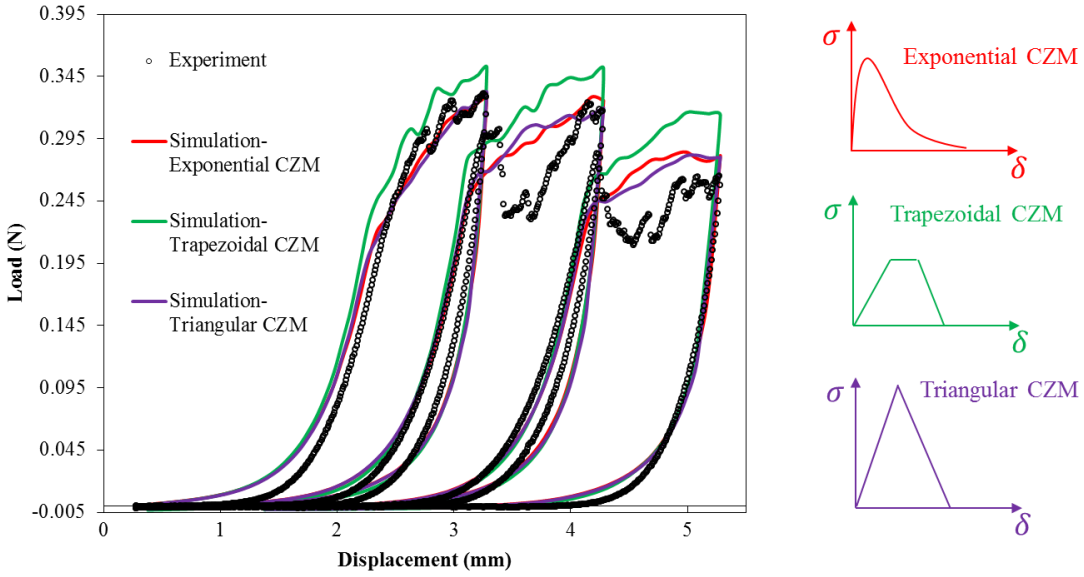


Fig. 6.4 Predicted load-displacement curves of three different cycles using three different types of CZM, with comparison to the experimental curve.

6.3.5 Mesh Convergence analysis

A mesh convergence study was performed in order to ensure that the finite element mesh is sufficiently refined to produce converged solutions. Since mesh generation in this

study was done by controlling the number of divisions along geometric lines, mesh refinements were done by doubling the number of divisions along the lines, which may lead to more or fewer elements than required for strict mesh refinement (in which each brick element is cut into eight elements and each cohesive element is divided into four elements), depending on the complexity of the geometry and the software used for the mesh refinement.

In the current study, Mesh 1 has 6,302 brick (C3D8H) elements and 255 interfacial cohesive elements, and 9,098 nodes. Mesh 2 is refined from mesh 1 so that the element size in mesh 2 is half of that in mesh 1 along x, y and z directions. Mesh 2 has 50,012 brick elements and 1,030 interfacial cohesive elements, and 60,605 nodes. During the mesh refinements, the cohesive element size is dictated by the bulk element size along the delamination path. Specifically, the cohesive element size is 0.1 mm and 0.05 mm, respectively, in the two meshes.

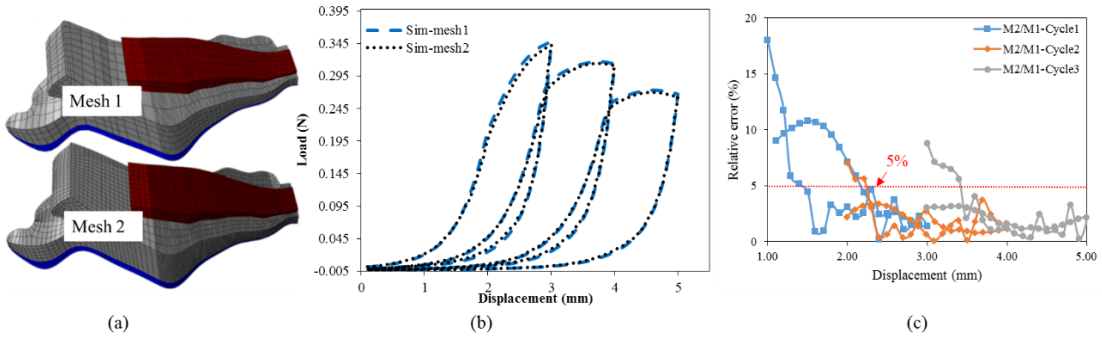


Fig. 6.5 (a) Mesh 1 and Mesh 2 (a refinement of Mesh 1) of the 3D finite element model ; (b) the predicted load-displacement curves for three loading cycles using the two meshes; (c) relative percent error in the reaction load vs. displacement between Mesh 2 and Mesh 1 (M2/M1) for three loading cycles.

We observed that, from Mesh 1 to Mesh 2, there is little change in the predicted load-displacement curves (see Fig. 6.5b). The corresponding variation of the relative error

(the percent difference between the predicted loads from Mesh 1 and Mesh 2) with displacement is shown in Fig. 6.5c. This relative error is greater than 5% only when the predicted reaction load has a small magnitude (below 0.05 N), in which case the large error is mostly due to division by a small value. The average relative percent error for all data points is 3.3%. Overall, Mesh 1 gives well converged predictions, and thus subsequent simulation results are derived from Mesh 1.

6.4 Results

6.4.1 Fibrous Cap Delamination Test Results

Fibrous cap (FC) delamination tests were performed on six specimens. Test results include the load-displacement curves for multiple loading-delamination-unloading cycles for each test, and the critical energy release rate values calculated from these curves.

Test results show that there is a large inter-plaque and inter-sample variability, although the trends in the load-displacement curves are similar. The values of the critical energy release rate G_c (see Table 6.3) acquired from the delamination tests show a mean value of 0.254 N/mm and a large standard deviation of ± 0.15 N/mm.

Typical load-displacement curves from these tests are presented in the next section when simulation predictions are compared with experimental data for samples FC1 and FC2.

Table 6.3 Critical energy release rate values from fibrous cap delamination tests

	Critical energy release rate Gc (N/mm)					
Specimen	FC1	FC2	FC3	FC4	FC5	FC6
Cycles 1-3	0.23	0.24	0.695	0.132	0.217	0.229
Cycles 4-6	0.294	0.199	—	—	—	0.167
Cycles 7-9	—	—	—	—	—	0.133

6.5 Prediction and Validation

In the previous section, a finite element model was developed for the fibrous cap delamination experiments and the parameter values for the bulk material models and for the CZM were identified. In this section, simulation predictions of the mechanical response of the specimen during the experiments are discussed. The focus is placed on the prediction of the load vs. load-point displacement curve since it allows for a direct comparison with experimental measurements, which can serve as a validation of the CZM based modeling/simulation approach for fibrous cap delamination events.

It is worth pointing out that, since the load-displacement curve for the first loading-delamination-unloading cycle and for the loading phase of the second loading-delamination-unloading cycle have been utilized in identifying the material parameter values, they will not be used to validate the simulation predictions. However, comparisons of the predicted and measured load-displacement curves for the first loading-delamination-unloading cycle and for the loading phase of the second loading-delamination-unloading cycle do provide useful information about the level of errors introduced in the geometry of the specimen and in determining the material parameter values, which serves as a good reference for assessing the level of agreement between simulation predictions and experimental measurements for subsequent loading-delamination-unloading cycles.

Simulation results are presented for two fibrous cap samples, FC1 and FC2. For sample FC1, simulation predictions of the load-displacement curve for cycles #1, #2 and #3 are shown in Fig. 6.6a and those for cycles #4, #5 and #6 are shown in Fig. 6.6c. For sample FC2, simulation predictions for sample FC2 for cycles #1, #2 and #3 are shown in Fig. 6.6e.

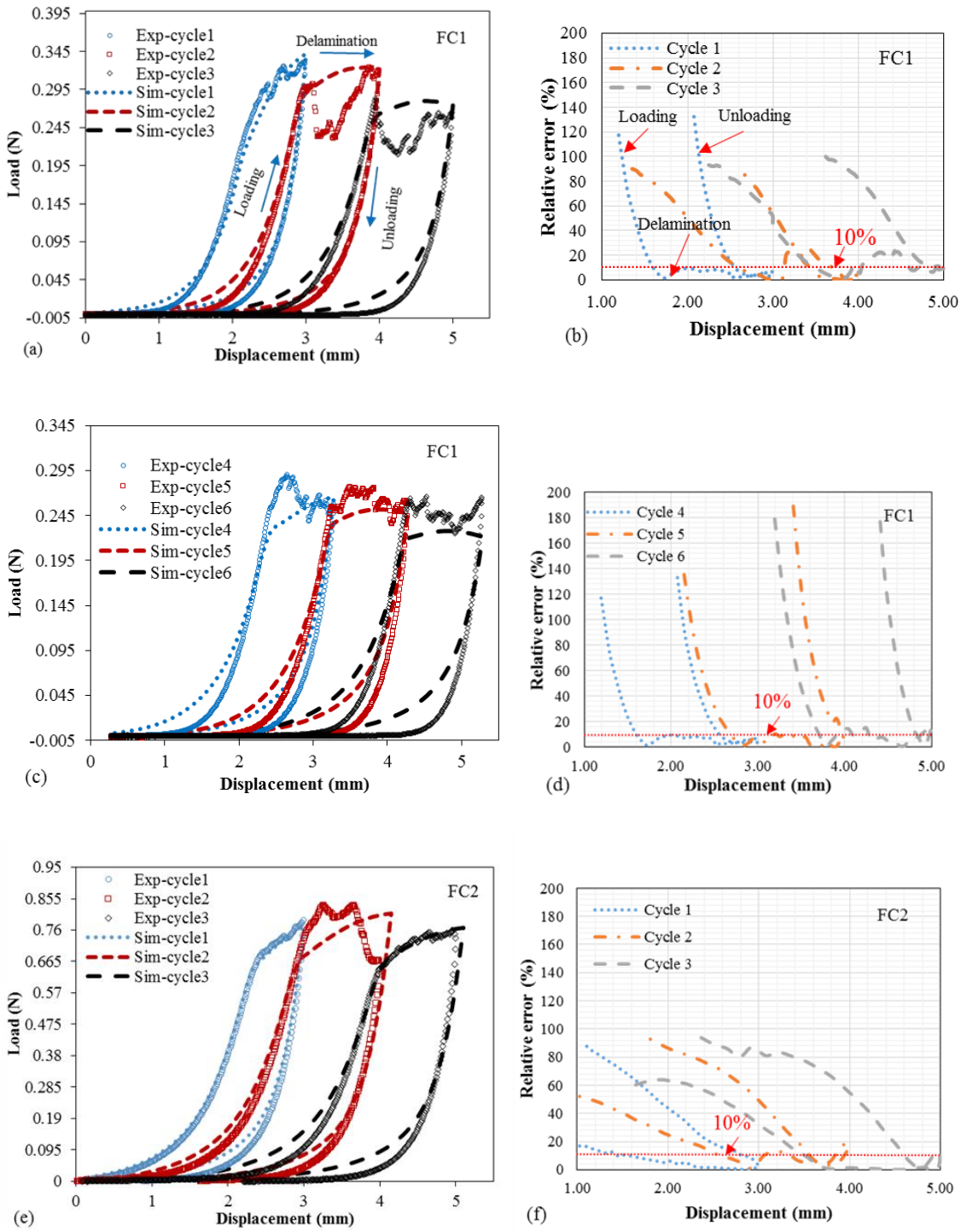


Fig. 6.6 The simulation-predicted load-displacement curves of nine loading-delamination-unloading cycles are compared with the measured curves: (a) the load-displacement curves and (b) relative error vs. displacement curves for cycles #1, #2 and #3 for sample FC1; (c) load-displacement curves and (d) relative error vs. displacement curves for cycles #4, #5 and #6 for sample FC1; (e) the load-displacement curves and (f) relative error vs. displacement curves of cycles #1, #2 and #3 for sample FC2.

It is noted that, due to inter-sample variability (the test results and model parameter values are patient-specific), the material parameter values for sample FC1 cannot be transferred to sample FC2. As such, key material parameter values for sample FC2 are determined from the test results of FC2 according to the same procedure as the one used for FC1. The parameter values for FC2 that are different from those for FC1 are: $r = 58.35°$ (media), $\mu = 11.45$ kPa (plaque), $r = 60°$ (plaque), $T_1 = 9.06\, s$ (plaque), $\mu = 11.89$ kPa (fibrous cap), and $G_c = 0.24\, N/mm$ (CZM). All remaining parameter values for FC2 are taken to be the same as those for FC1.

The relative error vs. displacement curves for the comparisons of simulation predictions with experimental measurements are shown in Figs. 6.6b, 6.6d and 6.6f. Relative percent errors for the loading and unloading phases are large (above 10%) when the magnitude of the load is small (0.145 N for FC1 and 0.285 N for FC2). Factors that may contribute to these large errors are discussed in Section 6.6. However, relative errors for the rest of the loading and unloading curves as well as for the delamination phases are below 10%. It can be seen that overall the simulation predictions match well with the experimental data. The unloading phase of cycle#1 and the loading phase of cycle #2 from FC1, which describe the first hysteresis loop between cycles #1 and #2, show good match between predictions and measurements. The agreement between predictions and measurements for the subsequent hysteresis loops is similar to that for the first loop.

The von Mises stress contours in the specimen when the loading was at three typical points during the 3rd loading-delamination-unloading cycle are shown in Fig. 6.7. The values of stress contours in the area near the delamination front shown in the zoomed-in views in Figs. 6.7(a), (b) and (c) are correlated with the loading levels in the load-

displacement curve. Taking the loading level for Fig. 6.7(b) as an example, the highest stress is located behind the delamination front in the delaminated cap, which is consistent with the corresponding effective traction level as shown in Fig. 6.7d, where the maximum effective traction $t = 0.42$ MPa occurs behind the delamination front.

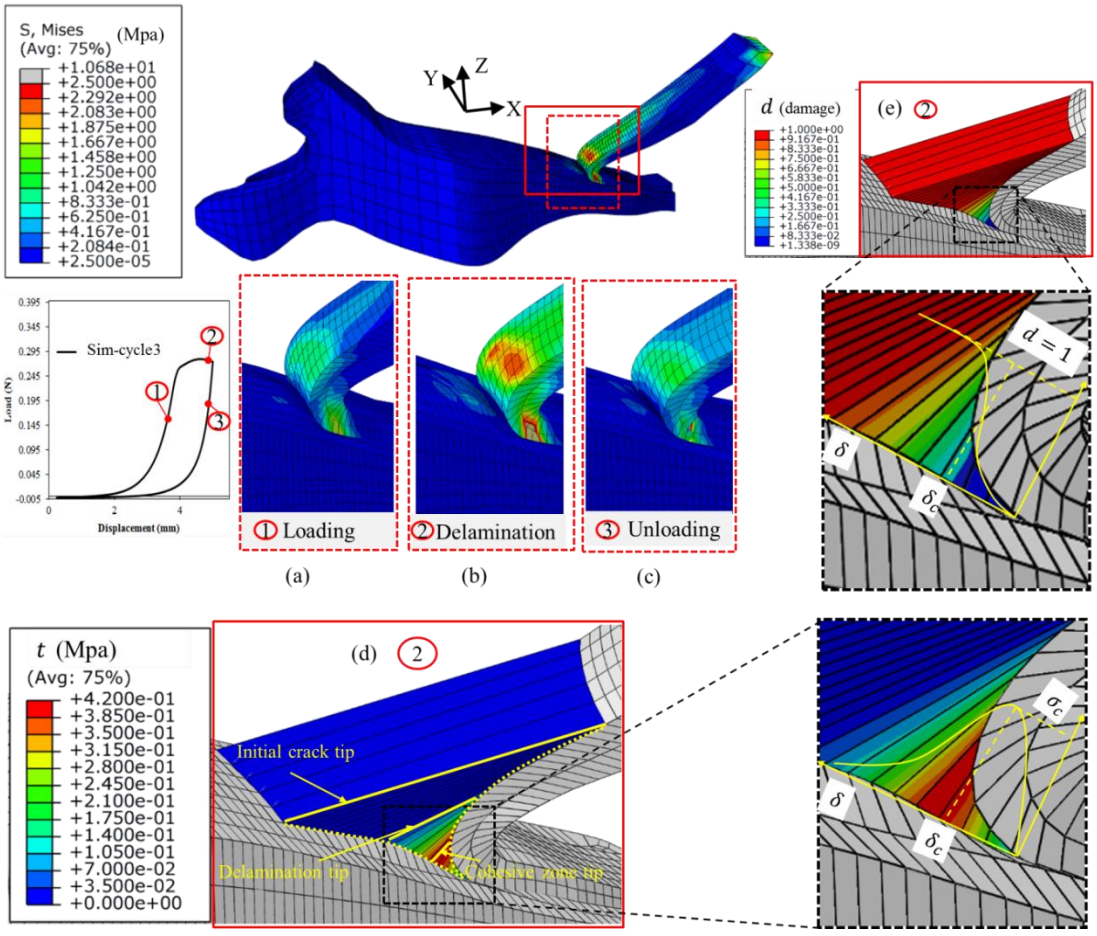


Fig. 6.7 von Mises stress contours at three typical points during loading-delamination-unloading cycle #3: (a) at point 1 in the loading phase; (b) at point 2 in the delamination phase; (c) at point 3 in the unloading phase; (d) the effective traction contours in the cohesive elements at point 2; (e) the cohesive damage parameter contours in the cohesive elements at point 2.

It can be seen from Fig. 6.7d that the interfacial cohesive elements are stretched and the effective traction contours in the cohesive elements enclosed by the black dotted line reveal the stiffening and softening portions of the interfacial separation process during

delamination propagation, as shown more clearly in the zoomed-in view of the insert. In Fig. 6.7d, the initial crack tip represents the delamination front at the beginning of cycle #1, the delamination tip indicates the delamination front at the end of the delamination phase of cycle #3 (a point where the cohesive traction is zero and the cohesive damage parameter $d = 1$), and the cohesive zone tip shows the point where the traction equals the maximum value ($t = 0.42$ MPa). The cohesive elements are completely separated when the damage parameter $d = 1$ (as shown in Fig. 6.7e) and also the effective traction t is approximately equal to zero (as shown in Fig. 6.7d). The traction-separation curve and the damage-separation curve are shown in the zoomed-in views in the inserts of Figs. 6.7d and Fig. 6.7e, respectively.

6.6 Discussion

There are two regions where the predictions have the largest differences from the measurements. One is when the load is small, and the other is during the delamination phase. The differences between the simulation predictions and experimental results may be due to several simplifications, approximations and uncertainties.

First, there are the approximations for the geometries of the delamination path and the specimen surfaces. The geometry of the diseased artery specimen is complex and many of the small features (e.g. the depressions on the uneven delaminated surface) were not modeled. The shape of the fibrous cap is not regular and has a zigzag boundary along the circumferential direction.

Second, the local components of the atherosclerotic plaque (e.g. the lipid core and calcified tissue) were assigned the same material properties due to the lack of sufficient experimental data. The lipid core and the calcified tissues are distributed randomly in the

plaque with different volumes (as shown in Fig. 6.2). The heterogeneous distribution of strong materials (e.g., calcified tissue and collagen fibers) and weak materials (e.g., lipid core) is expected to lead to material property variations throughout the specimen, which can largely influence the local mechanical response and hence alter the load-displacement curve.

Third, to reduce experimental data noise, the critical energy release rate data for cycles #1, #2 and #3 were averaged and the resulting mean value was set to be the input value for the critical energy release rate in the simulations for cycles #1, #2 and #3. The same was done for cycles #4, #5 and #6. In reality, the critical energy release rate is observed experimentally to vary along the delamination path and from cycle to cycle, and the measured values oscillate in a certain range (Tong et al., 2011; Wang et al., 2014). This gross approximation is expected to affect agreement between predicted and measured load-displacement curve during the delamination phase of a loading cycle.

Fourth, the material parameter values used for the HGO and VA models may not be the best values to describe the complex bulk mechanical response. There were many unknown parameter values involved and the available experimental data were limited, and compromises were made in the numerical identification procedure for determining the parameter values. As a result, the parameter values determined through the identification process mentioned in section 6.3.3 may not be the only choice or the best choice for the specimen.

Furthermore, the differences between predictions and measurements seen in the first hysteresis loop of the load-displacement curve, which was used for parameter value identification, suggest that features not captured in the current study (e.g. local material

variations due to heterogeneous tissue distribution) may be an important factor that affects the accuracy of the results when the viscoelastic material model is implemented.

Considering the various simplifications, approximations and uncertainties involved in the simulations, which are unavoidable in this study due to the lack of available data, it can be said that the simulation predictions can capture, both qualitatively and quantitatively, the main features of the load-displacement curve, and that the overall good agreement between predictions and measurements provides a meaningful validation of the CZM based modeling and simulation approach for fibrous cap delamination events.

6.7 Conclusions

In the current study a cohesive zone model-based computational approach for modeling and simulating fibrous cap delamination events was developed and applied successfully to fibrous cap delamination experiments performed on human carotid artery endarterectomy specimens. A 3D finite element model was built based on a 3D specimen geometry reconstructed from recorded images of the specimen.

The bulk material behavior of the arterial layers (including the fibrous cap and the underlying plaque tissue) was represented by the HGO anisotropic hyperelastic constitutive model and a viscoelastic extension of the model proposed in the current study that allows for capture of the hysteresis behavior exhibited in the load-displacement curve over loading-delamination-unloading cycles. The behavior of the interface between the fibrous cap and the underlying plaque was characterized by an exponential cohesive zone model, which governs the traction-separation relationship and the interfacial failure process.

A numerical procedure for identifying material model parameter values was developed, in which measured load and load-point displacement data for the first loading-

delamination-unloading cycle and for the loading phase of the second loading-delamination-unloading cycle were used as input to an inverse analysis. The identified parameter values were then applied in the simulations to predict the load-displacement response for the subsequent loading-delamination-unloading cycles of the fibrous cap delamination experiments.

Comparisons of simulation predictions of the load-displacement curve with experimental measurements reveal that the simulation predictions were able to capture the essential features of the load-displacement curve from the fibrous cap delamination experiments and show reasonably good quantitative agreement with experimental measurements. The results of this study provide a validation for the proposed CZM based approach for modeling and simulating fibrous cap delamination events.

CHAPTER 7

AN INVERSE ANALYSIS OF COHESIVE ZONE MODEL PARAMETER VALUES FOR HUMAN FIBROUS CAP MODE I TEARING SIMULATIONS

7.1 Introduction

Previous studies have evaluated the mechanical and/or failure behavior of human fibrous cap or plaque. Ultimate tensile stress and ultimate tensile strain were acquired through uniaxial tensile tests on human carotid plaques which contain lipid cores, intraplaque hemorrhage and a thin fibrous cap (Lawlor et al., 2011). Indentation tests on human fibrous cap samples were carried out in order to obtain the shear modulus of a neo-Hookean model (Barrett et al., 2009). Several groups have obtained the circumferential tensile stress and associated strain of human fibrous caps through uniaxial tensile tests (Cheng, 1993; Holzapfel et al., 2004b; Lendon et al., 1991; Loree et al., 1994). Previous work used ultimate tensile stress and strain as the material parameters to evaluate fibrous cap tissue failure (Loree et al., 1992), but those parameters cannot be used to describe the damage initiation and propagation processes. Thus, the cohesive zone parameters such as interfacial strength and critical energy release rate can be implemented as input data in a finite element model to simulate and predict the entire fibrous cap failure process.

The critical energy release rate can be obtained from plaque delamination (Wang et al., 2013) and fibrous cap delamination (Leng et al., 2015a) tests with the delaminated

areas acquired directly from the experiments. However, this method cannot be used directly to acquire the cohesive strength of the fibrous cap across its thickness due to limited data on tearing area from miniature single notch edge tearing (MSENT) experiments. Thus, an automated inverse modeling approach including finite element analysis provides a way to gain the interfacial strength and critical energy release rate from the fibrous cap tearing tests.

Some automated methods have been used to obtain the material parameter values of arterial tissue under different types of mechanical tests. In one such approach, an experimental curve fitting method with simulations from FEA software ABAQUS and fitting tool from Matlab was implemented to acquire the shear modulus of human fibrous cap under indentation tests (Barrett et al., 2009) and material parameters of an anisotropic constitutive model for mitral valve anterior leaflets (Lee et al., 2014). In other studies, an inverse optimization protocol based on the Nelder-Mead Simplex method and FEA was conducted to estimate in vivo material parameters for a human aorta (Zeinali-Davarani et al., 2011). In other work, the material parameters of human carotid arteries were determined by means of a Levenberg-Maquardt algorithm in Matlab (Li et al., 2013; Prim et al., 2016; Sommer and Holzapfel, 2012; Zhou et al., 2015; Zhou et al., 2014).

However, little information is available regarding the interfacial strength and critical energy release rate of crack propagation during tearing of the fibrous cap. To this end, mode I tearing tests on circumferentially oriented human fibrous cap specimens have been carried out in order to obtain the cohesive strength across the thickness using an inverse analysis method. A finite element analysis of the tearing procedure is proposed to gain deeper understanding of the fibrous cap tearing phenomenon. Furthermore, these

studies will provide a perspective for using finite element methods to predict atherosclerotic plaque rupture, and a solid basis for medical advances in intervention and prevention of this life-threatening event.

7.2 Materials and Methods

7.2.1 Experimental Procedure

In this study, fibrous cap tearing experiments are performed on human carotid atherosclerotic plaques obtained from endarterectomies. Five fresh carotid endarterectomy samples were obtained at the time of surgery from five patients. One fibrous cap sample was successfully prepared from each specimen, leading to five fibrous cap tearing (FCT) tests. The plaque specimens were slice transversely and opened longitudinally before isolation of the fibrous cap, yielding circumferentially-oriented tissue strips.

Before the tearing test, samples were preconditioned by approximately 5 cycles of quasi-static uniaxial tensile tests at a loading rate of 0.05 mm/s in order to obtain a repeatable mechanical response (Zhou et al., 2016). The tensile loading experimental data were used to obtain the bulk material properties of each fibrous cap. Then, a surgical scalpel was used to carefully introduce an initial cut perpendicular to the direction of the loading (to initiate the tearing path) at the midline of the specimen (Fig. 7.1a, 7.1c). The lower edge of the tissue strip was gripped by clamps connected to the load cell of a Bose ELF 3200 test system for load data recording, and the top edge (proximal end) of the fibrous cap was gripped by clamps connected to the Bose ELF 3200 actuator, which controlled the applied loading.

The tearing test was performed by moving the proximal end of the fibrous cap and the prescribed displacement and load were recorded via system actuator and load cell. The tearing process was recorded by a computer vision system with two cameras perpendicularly positioned in order to get the front and side views of the specimen.

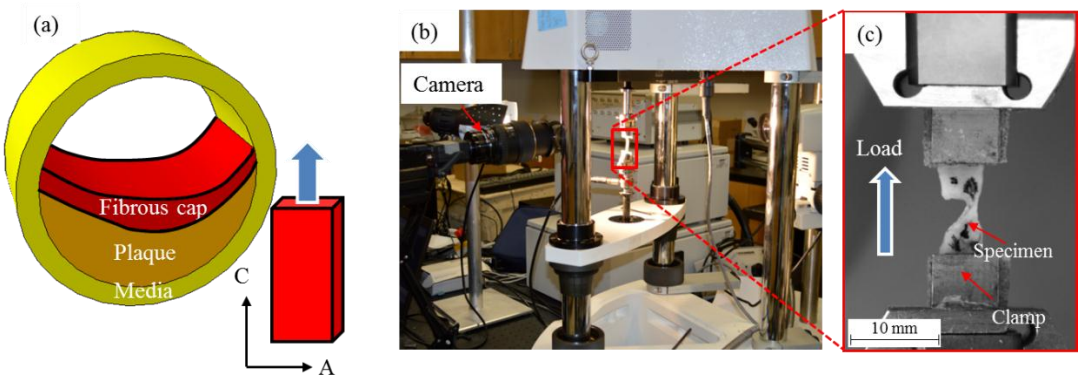


Fig. 7.1 Schematic of experimental setup. (a) Schematic of carotid artery plaque specimens obtained from endarterectomies and cut to strips transversely (A: axial direction; C: circumferential direction); (b) Experimental setup of fibrous cap tearing tests; (c) experiment setup (zoomed-in view).

7.3 Numerical Implementation

The simulations of fibrous cap tearing process are implemented through the finite element software ABAQUS 6.13 (ABAQUS, 2013). The material parameter values of the bulk material model of fibrous cap were obtained from the inverse analysis of the uniaxial tensile tests of fibrous cap before the tearing tests. These material parameter values were used as the input data for the bulk material model of the fibrous cap in the simulations of tearing experiments. Finally, cohesive parameters including interfacial strength and critical energy release rate were acquired through the inverse analysis of the fibrous cap tearing

tests using CZM-based approach by comparing the numerical predictions of load-displacement curves with the experimental measurements.

7.3.1 Geometrical Modeling

The geometric models were reconstructed from the images obtained during the fibrous cap tearing experiments (Fig. 7.1). The tearing path of the fibrous cap specimens were measured directly from the experimental images taken at different stages during the testing. Specimen #1 (FCT1) with the fibrous cap teared into two separated parts, was used as a representative illustration of obtaining the cohesive parameter values of the fibrous cap by using inverse analysis method. A straight tearing path was pre-defined along the width of the specimen at the beginning of the simulations, as shown in Fig. 7.2c.

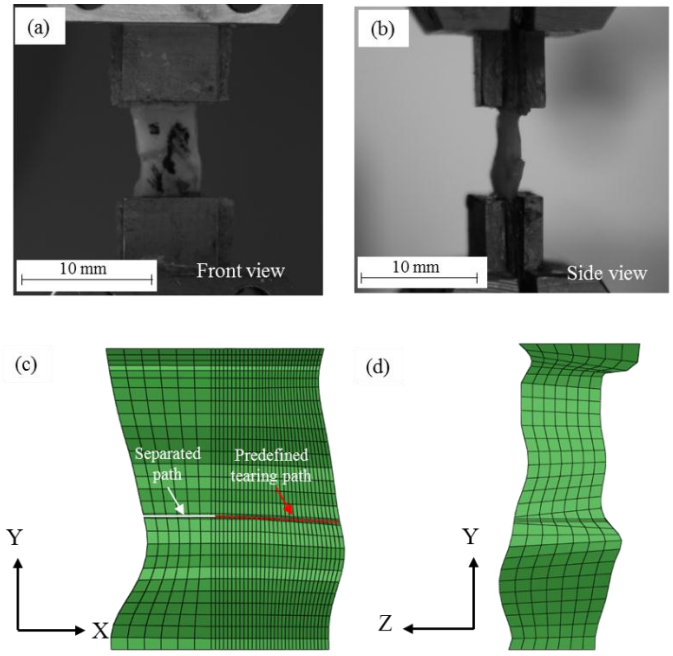


Fig. 7.2 Representative experimental images of the fibrous cap tearing specimen: (a) a front view of the specimen; (b) a side view of the specimen; (c) FE model of front view of the specimen, which the white line shows the initial separated path and the red dot line represents the predefined tearing path that will be teared during the experiment; (d) FE model of side view of the specimen.

7.3.2 Meshing

The fibrous cap are meshed with eight-node brick elements (C3D8H), while the cohesive interface (tearing path) is meshed with zero thickness eight-node 3D user-defined elements which placed along the tearing path starting from the initial tearing front to the end of the sample along the width. The front and side views of meshed geometric model of FCT1 are shown in Fig. 7.2c and 7.2d, respectively, with 0.4mm for the global size of the elements of fibrous cap and 0.1 mm for elements of the cohesive interface.

7.3.3 Boundary Conditions

At the beginning of the experiment, the lower edge was fixed by clamps. Therefore, in the finite element model the boundary condition for the lower edge was taken to be that all nodes on the low edge were fixed so that they could not move in any direction. The top edge was fixed by clamps which were translated with a certain displacement upward with loading rate 0.05 mm/s, as shown in Fig. 7.1c. Except for the fixed part of the two edges, all the other surfaces of the finite element model were set to a traction-free boundary condition.

7.3.4 Identification of Model Parameter Values for HGO Model

Material parameter values of HGO model were obtained through inverse analysis of the uniaxial tensile tests of fibrous cap that fitting simulation predictions of the load vs. load-point displacement curve with experimental measurements (Fig. 7.3). A set of HGO parameter values of fibrous cap from the reference (Leng et al., 2016) was used as the initial input values, then a fully automated inverse procedure (Chen et al., 2014) presented in ***Appendix C*** was adopted and all parameter values were determined when the objective

function $F_{p_i}(\mu, k_1, k_2, r, \kappa,)$ is minimized to an acceptable value during the numerical identification procedure.

7.3.5 CZM Parameters along the Tearing Path

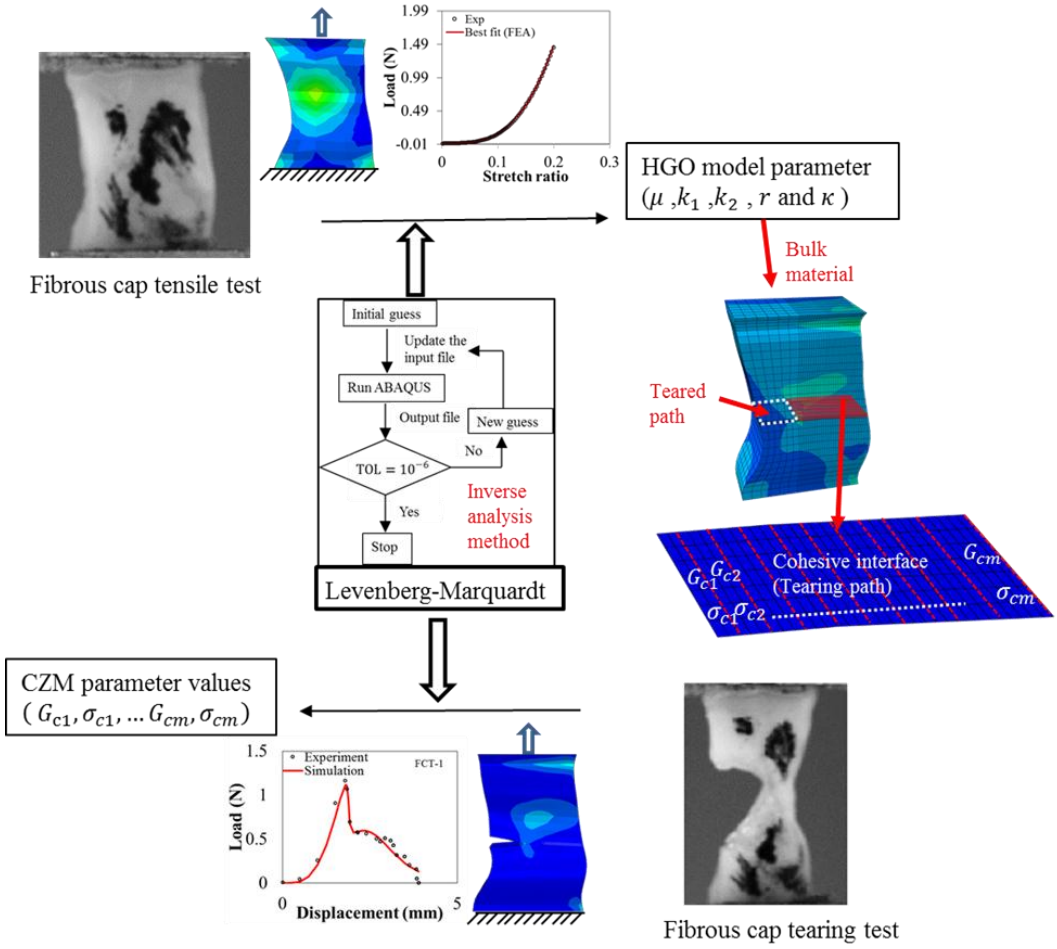


Fig. 7.3 Flow chart of the inverse analysis of fibrous cap tearing tests which used to obtain the cohesive interface parameter values along the tearing path.

The HGO model parameter values obtained from the material parameter identification procedure in the previous section were used as the material parameter values of bulk material. A set of exponential CZM parameter values obtained from the reference (Leng et al., 2016) was used as the initial guess of CZM parameter values for the cohesive

interface. For simplification, the value of K and λ were set equal to 10 N/mm^3 and 1 (Leng et al., 2016), separately. The initial guess of the critical energy release rate and interfacial strength for the total tearing path are 0.23 N/mm (Leng et al., 2016) and 0.2 MPa (assumed value), respectively. For the entire tearing path, only the values of critical energy release rate and cohesive interfacial strength varied during the inverse analysis processes and a proper set of parameter values was determined when the objective function $f(G_{c1}, \sigma_{c1}, \ldots G_{cm}, \sigma_{cm})$ is minimized to an acceptable value. The whole inverse modeling processes of fibrous cap mode I tearing tests are shown in Fig. 7.3.

7.4 Results

7.4.1 Inverse Analyses of Uniaxial Tensile Tests of Fibrous cap

In the numerical identification process, the HGO model parameter values of human fibrous cap were obtained when the objective function satisfies an acceptable value, which are shown in Table 7.1.

Table 7.1 The parameter values of the HGO model for human fibrous cap samples under uniaxial tensile tests obtained from inverse analysis process.

Sample	μ (kPa)	k_1 (kPa)	k_2	r (angle)	κ	Residual f
FCT1	2.00	4705.30	54.26	57.01	0.27	0.0006642
FCT2	2.00	413.9	37.96	66.69	0.27	0.0000013
FCT3	5.1	938.80	20.09	38.53	0.23	0.0000225
FCT4	4.00	388.9	16.26	65.87	0.25	0.0000258
FCT5	4.40	3263	77.83	73.56	0.29	0.0000056

7.4.2 Inverse Analyses of Fibrous Cap Tearing Experiments

In the previous section, a finite element model was developed for the fibrous cap uniaxial tensile experiment and the parameter values for the bulk models were identified. In this section, the HGO model parameter values was used for the bulk material model of

the fibrous cap in order to obtained the cohesive interface parameter values along the tearing path (Fig. 7.3). The values of critical energy release rate and CZ interfacial strength of fibrous cap are shown in Table 7.2 (f represents the residual). The comparison of simulation predictions between experimental measurements of the load-displacement curve of the fibrous cap tearing tests are shown in Fig. 7.4.

Table 7.2 The values of critical energy release rate and interfacial strength of fibrous cap tissue obtained from inverse analysis process.

	FCT-1		FCT-2		FCT-3		FCT-4		FCT-5	
Area	G_c (N/mm)	σ_c (Mpa)	G_c (N/mm)	σ_c (Mpa)	G_c (N/mm)	σ_c (Mpa)	G_c (N/mm)	σ_c (Mpa)	G_c (N/mm)	σ_c (Mpa)
1	0.237	0.368	1.341	0.572	0.089	0.029	0.797	0.289	0.172	0.026
2	0.225	0.387	1.346	0.483	0.090	0.042	0.786	0.339	0.095	0.001
3	0.203	0.378	1.391	0.492	0.110	0.051	0.779	0.518	0.213	0.096
4	0.195	0.378	1.428	0.506	0.123	0.067	0.777	0.558	0.289	0.197
5	0.434	0.211	1.313	0.494	0.085	0.093	0.778	0.564	0.182	0.354
6	0.411	0.195	1.235	0.474	0.125	0.120	0.778	0.543	0.257	0.392
7	0.411	0.195	1.224	0.500	-	-	-	-	0.224	0.386
8	0.413	0.198	-	-	-	-	-	-	-	-
9	0.341	0.159	-	-	-	-	-	-	-	-
10	0.188	0.082	-	-	-	-	-	-	-	-
Mean	0.306	0.255	1.326	0.503	0.096	0.057	0.782	0.468	0.205	0.207
SD	0.105	0.112	0.075	0.032	0.026	0.040	0.008	0.122	0.063	0.171
f	0.119		0.021		0.005		0.078		0.007	

To propose a quantitative understanding of the inverse iteration procedure, Fig. 7.5a shows the variations of CZM parameters (only the parameter values of the interfacial areas from the initial, the middle and the end of the tearing path) with iteration numbers of inverse modeling of tearing experiment for sample FCT-1. It is noted that the predicted interfacial strength and critical energy release rate converged to certain values after approximately 30 iterations. The convergence trend of the objective function is shown in

Fig. 7.5b, and the value is quickly reduced from a large value to a small value after seven iterations.

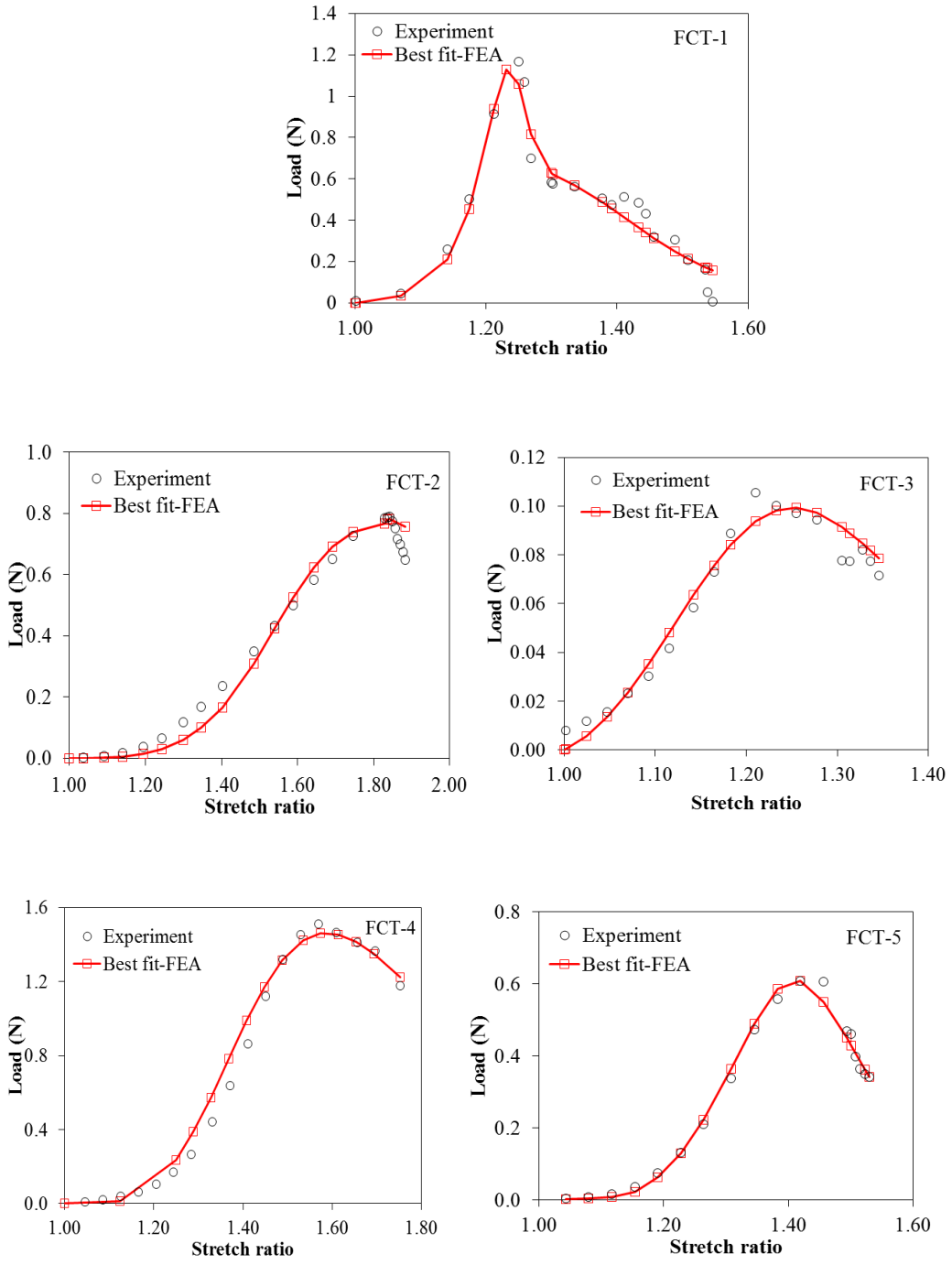


Fig. 7.4 The simulation predicted load-displacement curves of loading-tearing cycles are compared with the experimental measured curves.

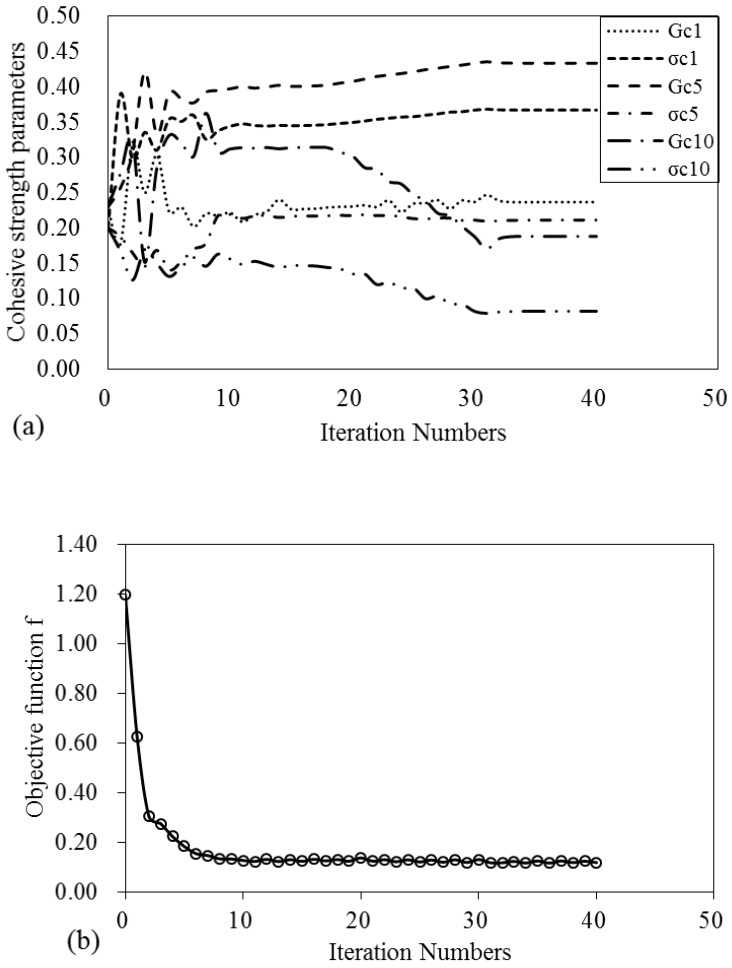


Fig. 7.5 (a) Variations of CZM parameters and (b) objective function with iteration numbers of inverse modeling of tearing experiment for sample FCT-1.

7.4.3 Finite Element Results of the Fibrous Cap Tearing Process

The simulation predicted tension stress (S22) contours for eight typical points along the loading-displacement curve during the tearing process are shown in Fig. 7.6. The states of deformation of specimen from experiment (Fig. 7.6a) and the tension stress contours (Fig. 7.6b) are consistent with the corresponding loading levels in the load-displacement diagram. At the beginning of the tearing test (Fig. 7.6a, at point 1), the sample deforms (Fig. 7.6a and 7.6b, at points 2 and 3) with extension along Y direction to the time point when the maximum tension stress occurs (Fig. 7.6a and 7.6b, at point 4). The loading level

at point 4 is the highest level and is sufficient to initiate the tearing, and the tension stress contour shows that the highest tension stress occurs in the cohesive interface and also the bulk material. After that, the tension stress decreases with the tear propagates along the tearing path (Fig. 7.6a and 7.6b, at points 5 and 6). At the loading point 7, the tearing propagation stops and the rest part of the tearing path (cohesive interface elements) deform with large extension which similar to the uniaxial tension test. At last, the tearing propagation of fibrous cap begins when resistant force decreases (Fig. 7.6a and 7.6b, at point 8).

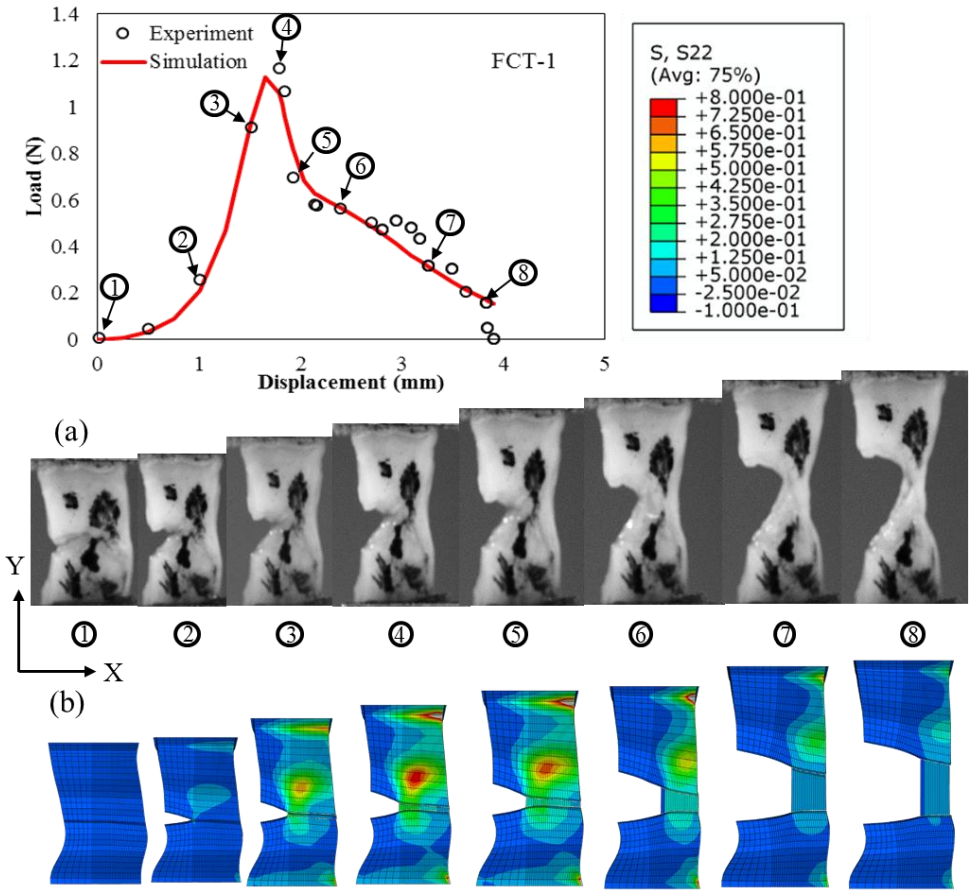


Fig. 7.6 Tension stress (S22, along Y direction) contours at eight typical points along the load-displacement curve during tearing process: (a) tension deformation from experiment and (b) simulation prediction.

7.5 Discussion

For the acquiring of HGO model parameter values, uniaxial tensile tests on five fibrous cap samples were used. Since the mechanical behavior play an important role in determination of the critical energy release rate and the interfacial strength across the thickness of fibrous cap, the HGO parameter values were obtained through the inverse modeling method. Though the shear modulus of the matrix material μ are in the range 1 kPa to 2.55 kPa, which are less than the values from the reference (43.78 kPa (Kiousis et al., 2009) and 24.12 kPa (Balzani et al., 2012)). However, the fiber reinforced response is associated with the constitutive parameters k_1 and k_2, which dominate the mechanical behavior. And the values of k_1 and k_2 are within the same range as those in the reference.

Moreover, for the simulation of arterial tissue delamination, the ultimate tensile stress has been used as the cohesive interfacial strength of CZM (Ferrara and Pandolfi, 2010; Gasser and Holzapfel, 2006). In the present study, it was found that the values of cohesive interfacial strength of the fibrous cap along circumferential direction are in the range from 0.029 to 0.572 MPa (0.296±0.176 MPa, mean±S.D.). These values are in good agreement with the values of ultimate tensile stress obtained by other researchers: Lawlor et al. (Lawlor et al., 2011) have observed the values of ultimate tensile stress of fresh carotid artery plaques from circumferential direction using uniaxial tensile test, which are in the range between 0.131and 0.779 MPa (0.367±0.213 MPa, mean±S.D.). Teng et al. (Teng et al., 2015) have performed uniaxial tensile tests on human carotid fibrous cap in the circumferential direction, the mean ultimate strength of fibrous cap is 0.158 [0.072, 0.259] MPa. Holzapfel et al. (Holzapfel et al., 2004b) have reported that the ultimate tensile stress of human carotid fibrous cap in the circumferential direction is 0.255±0.08 MPa.

The values of critical energy release rate across the thickness of fibrous cap obtained in the current study are in the range from 0.085 to 1.428 N/mm (0.533±0.449 N/mm), which show a large variation from specimen to specimen or from position to position of one specimen. Under the same load conditions, the fibrous cap with lower energy release rate values will prone to break, or the positions of one fibrous cap with lower G_c will start tearing firstly. From previous studies of human fibrous cap delamination from the underlying plaque tissue, the critical energy release rate ranged from 0.132 to 0.695 N/mm, with a mean of 0.254±0.155 N/mm (Leng et al., 2016). The values across the thickness of fibrous cap are larger than those between the fibrous cap and underlying tissue from the limit studies. Furthermore, the critical energy release rate has a large effect to failure mechanism of the atherosclerotic plaque. For one thing, the damage and dissection propagation will occur at the interface between fibrous cap and underlying tissue. For another thing, the fibrous cap will prone to tear across the thickness that the whole plaque tissue will be exposed to the blood vessel when the fibrous cap is weaker.

There are some limitations for the current work. First, the geometry models were built from images of front view and side view, which the thicknesses were assumed constant along the direction along width of the sample. Secondly, the samples under uniaxial tensile tests are not underwent pure tensile deformation for the shearing forces may occur inside the samples with large width-length ratio. Third, the HGO model parameter values identified from this study were from a single stretch ratio which may not well characterize the mechanical behaviors of the tearing tests of arterial tissue. Since the stretch ratios of the tearing tests are larger than those from the uniaxial tensile tests. The further limitation is the inverse modeling method used in current study. The material

parameter values were obtained from a local optimal process (Lei and Szeri, 2007), so other combinations of different parameter values can characterize a similar mechanical response as the set of parameters in the current study.

7.6 Conclusions

In the current study, an inverse analysis method and a finite element based modeling approach for simulating human fibrous cap tearing event have been developed and demonstrated in order to acquire the cohesive interface parameter values. Simulations of human fibrous cap tearing experiments have been carried out, in which the HGO model for the bulk material behavior and the CZM for the tearing behavior along the tearing path are adopted. By implementation of the inverse modeling of the uniaxial tensile tests of human fibrous cap, the HGO parameter values were obtained and used as the input values for the bulk material model to model the fibrous cap tearing process. With the same inverse analysis method, the cohesive interfacial strength and critical energy release rate across the thickness of fibrous cap were acquired.

Comparisons of simulation predictions of the load-displacement curve from inverse modeling with experimental measurements revealed that the simulation predictions were able to characterize the critical features of the deformation states of specimen for the human fibrous cap tearing tests. The results of this study provide a finite element based inverse analysis method to obtain the material parameter values from the simulations of arterial tissue failure events using CZM approach.

CHAPTER 8

EXPERIMENTAL AND NUMERICAL STUDIES OF COLLAGEN FIBER FAILURE IN ARTERIAL TISSUE

8.1 Introduction

We have successfully developed a mechanical modeling approach ((Leng et al., 2015b; Leng et al., 2016)) for arterial tissue failure in the form of plaque delamination (dissection) along the plaque-media interface and fibrous cap delamination along fibrous cap-underlying plaque tissue interface. However, the arterial tissue is a complex, laminated structure which contains several types of fiber reinforcing elements such as fiber bridges extending perpendicular to the interface between plaque and media or fibrous cap and underlying plaque tissue. The macro-scale cohesive zone model (CZM) approach is useful for the understanding of the overall arterial delamination behavior; it does not give the descriptions of the micromechanical physical basis for the arterial tissue delamination process. Furthermore, the structural elements in the artery compose of individual cells and extracellular matrix fibers (Twal et al., 2013). These individual components are affected by most drug treatments in the form of changing the relative amounts, mechanical properties, or interactions between each other (SIMPSON and BOUCEK, 1983). Therefore, to determine whether an intervention will prevent the arterial tissue failure, we need to know how the mechanical properties and organization of the individual components at the

microscale, especially the collagen fibers, contribute to the adhesive strength of interfaces in the arterial layers.

The aims of this study are to go beyond the scope of the existing studies (e.g. (Ferrara and Pandolfi, 2010; Gasser and Holzapfel, 2007; Gasser and Holzapfel, 2006; Leng et al., 2015b)) to gain a mechanical understanding of the plaque rupture phenomenon at the microscopic scale. Firstly, a uniaxial tensile test on a single tow of collagen fibers from porcine arterial wall was performed in order to acquire the elastic modulus, tensile strength and strain at failure. Secondly, the interfacial strength of interface across fibers was obtained through best fitting of the load-displacement curve from the simulation predictions with the experimental measurements. Finally, these parameter values were used as input data for a micromechanical model of a plaque-arterial wall system, which was developed based on experimental observations and the cohesive zone model approach. The failure mechanism at the microscopic scale (such as possible collagen fiber breakage) was incorporated to develop a three-dimensional unit cell model, which will enable the characterization of the cohesive traction-separation relation and the factors at the micromechanical scale affecting this relation that plays an important role for the understanding of micromechanical mechanism in plaque rupture.

8.2 Materials and Methods

Specimen Preparation

All tissue handling protocols were approved by the Institutional Animal Care and Use Committee at the University of South Carolina. The porcine abdominal aorta was harvested from the kidneys of the male Landrace Pigs (age 8-12 months, mass 60-70 kg).

All kidneys were acquired immediately after animal sacrifice and placed on ice for transport to laboratory. Upon kidney arrival, the abdominal aorta was isolated from the surrounding tissue, washed in phosphate buffered saline (PBS), dissected free of perivascular tissue. Strips of 20 mm ×10 mm were cut using surgical scissors (Fig. 8.1a). Scalpel was used to make a 2 mm long cut in the middle of the strip and tear it apart, releasing the collagen fibers embedded in the tissue. The separated surfaces obtained from this process is similar to those from the arterial tissue dissection and delamination processes. Hence, the shape and diameter of collagen fibers obtained are the same as the fibers along the surfaces from the delamination or dissection experiment of arterial tissue. A part of separated surface is shown in Fig. 8.1b, where several bundles of collagen fibers distribute randomly and connect to each other. Six specimens were harvested at the separated surface, which are consisted with bundles of collagen fibers twisted together.

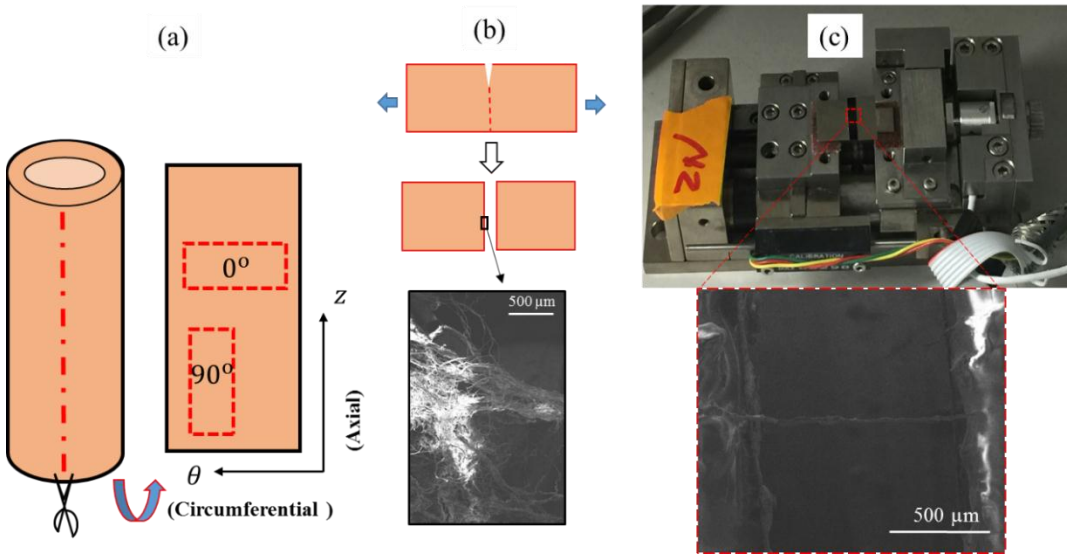


Fig. 8.1 Schematic of set-up for tensile testing in SEM. (a) A radial cut was made on the porcine abdominal aorta and strips oriented at the angle of 0° and 90° with respect to the circumferential vessel axis were obtained; (b) a strip was teared into two parts and a bundle of collagen fibers was harvested at the teared surface; (c) collagen fiber uniaxial tensile test setup.

Uniaxial Tensile Tests of Collagen Fibers

Both ends of fibers were clamped onto a GatanTM Deben micro-tester (Gatan, Inc., Pleasanton, CA) equipped with a 2 N load cell (Fig. 8.1c). The fibers together with micro-tester was fixed into a scanning electron microscope (SEM: FEI Quanta 400) for in-situ tensile tests. The loading speed was set as 1 mm/min. The completely fiber uniaxial tensile test was recorded by a video to reveal the corresponding deformation and fracture processes, and to ensure the validity of such tests.

8.3 Numerical Implementation

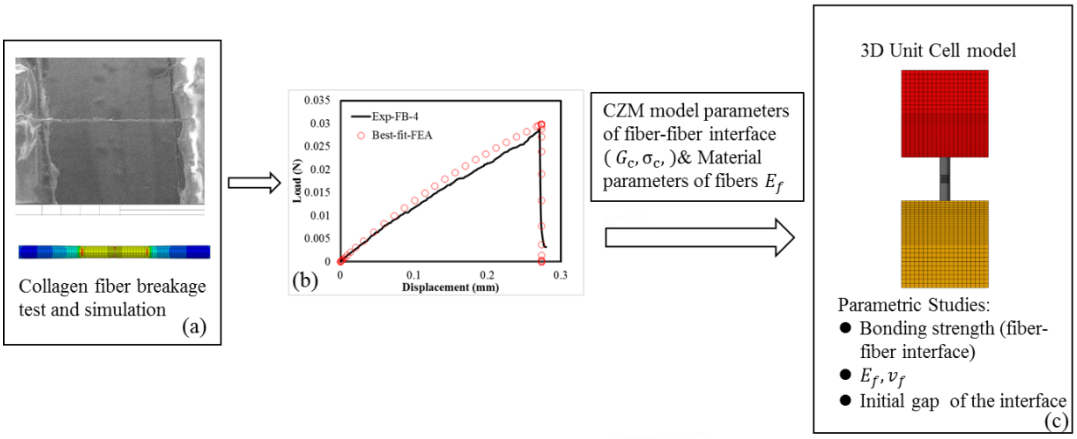


Fig. 8.2 Schematic representation of the numerical implementation of micromechanical model with fiber breakage. (a) SEM image of collagen fibers from the uniaxial tensile test and FE model of collagen fibers; (b) best fitting of load vs. load-point displacement curve between the simulation predictions and experimental measurements; (c) Schematic illustration of parametric studies using 3D unit cell model.

In order to investigate the micro-mechanism of collagen fiber failure, a 3D unit cell model was implemented in the numerical studies. First, the CZM parameter values of the fiber-fiber interface (interface across the collagen fibers) were identified via fitting the simulation predictions of load vs. load-point displacement curve with experimental

measurements (Fig. 8.2a and 8.2b). Then, the CZM parameter values were used as input data for the parametric studies using the micromechanical model (Fig. 8.2c).

8.4 Material Properties Identification Process

The values for the interfacial strength and critical energy release rate of interface across fibers (fiber-fiber interface) as well as the modulus of collagen fibers were obtained via fitting simulation predictions with experimental measurements of the load vs. load-point displacement curve.

8.4.1 Material Properties of Fiber-Fiber Interface and Collagen Fibers

Geometrical Modeling

The geometric models of the collagen fibers were reconstructed from the images obtained during the tensile tests (Fig. 8.2a). The length and diameter of the specimen were measured directly from the experimental images (Fig. 8.3a). For simplification, the shape of the cross-section is assumed to be a circular section (Wang et al., 1994).

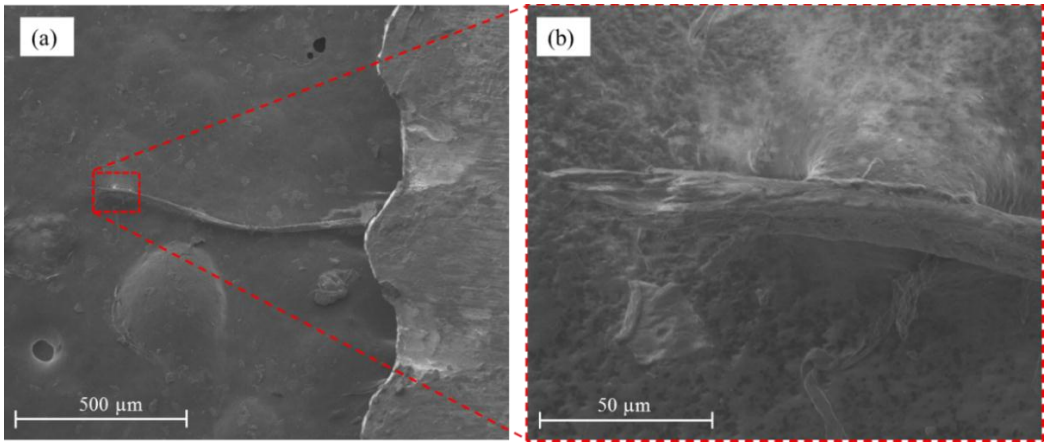


Fig. 8.3 (a) SEM image of fibers after the tensile test and (b) the zoom-in image of the breakage surface of the collagen fibers.

Meshing

The geometric model of the fibers was meshed with eight-node brick elements (C3D8). The zero thickness eight-node 3D user-defined elements were placed at the cross-section perpendicular to the longitudinal axis where the fiber breakage occurred in the experiment.

Boundary Conditions

In line with the experiments, the left end of the fibers was fixed, the load applied on the right end with loading rate 1.0 mm/min. Except for the fixed part of the model, all other surfaces of FE model were set to a traction-free boundary condition.

8.5 Results

8.5.1 Material Properties of Collagen Fibers

The equations for calculating the Cauchy stress and strain are given as follows,

$$\sigma = \frac{F}{A_0}\left(1 + \frac{\Delta L}{L_0}\right), \varepsilon = In\left(1 + \frac{\Delta L}{L_0}\right) \tag{8.1}$$

where σ and ε are the Cauchy stress and strain, respectively; F is the resultant load in the tensile testing; A_0 and L_0 represent the initial cross-section and length of the fibers, respectively; ΔL denotes the increment of length during the fiber tensile test. The Cauchy stress-strain curves of all specimens for fiber breakage (FB) tests (uniaxial tensile tests) are shown in Fig. 8.4. The strain at failure and ultimate tensile strength were 23.00 ± 7.30 % and 81.75 ± 75.14 MPa (Table 8.1), respectively.

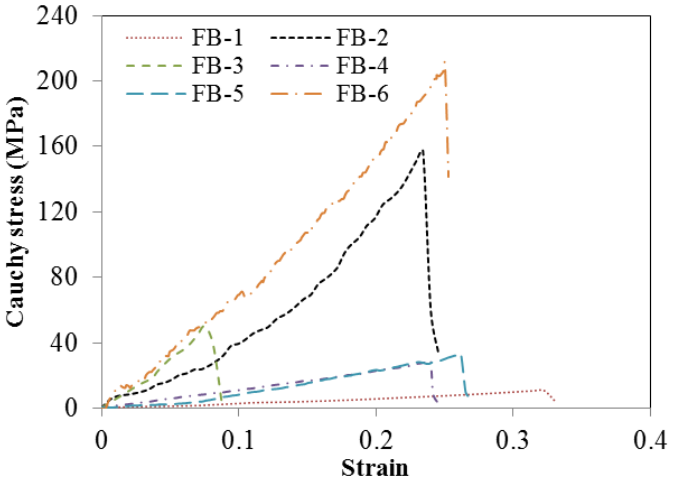


Fig. 8.4 Cauchy stress-strain curves from collagen fiber tensile tests.

Table 8.1 Diameter, strain at failure and ultimate strength from fiber tensile tests.

	FB-1	FB-2	FB-3	FB-4	FB-5	FB-6	Mean	S.D.
Diameter, D (μm)	28.6	11.1	16.8	39.5	32.3	12.4	23.5	10.7
Strain at failure (%)	32	23	8	24	26	25	23.00	7.30
Ultimate Strength (MPa)	10.81	156.88	50.29	28.34	32.35	211.82	81.75	75.14

8.5.2 CZM Parameter Values of Fiber-Fiber Interface

The CZM parameter values for the interface across the fibers were obtained through a numerical identification procedure that matches simulation predictions of the load vs. load-point displacement curve with the experimental measurements (Leng et al., 2015b; Leng et al., 2016; Shazly et al., 2014), as shown in Fig. 8.5. The tangential modulus and ultimate tensile strength quantified from the fiber tensile tests were used as input data as the modulus E of fibers and interfacial strength σ_c of fiber-fiber interface in the parameters identification procedure, respectively. The initial guess of critical energy release rate G_c was chosen according to the critical energy release rate of fibrous cap delamination tests

(Leng et al., 2016). The value of Poisson's ratio ν of fibers was taken to be 0.3 (Genin et al., 2009).

In the numerical identification process, the modulus and Poisson's ratio of fibers and the CZM parameter values of interface across fibers were considered "acceptable" when the root mean square error satisfies

$$f_r = \frac{\sqrt{\frac{\chi^2}{N-M}}}{F_{avg}} < 0.005 \text{ , with } \chi^2 = \sum_{i=1}^{N} \left[\left(F_{exp} - F_{sim} \right)_i^2 \right] \quad (50)$$

where F_{sim} and F_{exp} are the simulation predicted and the experimentally measured resultant loads; F_{avg} is the sum of all experimentally measured forces divided by the number of data points; N is the number of data points on the load-displacement curve which were used in the parameter value identification procedure; and M is the number of parameters whose values were determined from the identification procedure.

A proper set of modulus and Poisson's ratio of fibers and the CZM parameter values of interface across fibers is shown in Table 8.2. It is noted that the values for K and λ were assumed equal to 1 N/mm^3 and 1, respectively. These values are reasonable since the K value is sufficiently large that artificial compliance from the cohesive interface can be prevented and the values for mixity parameter λ is reasonable for the mode I fracture process of collagen fiber breakage process (Leng et al., 2015b; Leng et al., 2016).

Table 8.2 Modulus and CZM parameter values of collagen fibers

	FB-1	FB-2	FB-3	FB-4	FB-5	FB-6	Mean	S.D.
Modulus, E (MPa)	28.02	850	534.38	118.08	105.14	781.28	402.82	334.33
G_c (N/mm)	0.005	0.32	0.21	0.1	0.15	0.47	0.209	0.151
σ_c (MPa)	11.32	160.82	55.75	28.34	29.39	211.82	82.91	75.71
f_r	0.0003	0.0023	0.0009	0.0047	0.0037	0.0008	0.0021	0.0016

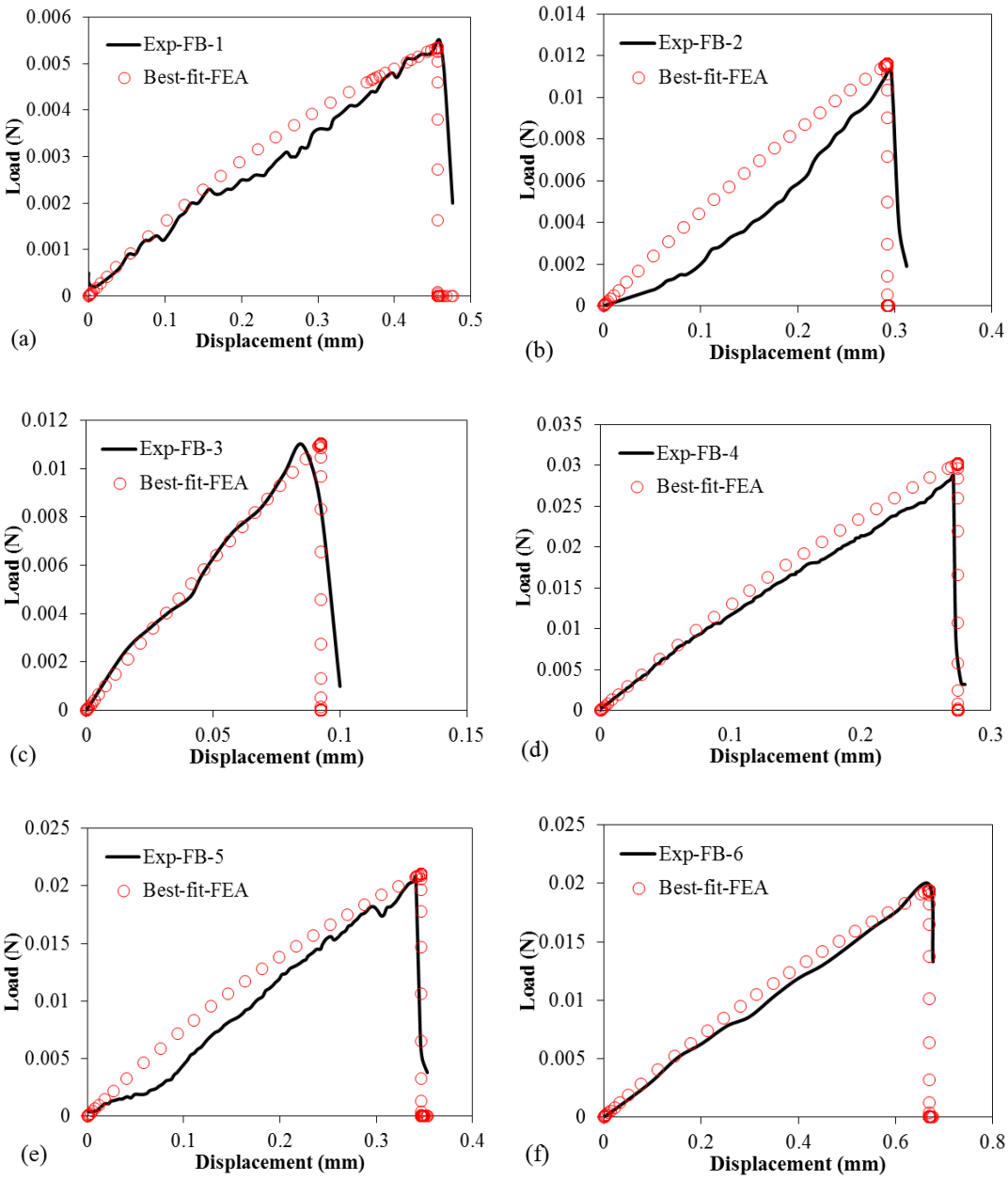


Fig. 8.5 The simulation predicted load-displacement curves of tensile tests of collagen fibers are compared with the experimental measured curves.

8.6 Parametric Studies

A micromechanical model was proposed to characterize the arterial delamination mechanics at the fibrous cap-underlying plaque tissue interface in terms of the mechanical

properties and geometry of fibrous components including bridging fibers. A 3D unit cell containing a set of fibers between two arterial tissue layers was considered (Fig. 8.6).

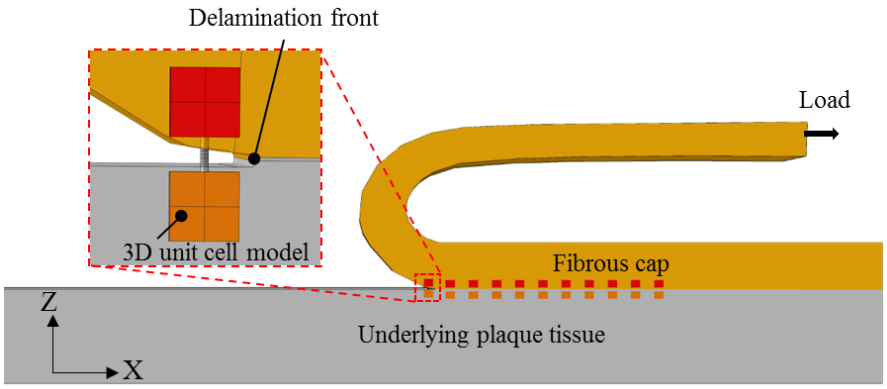


Fig. 8.6 Schematic representation of 3D unit cell models distributed in the fibrous cap delamination path.

The top and bottom arterial tissue layers were modeled as hyperelastic anisotropic materials (HGO model) and the fibers were treated as a linear elastic material. In order to investigate the factors affecting the traction-separation response of delamination process at the micro scale, the parametric studies based on the 3D unit cell model was implemented, which considering: (1) the bonding strength of interface across the fibers; (2) variations in the fibers' stress-strain behavior; (3) initial gap of the interface.

8.6.1 3D Unit Cell Model for the Arterial Tissue Delamination

Geometrical Modeling

The geometry values are shown in Fig. 8.7, which are chose according to the average value of diameters of fibers in Table 1.

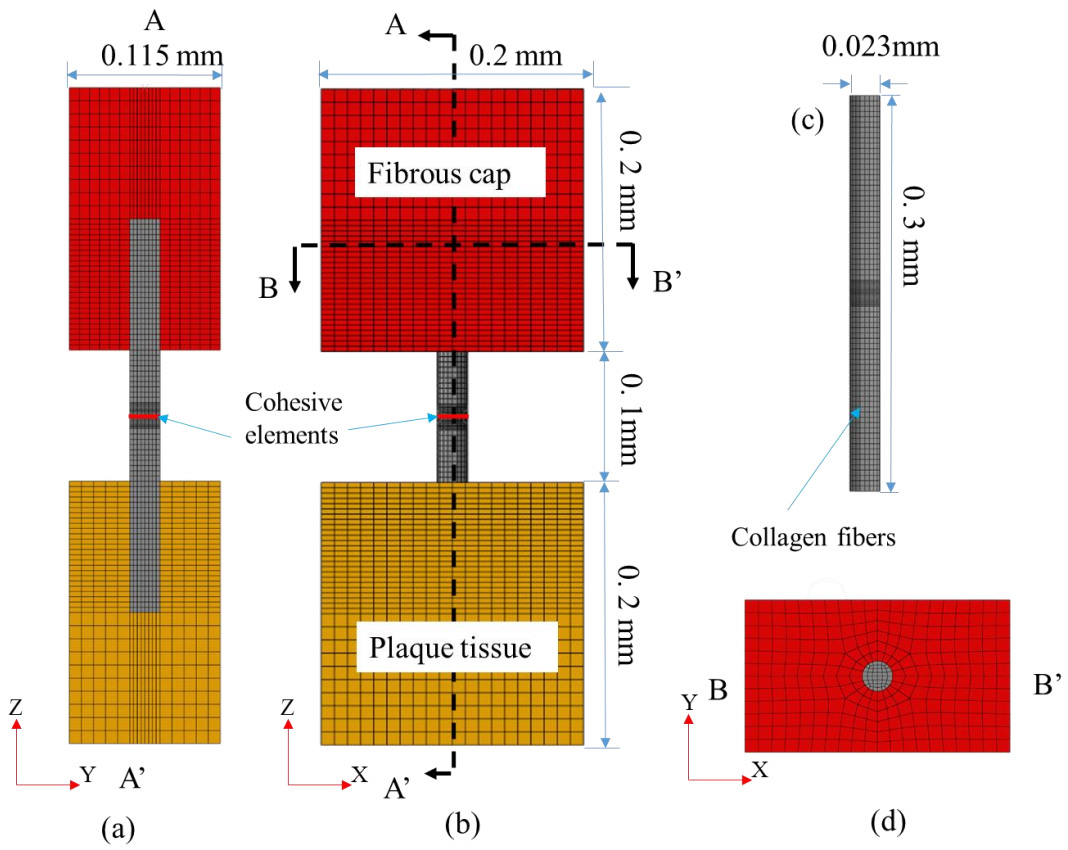


Fig. 8.7 Finite element model of the 3D unit cell model for micromechanical study of fibrous cap delamination: (a) left section view of 3D unit cell model, the collagen fibers connecting fibrous cap and underlying plaque tissue (the red line shows a zero thickness layer of cohesive elements assigned to the interface across fibers at the middle of fibers); (b) front view of 3D unit cell model; (c) collagen fibers; (d) top section view of 3D unit cell model.

Meshing

The eight-node brick elements (C3D8H) are implemented for the matrix part (contains collagen fibers and smooth muscle cells, etc.). The interface across the fibers is placed with zero thickness eight-node 3D user-defined elements. The meshed geometric model of 3D unit cell is shown in Fig. 8.7.

Boundary conditions

The unit cell has symmetry conditions on the left and right vertical boundaries of the layers and is loaded in tension at the top and bottom boundaries by a uniform displacement. The 3D unit cell can be taken as a small part inside the human fibrous cap delamination model (Fig. 8.6). The boundary conditions should according to the stress states in the macro model. To this end, the front and back surfaces (perpendicular to the x axial) of the fibrous cap and underlying plaque tissue of the unit cell model were constrained along x direction (Constrain the deformation along the direction of length of fibrous cap, as shown in Fig. 8.6); and the left and right surfaces (perpendicular to the y axial) were set with restriction of y direction along the width of the fibrous cap and underlying plaque tissue during delamination test. The total reaction loads are determined from finite element solutions. The resulting relation between the applied displacement and the reaction load was used to analyze the traction-separation relation of the cohesive interface between the two arterial layers.

The material parameter values of HGO model for matrix material are shown in Table 8.3 (Leng et al., 2016).

Table 8.3 Material parameter values of HGO model

	μ (kPa)	k_1 (kPa)	k_2(-)	κ (-)	r (degree)
Plaque	49.45	23.7	2630	0.226	30
Fibrous cap	21.89	93.63	7957	0.226	17.22

The linear elastic model was used to characterize the mechanical behavior of bulk material of collagen fibers, which includes parameters such as the elastic modulus and Poisson's ratio. A CZM model was adopted to describe the stiffening and softening

behavior of collagen fibers during the tensile tests. The reference material parameter values of elastic modulus, interfacial strength and critical energy release rate for the 3D unit model were set equal to the average values of the parameters obtained from the experiment as shown in Table 8.3 (G_c=0.209 N/mm, σ_c=82.91 MPa, E=402.82 MPa and ν=0.3) .

One set of the traction-separation curves from simulation predictions using 3D unit cell model is shown in Fig. 8.8a. Traction is obtained through dividing the resultant force by the area of the fibrous cap-underlying plaque tissue interface (0.023mm^2) and the separation is the load-point displacement. At the beginning of the traction-separation curve, the traction increases because of the resistance force from the interface across fibers and the matrix material. Further, the maximum traction occurs when the stress of interface across fibers equal to the interfacial strength. At last, the traction decreases to zero when the cohesive elements of the interface across fibers are completely damage.

8.6.2 Bonding Strength of Interface across the Fibers

Collagen fibers are the major load-bearing structural constituents in the vascular tissue, which increase strength exponentially at higher strains. Hence, collagen fiber breakage is considered as the main contribution to the arterial tissue failure (Pal et al., 2014). In this section, we focus on the effects of bonding strength of interface across the collagen fibers to study the traction-separation relationship of the interface between two arterial layers including fiber bridging. To gain some insight into the effect of G_c, five values for the G_c are considered: 0.01 N/mm, 0.05 N/mm, 0.1 N/mm, 0.209 N/mm and 0.4 N/mm. Furthermore, to investigate the effect of the interfacial strength on simulation predictions, five values of σ_c are considered: 50 MPa, 82.91 MPa, 100 MPa, 150 MPa and 200 MPa. All other aspects of the simulation model keep the same.

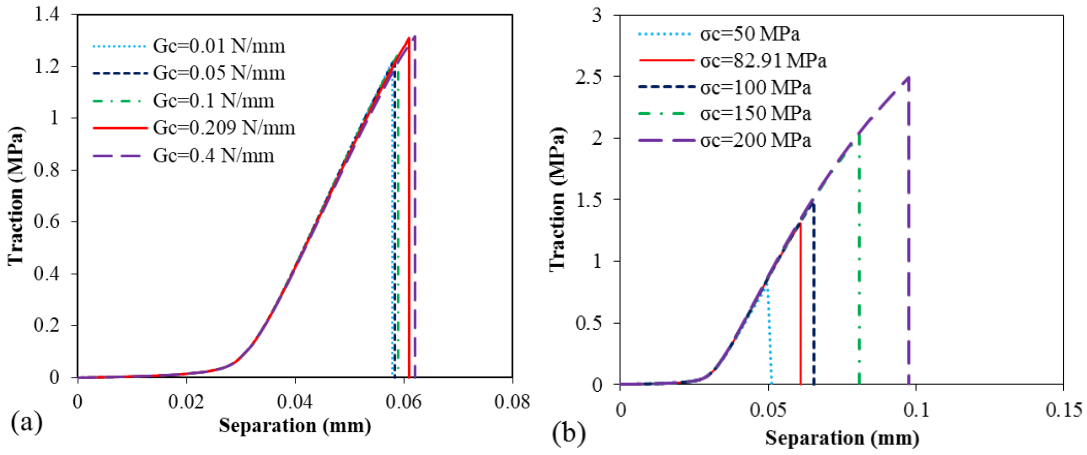


Fig. 8.8 Traction-separation curves from simulation predictions with five different values of (a) critical energy release rate G_c and (b) interfacial strength σ_c.

The predicted traction-separation curves are shown in Fig. 8.8. It is seen that the traction increases with increasing critical energy release rate G_c. Moreover, the traction is largely affected by the interfacial strength that the traction increases with increasing σ_c, but the stiffness is not affected by the interfacial strength.

8.6.3 Variations in the Fibers' Stress-strain Behavior

In order to gain insight into the effect of the elastic modulus E on traction-separation relation for unit cell model, five values are considered: 402.82 MPa, 500 MPa, 600 MPa, 700 MPa and 800 MPa. Furthermore, to investigate the effect of the Poisson's ratio ν on simulation predictions, five values of ν are considered: 0.1, 0.2, 0.3, 0.4 and 0.499. Using these elastic modulus and Poisson's ratio, ten simulations were carried out (as shown in Fig. 8.9), each with a different E or ν. Other values are kept the same in all simulations. The simulation predicted traction-separation curves are shown in Fig. 8.9. It is seen that the traction and the stiffness increase with increasing of elastic modulus and the traction decreases with increasing of Poisson's ratio.

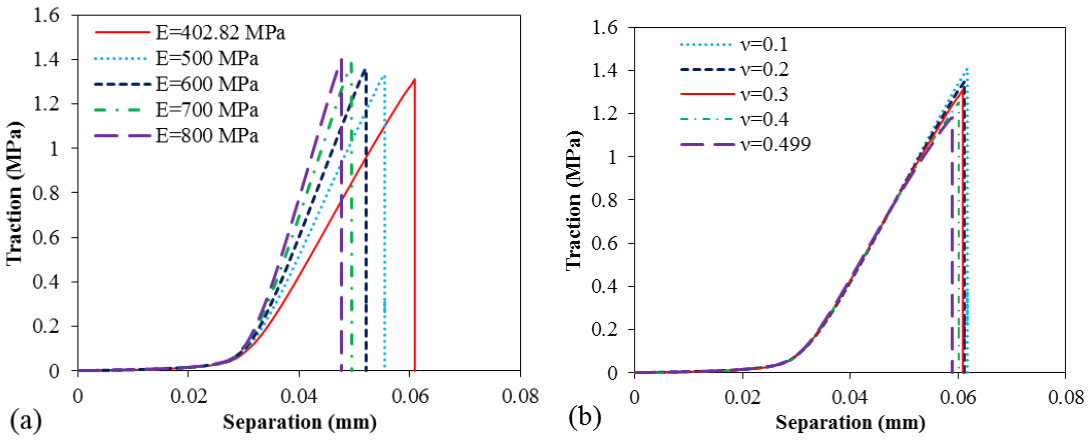


Fig 8.9 Traction-separation curves from simulations with five different values of (a) elastic modulus E and (b) Poisson's ratio ν.

8.6.4 The Initial Gap of the Interface

Considering the effect of the initial gap of the interface l_g on traction-separation relation for unit cell model, five values are considered: 0 mm, 0.05 mm, 0.1 mm, 0.15 mm and 0.2 mm. All other aspects of the simulation model are kept the same.

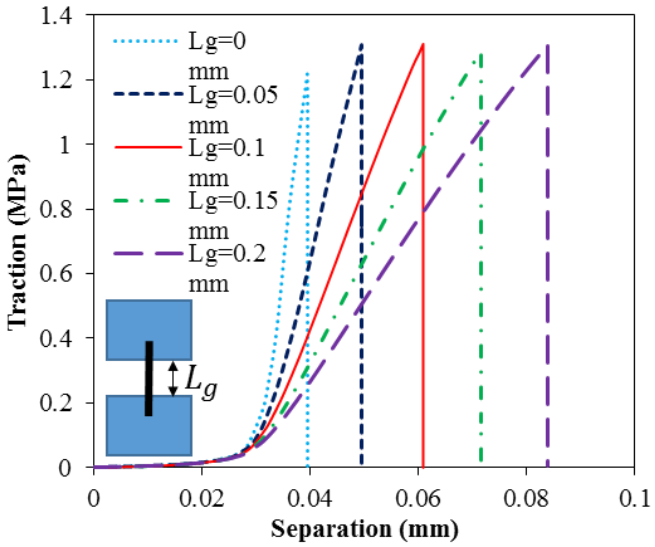


Fig. 8.10 Traction-separation curves from simulations with five different values of initial gap of the interface L_g.

The simulation predicted traction-separation curves are shown in Fig. 8.10. It is seen that the stiffness increases with decreasing of initial gap of the interface and the predicted maximum traction is only slightly affected by the initial gap of the interface.

8.7 Discussion

For the tensile tests, the fibers is composed of several bundles of collagen fibers. During the collagen fiber breakage process, the lamellae sliding occurred and it was also associated with fibril pulling out and breakage (Ikoma et al., 2003). Because some of the collagen fibers are attached to the matrix and connected to other collagen fibers (Fig. 8.1b), the arterial failure process may contain separation of matrix material and collagen fiber pull-out. Thus, the debonding and slippage of fibers embedded within the matrix may occur, but the main contribution of the micromechanical behavior of arterial delamination is the breakage of fibers perpendicular to the delamination interface (Pal et al., 2014).

In the present study, the fibers contain bundles of collagen fibers (the diameters of fibers in the current study are larger than that of collagen fibers which ranged from 1 to 10 μm (Miyazaki and Hayashi, 1999)). It was found that the strain at failure, ultimate strength and elastic modulus of fibers are 23.00 ± 7.3 %, 81.75 ± 75.14 MPa and 402.82 ± 334.33 MPa, respectively. Miyazaki and Hayashi (Miyazaki and Hayashi, 1999) have observed the mechanical properties of single collagen fibers isolated from rabbit patellar tendon and the failure strain, ultimate strength and elastic modulus are 21.6±3.0 %, 8.5±2.6 MPa and 54.3±25.1 MPa, respectively. Except for the values of strain at failure obtained in this study are in line with those from tensile tests of single collagen fibers, the ultimate strength and elastic modulus obtained from tensile tests of bundles of collagen fibers from porcine aorta are larger than the values from Miyazaki's research. Yamamoto et al. (Yamamoto et al.,

1999) acquired the tensile properties of collagen fascicles (consists of collagen fibrils, fibers, interfibrillar matrix and fibroblasts (Miyazaki and Hayashi, 1999), the diameter is approximately 300 μm (Yamamoto et al., 1999)) from rabbit patellar tendons, and the strain at failure, ultimate strength and elastic modulus are 10.9±1.6 %, 17.2±4.1 MPa and 216±68 MPa, respectively. The values of strain at failure, ultimate strength and elastic modulus are less than those from the present study. The differences may attribute to the different tissue source of the collagen fibers, the different geometric or structural properties of the samples.

For the identification of CZM parameter values of interface across collagen fibers, the deformation of fibers should correlate to that from tensile tests. It was noted that the fibers was stretched during the tensile test until the fiber breakage occurred at the last time point with load completely dropping to zero. Moreover, the maximum effective displacement when the interface is damaged completely is very small compared to the length of fibers. Experimental results show a nonlinearity of the mechanical response which is attributed to the nonlinear mechanical response of elastin and the gradually recruited load-bearing collagen fibers as they straighten out with increasing strain. At the last stage, the softening behavior of the interface across the fibers occurs and the interface damage completely with the traction dropping to zero.

For the 3D unit cell model, the parts of matrix material including fibrous cap and underlying plaque tissue were created according to the dimension of the arterial layers. The thickness, length and width should be small enough to attain a good numerical efficiency and also to eliminate the effects from the boundary conditions. For the parametric studies, the material parameter values for the CZM model and elastic model of fibers were chosen within the range of the values obtained from the experiments (Table 8.1and Table 8.2) in

order to simulate the actual failure process. The predicted maximum traction is largely affected by the critical energy release rate, interfacial strength and Poisson's ratio while the stiffness of the traction-separation curves is affected by the elastic modulus of fibers and the initial gap of the interface. The damage accumulates as the fibers be elongated and its magnitude reaches 1 when the tractions of the 3D unit cell model as well as the tractions of cohesive elements decrease to zero after attaining the maximum values. Meanwhile, the cohesive element is completely damage and the two layers of the 3D unit cell model are separated.

In one reference (SIMPSON and BOUCEK, 1983), It mentioned that the medicine act by decreasing the aortic tensile strengths to increase the high percentage of the animal death from the aortic dissecting aneurysms. It is noted that the drugs increase the ultrastructural disruption of collagen and decrease the arterial strength. For this reason, the increasing of critical energy release rate and interfacial strength of interface across fibers will increase the traction of the unit cell along the failure path, which will inhibit the arterial failure. Meanwhile, the effective displacement when the maximum traction of unit cell attained will increase, which will also prevent the damage of arterial tissue under certain deformation. The arterial stiffness increased with age and was taken as one factor to increase the cardiovascular disease (Janić et al., 2014). From the parametric studies, when the modulus of collagen fibers increases and the initial gap of the interface decreases, the stiffness of the interface prone to failure will increase, which will accelerate the damage of the interface under a certain small deformation. Therefore, the parametric studies using 3D unit cell will provide a possibility to investigate the mechanism of drug treatments to the arterial tissue failure.

Despite the novelty of some experimental observations and the encouraging predictive power of the proposed micromechanical model of the arterial tissue, certain limitations in our study should be recognized. Firstly, the fibers are assumed with constant cross-section area along the longitudinal direction, but actually the area of cross-section varies with irregular shape. Additionally, the fibers are composed of bundles of collagen fibers twisted together. Secondly, the cross-section of fibers were assumed to be a smooth interface perpendicular to the axial direction in the simulation of fiber breakage process. But, the breakage area may not be an ideal cross-section because the fibril pull-out and breakage occur inside the fibers.

8.8 Conclusions

In the current study, a 3D unit cell model was developed and applied successfully to do the parametric studies of the arterial tissue failure process at the microscopic scale. The mechanical behavior of the arterial layers (including parts of fibrous cap and underlying plaque tissue), collagen fibers and the interface across the fibers were represented by HGO anisotropic constitutive mode, linear elastic model and exponential CZM model, respectively. The CZM parameter values and elastic parameter values of fibers were obtained through material identification method that matching the load-displacement curve from simulation predictions of tensile tests of bundles of collagen fibers with the experimental measurements. The identified parameter values were then applied in the parametric studies using 3D unit cell model to investigate the cohesive traction-separation relation affected by factors at the micromechanical scale.

Comparisons of simulation predictions of the load-displacement curve with experimental measurements revealed that the simulation predictions were able to capture

the essential features of the load-displacement curve from the collagen fiber tensile tests and show good quantitative agreement with the experimental measurements. The results from the simulation predictions of fiber breakage provide a validation for the proposed CZM based approach for modeling and simulating collagen fiber breakage events. Furthermore, the parametric studies using 3D unit cell model provide a method to investigate the traction-separation relationship of fiber bridging across the arterial layers at the micromechanical scale. Considering the predicted maximum traction, it is largely affected by the critical energy release rate, interfacial strength and Poisson's ratio. For the stiffness of the traction-separation curve, it is affected by the elastic modulus of fibers and the initial gap of the interface.

CHAPTER 9

CONCLUSIONS AND FUTURE WORK

A cohesive zone model-based computational approach for modeling and simulating delamination experiments on atherosclerotic plaque, media and fibrous cap as well as the fibrous cap model I tearing and collagen fibers breakage events have developed and applied successfully to characterize arterial tissue failure.

For the simulations of plaque rupture at the plaque-media interface. The aortic wall is treated as a fiber-reinforced, highly deformable, incompressible material, and the Holzapfel-Gasser-Ogden (HGO) model is adopted for the aortic bulk material behavior. Cohesive elements are placed along the plaque-media interface along which delamination occurs. The 3D specimen geometric models are created based on images from the experiments and certain simplifying approximations. A set of HGO and CZM parameter values is determined based on values suggested in the literature and through matching simulation predictions of the load vs. load-point displacement curve with experimental measurements for one loading-delamination-unloading cycle. Using this set of parameter values, simulation predictions for four other loading-delamination-unloading cycles are obtained, which show good agreement with experimental measurements. The findings of the current study demonstrate the applicability of the CZM approach in arterial tissue failure simulations.

The delaminated mechanical responses of the porcine abdominal aorta under mix-mode and mode I delamination are quantified via mechanical testing. Mechanical data are used to parameterize and validate the structure-motivated constitutive model and the exponential cohesive zone model approach for simulations of the arterial wall delamination. This integrated theoretical-experimental approach is demonstrated by comparing the loading-delamination-unloading curve and the crack front between numerical simulation predictions and experimental measurements for two types of experiments. In addition, the mixed-mode delamination reveals a shear mode dominated fracture event whereas mode I delamination is purely an opening failure process. Experimental data and theoretical predictions of the arterial delamination provide a comprehensive description of the arterial delamination and aid in the predictions of abdominal aortic dissection.

In order to describe the hysteresis phenomenon of diseased arterial tissue, a viscoelastic anisotropic (VA) model for the bulk material behavior is extended from existing HGO constitutive model. A finite element model is developed for the fibrous cap delamination experiments, in which arterial layers (including fibrous cap and underlying plaque tissue) are represented by 3D solid elements based on the VA model and fibrous cap-underlying plaque tissue interface is characterized by interfacial CZM elements. Using the set of parameter values from fibrous cap delamination experiments and material parameter identification process, simulation predictions for fibrous cap delamination events are conducted, which match well with the experimental measurements. Results of this study demonstrate the applicability of the viscoelastic anisotropic model and the CZM approach for the simulation of diseased arterial tissue failure processes.

An inverse analysis method with finite element modeling and simulation approach is presented, which enables the analysis of fibrous cap Mode I tearing experiments for the purpose of acquiring the interfacial strength and critical energy release rate of the fibrous tissue across the thickness. A cohesive zone model (CZM) approach is applied to simulate the tearing of the fibrous cap tissue under uniaxial tensile tests along the circumferential direction and a fibers reinforced hyperelastic model (Holzapfel-Gasser-Ogden) is implemented for the mechanical response of bulk material. With the material parameter values of HGO model from inverse analysis process as the input for the bulk material, the interfacial strength and critical energy release rate along the tearing path or failure zones are obtained through the same method as material identification process of HGO model. Results of this study quantificational demonstrate the fibrous cap tissue mode I tearing failure processes.

In order to demonstrate the arterial tissue failure at the microscale, a cohesive CZM based approach is applied to develop a micromechanical model for arterial delamination along the interface between the fibrous cap and the underlying plaque tissue. A 3D unit cell containing an individual collagen fibers between two arterial tissue layers is considered. An exponential cohesive zone model (CZM) is applied to describe the stiffening and softening behaviors of fibers (bundles of collagen fibers) between the two arterial layers. The CZM parameter values and elastic parameter values of fibers are obtained through a material parameter identification method that matches the load-displacement curve from simulation predictions of tensile test of collagen fibers with experimental measurements. The identified parameter values are applied in the 3D unit cell model. Using the unit cell model, micromechanical factors affecting the resulting traction-separation relation for the

unit cell are investigated using a parametric approach, which considers CZM model parameters, elastic model parameters and the initial gap of the interface. Through this investigation, CZM parameter values that describe the fiber failure process and the tensile properties of the fibers are obtained. Results of the parametric studies demonstrate the applicability of the 3D unit cell model approach for studying the micromechanical mechanisms of arterial tissue failure processes.

The CZM approach developed in the current studies are not limited to simulating plaque delamination from the aortic wall, fibrous cap delamination from the underlying plaque tissue and so on. If proper experimental data are available so that CZM parameter values can be calibrated, the simulation procedure can be equally applied to rupture failure inside the plaque tissue or the arterial layers. This said, it is noted that the current studies seek to demonstrate and validate the numerical modeling approach for simulating material separation failure events in arterial tissues, which will provide a strong basis for its application to more clinically relevant arterial tissue failure events. The case of plaque delamination, fibrous cap delamination, aortic media delamination, fibrous cap tearing and collagen fiber breakage are chosen in these studies because these are the cases in which experimental data are available. These studies try to establish the credibility and viability of the CZM-based approach, so that it can be applied to more clinically relevant failure events of arterial tissue in the future.

Based on this dissertation, several open questions are proposed:

1) So far, a cohesive zone model was developed to simulate the mouse atherosclerotic plaque delamination and human fibrous cap delamination. However, the oscillation

of load from the delamination phase of loading-unloading cycles cannot be captured by the implementation of CZM method. Hence, a more reasonable model needs for further study. The fracture toughness of different tissue along the delamination path will be acquired through inverse analysis. The histological structures of specimens from the delamination tests will be used for creating geometry model with local tissue distribution. With the critical energy release rate for local materials, a structure based cohesive zone model will developed to mimic the oscillation of load during the delamination procedure.

2) Based on the validated CZM method, a 3D idealized diseased carotid artery model will be created, and cohesive elements will be inserted on the interfaces prone to failure from clinical observations. This model will be used to study the arterial tissue failure process during angioplasty and stenting.

3) The cohesive zone model will be employed to simulate three failure mechanisms at the microscopic scale: matrix (plaque and arterial wall) material separation, collagen fiber pull-out, and collagen fiber breakage. The plaque and arterial tissue forming the matrix material contain tiny fibers, presumably collagenous, which seem to be the dominant contributions to the adhesive strength of the interface between the plaque and arterial wall. According to this observation, a Micromechanical Cohesive Zone Model (MCZM) containing a set of fibers embedded in the matrix material will be considered. The failure of this MCZM has four stages as increasing tensile force is applied to it: (i) the separation of the matrix material; (ii) the fiber breakage; (iii) the combination of fiber breakage and fiber pull-out; (iv) the fiber pull-out.

REFERENCES

ABAQUS. 2013. Analysis user's manual version 6.12, Dassault Systemes Corp.

Ahmann, K.A., J.S. Weinbaum, S.L. Johnson, and R.T. Tranquillo. 2010. Fibrin degradation enhances vascular smooth muscle cell proliferation and matrix deposition in fibrin-based tissue constructs fabricated in vitro. *Tissue engineering. Part A* 16:3261-3270.

Alkhouli N, M.J., Green E, Bell J, Knight B, Liversedge N, Tham JC, Welbourn R, Shore AC, KosK, Winlove CP. 2013. The mechanical properties of human adipose tissues and their relationships to the structure and composition of the extracellular matrix. *Am J Physiol Endocrinol Metab* 305:E1427–E1435.

Antonova, M.L., P.S. Antonov, G.R. Marinov, M.V. Vlaskovska, and L.N. Kasakov. 2008. Viscoelastic characteristics of in vitro vital and devitalized rat aorta and human arterial prostheses. *Annals of biomedical engineering* 36:947-957.

Asawinee Danpinid, J.L., Elisa E. Konofagou, Chiang Mai,. 2009. Characterization of the stress-strain relationship of the abdominal aortic wall in vivo. *Conf Proc IEEE Eng Med Biol Soc* 1960-1963.

Assemat, P., and K. Hourigan. 2013. Evolution and rupture of vulnerable plaques: a review of mechanical effects. *ChronoPhysiology and Therapy* 23.

Badel, P., S. Avril, M.A. Sutton, and S.M. Lessner. 2014. Numerical simulation of arterial dissection during balloon angioplasty of atherosclerotic coronary arteries. *Journal of Biomechanics* 47:878-889.

Badimon, L., and G. Vilahur. 2014. Thrombosis formation on atherosclerotic lesions and plaque rupture. *Journal of internal medicine* 276:618-632.

Balzani, D., S. Brinkhues, and G.A. Holzapfel. 2012. Constitutive framework for the modeling of damage in collagenous soft tissues with application to arterial walls. *Computer Methods in Applied Mechanics and Engineering* 213–216:139-151.

Barenblatt, G.I. 1959. The formation of equilibrium cracks during brittle fracture. General ideas and hypotheses. Axially-symmetric cracks. *Journal of Applied Mathematics and Mechanics* 23:622-636.

Barrett, S.R., M.P. Sutcliffe, S. Howarth, Z.Y. Li, and J.H. Gillard. 2009. Experimental measurement of the mechanical properties of carotid atherothrombotic plaque fibrous cap. *Journal of biomechanics* 42:1650-1655.

Bentzon, J.F., F. Otsuka, R. Virmani, and E. Falk. 2014. Mechanisms of Plaque Formation and Rupture. *Circulation Research* 114:1852-1866.

Bernard, Y., H. Zimmermann, S. Chocron, J.-F. Litzler, B. Kastler, J.-P. Etievent, N. Meneveau, F. Schiele, and J.-P. Bassand. 2001. False lumen patency as a predictor of late outcome in aortic dissection. *The American Journal of Cardiology* 87:1378-1382.

Camacho, G.T., and M. Ortiz. 1996. Computational modelling of impact damage in brittle materials. *International Journal of Solids and Structures* 33:2899-2938.

Camanho, P.P., Dávila, C.G., de Moura, M.F. 2003. Numerical simulation of mixed-mode progressive delamination in composite materials. *Journal of Composite Materials* 37:1415-1438.

Cattell, M.A., P.S. Hasleton, and J.C. Anderson. 1993. Increased elastin content and decreased elastin concentration may be predisposing factors in dissecting aneurysms of human thoracic aorta. *Cardiovascular research* 27:176-181.

Chandra, N., H. Li, C. Shet, and H. Ghonem. 2002. Some issues in the application of cohesive zone models for metal–ceramic interfaces. *International Journal of Solids and Structures* 39:2827-2855.

Chen, X., X. Deng, and M.A. Sutton. 2013. Simulation of stable tearing crack growth events using the cohesive zone model approach. *Engineering Fracture Mechanics* 99:223-238.

Chen, X., X. Deng, M.A. Sutton, and P. Zavattieri. 2014. An inverse analysis of cohesive zone model parameter values for ductile crack growth simulations. *International Journal of Mechanical Sciences* 79:206-215.

Cheng, G.C., Loree, H. M., Kamm, R. D., Fishbein, M. C. and Lee, R. T. 1993. Distribution of circumferential stress in ruptured and stable atherosclerotic lesions: A structural analysis with histopathological correlation. *Circulation* 87:1179-1187.

Cilla, M., E. Pena, and M.A. Martinez. 2012. 3D computational parametric analysis of eccentric atheroma plaque: influence of axial and circumferential residual stresses. *Biomechanics and modeling in mechanobiology* 11:1001-1013.

Collins, M.J., Bersi, M., Wilson, E., Humphrey, J. D. 2011. Mechanical properties of suprarenal and infrarenal abdominal aorta: implications for mouse models of aneurysms. *Medical engineering & physics* 33:1262-1269.

Collins, M.J., Eberth, J. F., Wilson, E., Humphrey, J. D. 2012. Acute mechanical effects of elastase on the infrarenal mouse aorta: implications for models of aneurysms. *Journal of biomechanics* 45:660-665.

Comley K, F.N. 2009. The mechanical response of porcine adipose tissue. *ASME Journal of Biomechanical Engineering* 1-30.

Daugherty, A., and L. Cassis. 2002. Mechanisms of abdominal aortic aneurysm formation. *Curr Atheroscler Rep* 4:222-227.

DiFrancia, C., T.C. Ward, and R.O. Claus. 1996. The single-fibre pull-out test. 1: Review and interpretation. *Composites Part A: Applied Science and Manufacturing* 27:597-612.

Driessen, N.J., W. Wilson, C.V. Bouten, and F.P. Baaijens. 2004. A computational model for collagen fibre remodelling in the arterial wall. *Journal of theoretical biology* 226:53-64.

Dugdale, D.S. 1960. Yielding of steel sheets containing slits. *Journal of the Mechanics and Physics of Solids* 8:100-104.

Eberth, J.F., Taucer, A. I., Wilson, E., Humphrey, J. D. 2009. Mechanics of carotid arteries in a mouse model of Marfan Syndrome. *Annals of biomedical engineering* 37:1093-1104.

Enderling, H., N.R. Alexander, E.S. Clark, K.M. Branch, L. Estrada, C. Crooke, J. Jourquin, N. Lobdell, M.H. Zaman, S.A. Guelcher, A.R. Anderson, and A.M. Weaver. 2008. Dependence of invadopodia function on collagen fiber spacing and cross-linking: computational modeling and experimental evidence. *Biophysical journal* 95:2203-2218.

Ferrante, G., Presbitero, P., Whitbourn, R., Barlis, P. 2013. Current applications of optical coherence tomography for coronary intervention. *Intl. J. Cardiol.* 165:7-16.

Ferrara, A., and A. Pandolfi. 2010. A numerical study of arterial media dissection processes. *Int J Fract* 166:21-33.

Fung, Y.C. 1967. Elasticity of soft tissues in simple elongation. *Am J Physiol.* 213:1532-1544.

Fung, Y.C. 1973. Biorheology of soft tissues. *Biorheology* 10:139-155.

Fung, Y.C., K. Fronek, and P. Patitucci. 1979. Pseudoelasticity of arteries and the choice of its mathematical expression. *American Journal of Physiology - Heart and Circulatory Physiology* 237:H620-H631.

Gasser, T.C., and G. Holzapfel. 2007. Modeling Plaque Fissuring and Dissection during Balloon Angioplasty Intervention. *Ann Biomed Eng* 35:711-723.

Gasser, T.C., and G.A. Holzapfel. 2006. Modeling the propagation of arterial dissection. *European Journal of Mechanics - A/Solids* 25:617-633.

Gasser, T.C., R.W. Ogden, and G.A. Holzapfel. 2006. Hyperelastic modelling of arterial layers with distributed collagen fibre orientations. *Journal of the Royal Society, Interface / the Royal Society* 3:15-35.

Genin, G.M., A. Kent, V. Birman, B. Wopenka, J.D. Pasteris, P.J. Marquez, and S. Thomopoulos. 2009. Functional Grading of Mineral and Collagen in the Attachment of Tendon to Bone. *Biophysical Journal* 97:976-985.

Gentleman, E., A.N. Lay, D.A. Dickerson, E.A. Nauman, G.A. Livesay, and K.C. Dee. 2003. Mechanical characterization of collagen fibers and scaffolds for tissue engineering. *Biomaterials* 24:3805-3813.

Geubelle, P.H., and J.S. Baylor. 1998. Impact-induced delamination of composites: a 2D simulation. *Composites Part B: Engineering* 29:589-602.

Glagov, S., H.S. Bassiouny, Y. Sakaguchi, C.A. Goudet, and R.P. Vito. 1997. Mechanical determinants of plaque modeling, remodeling and disruption. *Atherosclerosis* 131, Supplement 1:S13-S14.

Golledge, J., and P. Norman. 2010. Atherosclerosis and abdominal aortic aneurysm: Cause, response or common risk factors? *Arteriosclerosis, thrombosis, and vascular biology* 30:1075-1077.

Graham, H.K., R. Akhtar, C. Kridiotis, B. Derby, T. Kundu, A.W. Trafford, and M.J. Sherratt. 2011. Localised micro-mechanical stiffening in the ageing aorta. *Mechanisms of Ageing and Development* 132:459-467.

Gregersen, H., J. Zhao, X. Lu, J. Zhou, and E. Falk. 2007. Remodeling of the zero-stress state and residual strains in apoE-deficient mouse aorta. *Biorheology* 44:75-89.

Hariton, I., G. deBotton, T.C. Gasser, and G.A. Holzapfel. 2006. Stress-driven collagen fiber remodeling in arterial walls. *Biomechanics and modeling in mechanobiology* 6:163-175.

Heidenreich, P.A., J.G. Trogdon, O.A. Khavjou, J. Butler, K. Dracup, M.D. Ezekowitz, E.A. Finkelstein, Y. Hong, S.C. Johnston, A. Khera, D.M. Lloyd-Jones, S.A. Nelson, G. Nichol, D. Orenstein, P.W. Wilson, Y.J. Woo, C. American Heart Association Advocacy Coordinating, C. Stroke, R. Council on Cardiovascular, Intervention, C. Council on Clinical, E. Council on, Prevention, A. Council on, Thrombosis, B. Vascular, C. Council on, C. Critical, Perioperative, Resuscitation, N. Council on Cardiovascular, D. Council on the Kidney in Cardiovascular, S. Council on Cardiovascular, Anesthesia, C. Interdisciplinary Council on Quality of, and R. Outcomes. 2011. Forecasting the future of cardiovascular disease in the

United States: a policy statement from the American Heart Association. Circulation 123:933-944.

Hemmasizadeh, A., M. Autieri, and K. Darvish. 2012. Multilayer material properties of aorta determined from nanoindentation tests. *Journal of the mechanical behavior of biomedical materials* 15:199-207.

Holzapfel, G.A. 2000a. Nonlinear Solid Mechanics. A Continuum Approach for Engineering. *John Wiley & Sons, Chichester*

Holzapfel, G.A. 2003. Structural and Numerical Models for the (Visco)elastic Response of Arterial Walls with Residual Stresses. In Biomechanics of Soft Tissue in Cardiovascular Systems. G. Holzapfel, and R. Ogden, editors. Springer Vienna, 109-184.

Holzapfel, G.A., and T.C. Gasser. 2001. A viscoelastic model for fiber-reinforced composites at finite strains: Continuum basis, computational aspects and applications. *Computer Methods in Applied Mechanics and Engineering* 190:4379-4403.

Holzapfel, G.A., T.C. Gasser, and R.W. Ogden. 2004a. Comparison of a Multi-Layer Structural Model for Arterial Walls With a Fung-Type Model, and Issues of Material Stability. *Journal of Biomechanical Engineering* 126:264-275.

Holzapfel, G.A., T.C. Gasser, and M. Stadler. 2002a. A structural model for the viscoelastic behavior of arterial walls: Continuum formulation and finite element analysis. *European Journal of Mechanics - A/Solids* 21:441-463.

Holzapfel, G.A., Gasser, T.C., Ogden, R.W. 2000b. A new constitutive framework for arterial wall mechanics and a comparative study of material models. *Journal of Elasticity* 61:1–48.

Holzapfel, G.A., G. Sommer, C.T. Gasser, and P. Regitnig. 2005. Determination of layer-specific mechanical properties of human coronary arteries with nonatherosclerotic intimal thickening and related constitutive modeling. *American Journal of Physiology - Heart and Circulatory Physiology* 289:H2048-H2058.

Holzapfel, G.A., G. Sommer, and P. Regitnig. 2004b. Anisotropic Mechanical Properties of Tissue Components in Human Atherosclerotic Plaques. *Journal of Biomechanical Engineering* 126:657-665.

Holzapfel, G.A., M. Stadler, and C.A.J. Schulze-Bauer. 2002b. A Layer-Specific Three-Dimensional Model for the Simulation of Balloon Angioplasty using Magnetic Resonance Imaging and Mechanical Testing. *Ann Biomed Eng* 30:753-767.

Holzapfel, G.A., and H.W. Weizsäcker. 1998. Biomechanical behavior of the arterial wall and its numerical characterization. *Computers in Biology and Medicine* 28:377-392.

Honye, J., Mahon, D. J., Jain, A., White, C. J., Ramee, S. R., Wallis, J. B., al-Zarka, A., Tobis, J. M. 1992. Morphological effects of coronary balloon angioplasty in vivo assessed by intravascular ultrasound imaging. *Circulation* 85:1012-1025.

Huang, H., R. Virmani, H. Younis, A.P. Burke, R.D. Kamm, and R.T. Lee. 2001. The Impact of Calcification on the Biomechanical Stability of Atherosclerotic Plaques. *Circulation* 103:1051-1056.

Ikoma, T., H. Kobayashi, J. Tanaka, D. Walsh, and S. Mann. 2003. Microstructure, mechanical, and biomimetic properties of fish scales from Pagrus major. *Journal of Structural Biology* 142:327-333.

Israelowitz, M., S.W. Rizvi, J. Kramer, and H.P. von Schroeder. 2005. Computational modeling of type I collagen fibers to determine the extracellular matrix structure of connective tissues. *Protein engineering, design & selection : PEDS* 18:329-335.

Janić, M., M. Lunder, and M. Šabovič. 2014. Arterial Stiffness and Cardiovascular Therapy. *BioMed Research International* 2014:11.

Jensen, L.O., G.S. Mintz, S.G. Carlier, K. Fujii, I. Moussa, G. Dangas, R. Mehran, G.W. Stone, M.B. Leon, and J.W. Moses. 2006. Intravascular ultrasound assessment of fibrous cap remnants after coronary plaque rupture. *American heart journal* 152:327-332.

Kato, Y.P., D.L. Christiansen, R.A. Hahn, S.-J. Shieh, J.D. Goldstein, and F.H. Silver. 1989. Mechanical properties of collagen fibres: a comparison of reconstituted and rat tail tendon fibres. *Biomaterials* 10:38-42.

Kiousis, D.E., S.F. Rubinigg, M. Auer, and G.A. Holzapfel. 2009. A methodology to analyze changes in lipid core and calcification onto fibrous cap vulnerability: the human atherosclerotic carotid bifurcation as an illustratory example. *Journal of biomechanical engineering* 131:121002.

Kolodgie, F.D., G. Nakazawa, G. Sangiorgi, E. Ladich, A.P. Burke, and R. Virmani. 2007. Pathology of atherosclerosis and stenting. *Neuroimaging clinics of North America* 17:285-301, vii.

Lakatta, E.G. 2008. Arterial aging is risky. *Journal of applied physiology (Bethesda, Md. : 1985)* 105:1321-1322.

Lanir, Y. 1983. Constitutive equations for fibrous connective tissues. *Journal of Biomechanics* 16:1-12.

Lawlor, M.G., M.R. O'Donnell, B.M. O'Connell, and M.T. Walsh. 2011. Experimental determination of circumferential properties of fresh carotid artery plaques. *Journal of biomechanics* 44:1709-1715.

Lee, C.-H., R. Amini, R.C. Gorman, J.H. Gorman Iii, and M.S. Sacks. 2014. An inverse modeling approach for stress estimation in mitral valve anterior leaflet valvuloplasty for in-vivo valvular biomaterial assessment. *J Biomech* 47:2055-2063.

Lei, F., and A.Z. Szeri. 2007. Inverse analysis of constitutive models: Biological soft tissues. *Journal of Biomechanics* 40:936-940.

Lendon, C.L., M.J. Davies, G.V.R. Born, and P.D. Richardson. 1991. Atherosclerotic plaque caps are locally weakened when macrophages density is increased. *Atherosclerosis* 87:87-90.

Leng, X., X. Chen, X. Deng, M.A. Sutton, and S.M. Lessner. 2015a. Simulation of Atherosclerotic Plaque Delamination Using the Cohesive Zone Model. In Mechanics of Biological Systems and Materials, Volume 7. F. Barthelat, C. Korach, P. Zavattieri, B.C. Prorok, and K.J. Grande-Allen, editors. Springer International Publishing, 81-88.

Leng, X., X. Chen, X. Deng, M.A. Sutton, and S.M. Lessner. 2015b. Modeling of Experimental Atherosclerotic Plaque Delamination. *Ann Biomed Eng* 43:2838-2851.

Leng, X., L.A. Davis, X. Deng, M.A. Sutton, and S.M. Lessner. 2016. Numerical modeling of experimental human fibrous cap delamination. *Journal of the Mechanical Behavior of Biomedical Materials* 59:322-336.

Li, D., and A.M. Robertson. 2009. A structural multi-mechanism constitutive equation for cerebral arterial tissue. *International Journal of Solids and Structures* 46:2920-2928.

Li, W.G., J. Going, N.A. Hill, and X.Y. Luo. 2013. Breaking Analysis of Artificial Elastic Tubes and Human Artery. *International Journal of Applied Mechanics* 5:1350024 (1350017 pp.).

Li, Z.-Y., T. Tang, J. U-King-Im, M. Graves, M. Sutcliffe, and J.H. Gillard. 2008. Assessment of Carotid Plaque Vulnerability Using Structural and Geometrical Determinants. *Circulation Journal* 72:1092-1099.

London, G.M., S.J. Marchais, A.P. Guerin, and B. Pannier. 2004. Arterial stiffness: pathophysiology and clinical impact. *Clinical and experimental hypertension (New York, N.Y. : 1993)* 26:689-699.

Loree, H.M., A.J. Grodzinsky, S.Y. Park, L.J. Gibson, and R.T. Lee. 1994. Static circumferential tangential modulus of human atherosclerotic tissue. *J Biomech* 27:195-204.

Loree, H.M., R.D. Kamm, R.G. Stringfellow, and R.T. Lee. 1992. Effects of fibrous cap thickness on peak circumferential stress in model atherosclerotic vessels. *Circulation Research* 71:850-858.

M.L. Benzeggagh, M.K. 1996. Measurement of Mixed-Mode delamination Fracture Toughness of Unidirectional Glass/Epoxy Composites With Mixed- Mode Bending Apparatus. *Composites Science and Technology* 49:439-449.

Madaloso, B.A., and L.A. Benvenuti. 2013. Case 4 - 84-Year old female with precordial pain and cardiac arrest with pulseless electrical activity. *Arquivos Brasileiros de Cardiologia* 101:e46-53.

Meir, K.S., and E. Leitersdorf. 2004. Atherosclerosis in the apolipoprotein-E-deficient mouse: a decade of progress. *Arterioscler Thromb Vasc Biol* 24:1006-1014.

Miehe, C. 1996. Numerical Computation of Algorithmic (Consistent) Tangent Moduli in Large Strain Computational Inelasticity. *Computer Methods in Applied Mechanics and Engineering* 134:223-240.

Miyazaki, H., and K. Hayashi. 1999. Tensile Tests of Collagen Fibers Obtained from the Rabbit Patellar Tendon. *Biomedical Microdevices* 2:151-157.

Nakashima, Y., A.S. Plump, E.W. Raines, J.L. Breslow, and R. Ross. 1994. ApoE-deficient mice develop lesions of all phases of atherosclerosis throughout the arterial tree. *Arteriosclerosis, Thrombosis, and Vascular Biology* 14:133-140.

Needleman, A. 1987. A Continuum Model for Void Nucleation by Inclusion Debonding. *Journal of Applied Mechanics* 54:525-531.

Needleman, A. 1990. An analysis of tensile decohesion along an interface. *Journal of the Mechanics and Physics of Solids* 38:289-324.

Ortiz, M., and A. Pandolfi. 1999. Finite-deformation irreversible cohesive elements for three-dimensional crack-propagation analysis. *International Journal for Numerical Methods in Engineering* 44:1267-1282.

Pal, S., A. Tsamis, S. Pasta, A. D'Amore, T.G. Gleason, D.A. Vorp, and S. Maiti. 2014. A mechanistic model on the role of "radially-running" collagen fibers on dissection properties of human ascending thoracic aorta. *Journal of Biomechanics* 47:981-988.

Pasterkamp, G., E. Falk, H. Woutman, and C. Borst. 2000. Techniques characterizing the coronary atherosclerotic plaque: influence on clinical decision making? *Journal of the American College of Cardiology* 36:13-21.

Peña, E., B. Calvo, M.A. Martínez, and M. Doblaré. 2007. An anisotropic visco-hyperelastic model for ligaments at finite strains. Formulation and computational aspects. *International Journal of Solids and Structures* 44:760-778.

Prim, D.A., B. Zhou, A. Hartstone-Rose, M.J. Uline, T. Shazly, and J.F. Eberth. 2016. A mechanical argument for the differential performance of coronary artery grafts. *Journal of the mechanical behavior of biomedical materials* 54:93-105.

Qiu, H., C. Depre, K. Ghosh, R.G. Resuello, F.F. Natividad, F. Rossi, A. Peppas, Y.T. Shen, D.E. Vatner, and S.F. Vatner. 2007. Mechanism of gender-specific differences in aortic stiffness with aging in nonhuman primates. *Circulation* 116:669-676.

Rajesh, R. 2000. Coupled Thermomechanical Analysis of Viscoelastic Dampers. *State University of New York at Buffalo*

RDSG Campillho, M.B., JABP Neto, LFM. da Silva. 2013. Modelling adhesive joints with cohesive models: effect of the cohesive law shape of the adhesive layer. *International Journal of Adhesion and Adhesives* 44:48-56.

Redheuil, A., W.C. Yu, E. Mousseaux, A.A. Harouni, N. Kachenoura, C.O. Wu, D. Bluemke, and J.A. Lima. 2011. Age-related changes in aortic arch geometry: relationship with proximal aortic function and left ventricular mass and remodeling. *Journal of the American College of Cardiology* 58:1262-1270.

Richardson, P.D., M.J. Davies, and G.V.R. Born. 1989. INFLUENCE OF PLAQUE CONFIGURATION AND STRESS DISTRIBUTION ON FISSURING OF CORONARY ATHEROSCLEROTIC PLAQUES. *The Lancet* 334:941-944.

Rodríguez, J.F., C. Ruiz, M. Doblaré, and G.A. Holzapfel. 2008. Mechanical Stresses in Abdominal Aortic Aneurysms: Influence of Diameter, Asymmetry, and Material Anisotropy. *Journal of Biomechanical Engineering* 130:021023-021023.

Roy, Y.A., and R. Dodds, Jr. 2001. Simulation of ductile crack growth in thin aluminum panels using 3-D surface cohesive elements. *Int J Fract* 110:21-45.

Sakai, S., Mizuno, K., Yokoyama, S., Tanabe, J., Shinada, T., Seimiya, K., Takano, M., Ohba, T., Tomimura, M., Uemura, R., Imaizumi, T. 2003. Morphologic changes in infarct-related plaque after coronary stent placement: A serial angioscopy study. *J. Am. Coll. Cardiol.* 42:1558-1565.

Schulze-Bauer, C.A.J., and G.A. Holzapfel. 2003. Determination of constitutive equations for human arteries from clinical data. *Journal of Biomechanics* 36:165-169.

Schwartz, S.M., Z.S. Galis, M.E. Rosenfeld, and E. Falk. 2007. Plaque rupture in humans and mice. *Arteriosclerosis, thrombosis, and vascular biology* 27:705-713.

Screen, H.R.C. 2008. Investigating load relaxation mechanics in tendon. *Journal of the Mechanical Behavior of Biomedical Materials* 1:51-58.

Sekikawa, A., C. Shin, J.D. Curb, E. Barinas-Mitchell, K. Masaki, A. El-Saed, T.B. Seto, R.H. Mackey, J. Choo, A. Fujiyoshi, K. Miura, D. Edmundowicz, L.H. Kuller, H.

Ueshima, and K. Sutton-Tyrrell. 2012. Aortic stiffness and calcification in men in a population-based international study. *Atherosclerosis* 222:473-477.

Shazly, T., A. Rachev, S.M. Lessner, W. Argraves, J. Ferdous, B. Zhou, A. Moreira, and M.A. Sutton. 2014. On the Uniaxial Ring Test of Tissue Engineered Constructs. *Exp Mech* 1-11.

Shen, Z.L., M.R. Dodge, H. Kahn, R. Ballarini, and S.J. Eppell. 2008. Stress-Strain Experiments on Individual Collagen Fibrils. *Biophysical Journal* 95:3956-3963.

Shen, Z.L., H. Kahn, R. Ballarini, and S.J. Eppell. 2011. Viscoelastic properties of isolated collagen fibrils. *Biophysical journal* 100:3008-3015.

SIMPSON, C.F., and R.J. BOUCEK. 1983. The B-aminopropionitrile-fed turkey: a model for detecting potential drug action on arterial tissue. *Cardiovascular Research* 17:26-32.

Sokolis, D.P., E.P. Kritharis, A.T. Giagini, K.M. Lampropoulos, S.A. Papadodima, and D.C. Iliopoulos. 2012. Biomechanical response of ascending thoracic aortic aneurysms: association with structural remodelling. *Computer methods in biomechanics and biomedical engineering* 15:231-248.

Sommer, G., T.C. Gasser, P. Regitnig, M. Auer, and G.A. Holzapfel. 2008. Dissection properties of the human aortic media: an experimental study. *Journal of biomechanical engineering* 130:021007.

Sommer, G., and G.A. Holzapfel. 2012. 3D constitutive modeling of the biaxial mechanical response of intact and layer-dissected human carotid arteries. *Journal of the Mechanical Behavior of Biomedical Materials* 5:116-128.

Sun, W., E.L. Chaikof, and M.E. Levenston. 2008. Numerical approximation of tangent moduli for finite element implementations of nonlinear hyperelastic material models. *Journal of biomechanical engineering* 130:061003.

Szasz, T., G.F. Bomfim, and R.C. Webb. 2013. The influence of perivascular adipose tissue on vascular homeostasis. *Vascular health and risk management* 9:105-116.

Tavora, F., N. Cresswell, L. Li, D. Fowler, and A. Burke. 2010. Frequency of acute plaque ruptures and thin cap atheromas at sites of maximal stenosis. *Arq Bras Cardiol* 94:153-159.

Tearney, G.J., et al. 2012. Consensus standards for acquisition, measurement, and reporting of intravascular optical coherence tomography studies: A report From the International Working Group for Intravascular Optical Coherence Tomography Standardization and Validation. *J. Am. Coll. Cardiol.* 59:1058-1072.

Teng, Z., J. Feng, Y. Zhang, M.P.F. Sutcliffe, Y. Huang, A.J. Brown, Z. Jing, Q. Lu, and J.H. Gillard. 2015. A uni-extension study on the ultimate material strength and

extreme extensibility of atherosclerotic tissue in human carotid plaques. *J Biomech* 48:3859-3867.

Tong, J., G. Sommer, P. Regitnig, and G. Holzapfel. 2011. Dissection Properties and Mechanical Strength of Tissue Components in Human Carotid Bifurcations. *Ann Biomed Eng* 39:1703-1719.

Tsamis, A., J.T. Krawiec, and D.A. Vorp. 2013. Elastin and collagen fibre microstructure of the human aorta in ageing and disease: a review. *Journal of the Royal Society, Interface / the Royal Society* 10:20121004.

Tsamis, A., N. Stergiopulos, and A. Rachev. 2009. A structure-based model of arterial remodeling in response to sustained hypertension. *Journal of biomechanical engineering* 131:101004.

Turon, A., P.P. Camanho, J. Costa, and C.G. Dávila. 2006. A damage model for the simulation of delamination in advanced composites under variable-mode loading. *Mechanics of Materials* 38:1072-1089.

Tvergaard, V. 1990. Effect of fibre debonding in a whisker-reinforced metal. *Materials Science and Engineering: A* 125:203-213.

Tvergaard, V., and J.W. Hutchinson. 1992. The relation between crack growth resistance and fracture process parameters in elastic-plastic solids. *Journal of the Mechanics and Physics of Solids* 40:1377-1397.

Twal, W.O., S.C. Klatt, K. Harikrishnan, E. Gerges, M.A. Cooley, T.C. Trusk, B. Zhou, M.G. Gabr, T. Shazly, S.M. Lessner, R.R. Markwald, and W.S. Argraves. 2013. Cellularized Microcarriers as Adhesive Building Blocks for Fabrication of Tubular Tissue Constructs. *Ann Biomed Eng* 42:1470-1481.

Unterberger, M.J., K.M. Schmoller, C. Wurm, A.R. Bausch, and G.A. Holzapfel. 2013. Viscoelasticity of cross-linked actin networks: experimental tests, mechanical modeling and finite-element analysis. *Acta biomaterialia* 9:7343-7353.

Ushiki, T. 2002. Collagen fibers, reticular fibers and elastic fibers. A comprehensive understanding from a morphological viewpoint. *Archives of histology and cytology* 65:109-126.

van der Rijt, J.A.J., K.O. van der Werf, M.L. Bennink, P.J. Dijkstra, and J. Feijen. 2006. Micromechanical Testing of Individual Collagen Fibrils. *Macromolecular Bioscience* 6:697-702.

Van Herck, J.L., De Meyer, G. R., Martinet, W., Van Hove, C. E., Foubert, K., Theunis, M. H., Apers, S., Bult, H., Vrints, C. J., Herman, A. G. 2009. Impaired fibrillin-1 function promotes features of plaque instability in apolipoprotein E-deficient mice. *Circulation* 120:2478-2487.

Venkatasubramaniam, A.K., M.J. Fagan, T. Mehta, K.J. Mylankal, B. Ray, G. Kuhan, I.C. Chetter, and P.T. McCollum. 2004. A Comparative Study of Aortic Wall Stress Using Finite Element Analysis for Ruptured and Non-ruptured Abdominal Aortic Aneurysms. *European Journal of Vascular and Endovascular Surgery* 28:168-176.

Verhagen, S.N., and F.L. Visseren. 2011. Perivascular adipose tissue as a cause of atherosclerosis. *Atherosclerosis* 214:3-10.

Versluis, A., A.J. Bank, and W.H. Douglas. 2006. Fatigue and plaque rupture in myocardial infarction. *J Biomech* 39:339-347.

Virmani, R., Narula, J., Leon, M. B. and Willerson, J. T. (eds). 2007. The Vulnerable Atherosclerotic Plaque: Strategies for Diagnosis and Management. *Malden, MA, Blackwell Futura* 37-59.

Walraevens, J., B. Willaert, G. De Win, A. Ranftl, J. De Schutter, and J.V. Sloten. 2008. Correlation between compression, tensile and tearing tests on healthy and calcified aortic tissues. *Medical Engineering & Physics* 30:1098-1104.

Wang, M.C., G.D. Pins, and F.H. Silver. 1994. Collagen fibres with improved strength for the repair of soft tissue injuries. *Biomaterials* 15:507-512.

Wang, Y., J.A. Johnson, A. Fulp, M.A. Sutton, and S.M. Lessner. 2013. Adhesive strength of atherosclerotic plaque in a mouse model depends on local collagen content and elastin fragmentation. *Journal of biomechanics* 46:716-722.

Wang, Y., J.A. Johnson, F.G. Spinale, M.A. Sutton, and S.M. Lessner. 2014. Quantitative Measurement of Dissection Resistance in Intimal and Medial Layers of Human Coronary Arteries. *Exp Mech* 54:677-683.

Wang, Y., J. Ning, J.A. Johnson, M.A. Sutton, and S.M. Lessner. 2011. Development of a quantitative mechanical test of atherosclerotic plaque stability. *Journal of biomechanics* 44:2439-2445.

Weiss, J.A., B.N. Maker, and S. Govindjee. 1996. Finite element implementation of incompressible, transversely isotropic hyperelasticity. *Computer Methods in Applied Mechanics and Engineering* 135:107-128.

Xu, X.P., and A. Needleman. 1993. Void nucleation by inclusion debonding in a crystal matrix. *Modelling and Simulation in Materials Science and Engineering* 1:111-132.

Y. Arun Roy, R.H.D.J. 2001. Simulation of ductile crack growth in thin aluminum panels using 3-D surface cohesive elements. *International Journal of Fracture* 110:21-45.

Yamamoto, E., K. Hayashi, and N. Yamamoto. 1999. Mechanical Properties of Collagen Fascicles From the Rabbit Patellar Tendon. *Journal of Biomechanical Engineering* 121:124-131.

Yanagisawa, H., E.C. Davis, B.C. Starcher, T. Ouchi, M. Yanagisawa, J.A. Richardson, and E.N. Olson. 2002. Fibulin-5 is an elastin-binding protein essential for elastic fibre development in vivo. *Nature* 415:168-171.

Yang, L., K.O. van der Werf, C.F.C. Fitié, M.L. Bennink, P.J. Dijkstra, and J. Feijen. 2008. Mechanical Properties of Native and Cross-linked Type I Collagen Fibrils. *Biophysical Journal* 94:2204-2211.

Yang, L., K.O. van der Werf, B.F.J.M. Koopman, V. Subramaniam, M.L. Bennink, P.J. Dijkstra, and J. Feijen. 2007. Micromechanical bending of single collagen fibrils using atomic force microscopy. *Journal of Biomedical Materials Research Part A* 82A:160-168.

Zareh, M., G. Fradet, G. Naser, and H. Mohammadi. 2015. Are two-dimensional images sufficient to assess the atherosclerotic plaque vulnerability: a viscoelastic and anisotropic finite element model. *Cardiovascular System* 3:3.

Zeinali-Davarani, S., L.G. Raguin, D.A. Vorp, and S. Baek. 2011. Identification of in vivo material and geometric parameters of a human aorta: toward patient-specific modeling of abdominal aortic aneurysm. *Biomechanics and modeling in mechanobiology* 10:689-699.

Zhou, B., A. Rachev, and T. Shazly. 2015. The biaxial active mechanical properties of the porcine primary renal artery. *Journal of the Mechanical Behavior of Biomedical Materials* 48:28-37.

Zhou, B., S. Ravindran, J. Ferdous, A. Kidane, M.A. Sutton, and T. Shazly. 2016. Using Digital Image Correlation to Characterize Local Strains on Vascular Tissue Specimens. e53625.

Zhou, B., L. Wolf, A. Rachev, and T. Shazly. 2014. A Structure-Motivated Model of the Passive Mechanical Response of the Primary Porcine Renal Artery. *Journal of Mechanics in Medicine and Biology* 14:1450033.

Zulliger, M.A., P. Fridez, K. Hayashi, and N. Stergiopulos. 2004. A strain energy function for arteries accounting for wall composition and structure. *Journal of Biomechanics* 37:989-1000.

APPENDIX A – DERIVATION OF TANGENTIAL MODULUS

The use for the user material subroutine of viscoelastic material model in ABAQUS needs the tangent modulus for Newton-Rapson iteration procedures, and an approximation of the tangent modulus was implemented (Miehe, 1996; Sun et al., 2008). The Jaumann rate can be expressed as

$$\overset{\nabla}{\boldsymbol{\tau}} = \dot{\boldsymbol{\tau}} - \boldsymbol{W\tau} - \boldsymbol{\tau W^T} = \mathbb{C}^{\boldsymbol{\tau J}} : \boldsymbol{D} \tag{A.1}$$

where $\mathbb{C}^{\tau J}$ is the tangent modulus tensor for the Jaumann rate of the Kirchhoff stress. $\boldsymbol{W}$ and $\boldsymbol{D}$ are spin tensor and rate of deformation gradient tensor, which are the antisymmetric and symmetric part of the spatial velocity gradient, respectively(Sun et al., 2008).

The linearized incremental form of Jaumann rate is given by

$$\Delta\boldsymbol{\tau} - \Delta\boldsymbol{W\tau} - \boldsymbol{\tau}\Delta\boldsymbol{W^T} = \mathbb{C}^{\boldsymbol{\tau J}} : \Delta\boldsymbol{D} \tag{A.2}$$

where

$$\Delta\boldsymbol{W} = \frac{1}{2}(\Delta\boldsymbol{FF^{-1}} - (\Delta\boldsymbol{FF^{-1}})^{\boldsymbol{T}}) \tag{A.3}$$

$$\Delta\boldsymbol{D} = \frac{1}{2}(\Delta\boldsymbol{FF^{-1}} + (\Delta\boldsymbol{FF^{-1}})^{\boldsymbol{T}}) \tag{A.4}$$

The perturbation of the deformation gradient can be written as

$$\Delta\boldsymbol{F^{ij}} = \frac{\varepsilon}{2}\left(\boldsymbol{e_i}\otimes\boldsymbol{e_j F} + \boldsymbol{e_j}\otimes\boldsymbol{e_i F}\right) \tag{A.5}$$

where ε is a small perturbation parameter and $\boldsymbol{e}_i, i = 1,2,3$ represents the unit vectors in the spatial description.

With the relation of (A.5), we can obtain

$$\Delta \boldsymbol{W}^{\boldsymbol{ij}} = \frac{1}{2}\left[\frac{\varepsilon}{2}\left(\boldsymbol{e}_i \otimes \boldsymbol{e}_j \boldsymbol{F} + \boldsymbol{e}_j \otimes \boldsymbol{e}_i \boldsymbol{F}\right)\boldsymbol{F}^{-1} - \left(\frac{\varepsilon}{2}\left(\boldsymbol{e}_i \otimes \boldsymbol{e}_j \boldsymbol{F} + \boldsymbol{e}_j \otimes \boldsymbol{e}_i \boldsymbol{F}\right)\boldsymbol{F}^{-1}\right)^{\boldsymbol{T}}\right] = \boldsymbol{0} \quad \text{(A.6)}$$

$$\Delta \boldsymbol{D}^{\boldsymbol{ij}} = \frac{\boldsymbol{1}}{\boldsymbol{2}}\left[\frac{\boldsymbol{\varepsilon}}{\boldsymbol{2}}\left(\boldsymbol{e}_i \otimes \boldsymbol{e}_j \boldsymbol{F} + \boldsymbol{e}_j \otimes \boldsymbol{e}_i \boldsymbol{F}\right)\boldsymbol{F}^{-1} + \left(\frac{\varepsilon}{2}\left(\boldsymbol{e}_i \otimes \boldsymbol{e}_j \boldsymbol{F} + \boldsymbol{e}_j \otimes \boldsymbol{e}_i \boldsymbol{F}\right)\boldsymbol{F}^{-1}\right)^{\boldsymbol{T}}\right] =$$

$$\frac{\varepsilon}{2}\left(\boldsymbol{e}_i \otimes \boldsymbol{e}_j + \boldsymbol{e}_j \otimes \boldsymbol{e}_i\right) \quad \text{(A.7)}$$

So, $\Delta\boldsymbol{\tau}$ can be approximated in another form through the difference between the perturbed and unperturbed Kirchhoff stresses and we find that

$$\Delta \boldsymbol{\tau} \approx \boldsymbol{\tau}\left(\widehat{\boldsymbol{F}}^{\boldsymbol{ij}}\right) - \boldsymbol{\tau}(\boldsymbol{F}) \quad \text{(A.8)}$$

Where $\widehat{\boldsymbol{F}}^{ij} = \boldsymbol{F} + \Delta \boldsymbol{F}^{ij}$ is the perturbed deformation gradient. With the expression of equations (A.2), (A.6) and (A.7), we find that $\Delta\boldsymbol{\tau} = \mathbb{C}^{\tau J} : \Delta \boldsymbol{D}$, hence (A.8) can be written as (Sun et al., 2008)

$$\boldsymbol{\tau}\left(\widehat{\boldsymbol{F}}^{\boldsymbol{ij}}\right) - \boldsymbol{\tau}(\boldsymbol{F}) \approx \mathbb{C}^{\boldsymbol{\tau J}\,\boldsymbol{ij}} : \frac{\varepsilon}{2}\left(\boldsymbol{e}_i \otimes \boldsymbol{e}_j + \boldsymbol{e}_j \otimes \boldsymbol{e}_i\right) \quad \text{(A.9)}$$

The numerical approximation of the tangential modulus would be acquired through the application of symmetry properties:

$$\mathbb{C}^{\boldsymbol{\tau J}\,\boldsymbol{ij}} \approx \frac{1}{\varepsilon}\left[\boldsymbol{\tau}\left(\widehat{\boldsymbol{F}}^{\boldsymbol{ij}}\right) - \boldsymbol{\tau}(\boldsymbol{F})\right] \quad \text{(A.10)}$$

The tangential modulus used in the ABAQUS subroutine has the expression as follow

$$\mathbb{C}^{\boldsymbol{mJ}^{\boldsymbol{ij}}} \approx \frac{1}{J\varepsilon}\left[\boldsymbol{\tau}\left(\widehat{\boldsymbol{F}}^{\boldsymbol{ij}}\right) - \boldsymbol{\tau}(\boldsymbol{F})\right] \tag{A.11}$$

APPENDIX B – DERIVATION OF ELASTIC TENSOR

The first-order partial derivatives of effective opening displacement δ with respect to δ_{s1}, δ_{s2} and δ_n are written as (Roy and Dodds, 2001)

$$\frac{\partial \delta}{\partial \delta_{s1}} = \frac{\partial \delta}{\partial \delta_s}\frac{\partial \delta_s}{\partial \delta_{s1}} = \frac{\lambda^2 \delta_{s1}}{\delta} \tag{B.1}$$

$$\frac{\partial \delta}{\partial \delta_{s2}} = \frac{\partial \delta}{\partial \delta_s}\frac{\partial \delta_s}{\partial \delta_{s2}} = \frac{\lambda^2 \delta_{s2}}{\delta} \tag{B.2}$$

$$\frac{\partial \delta}{\partial \delta_n} = \frac{\partial \delta}{\partial \delta_n} = \frac{\delta_n}{\delta} \tag{B.3}$$

And also the second-order partial derivatives of effective opening displacement δ with respect to δ_{s1}, δ_{s2} and δ_n are expressed as

$$\frac{\partial^2 \delta}{\partial \delta_{s1}\partial \delta_{s1}} = -\lambda^2 \delta_{s1}\frac{\lambda^2 \delta_{s1}}{\delta^3} + \frac{\lambda^2}{\delta} \tag{B.4}$$

$$\frac{\partial^2 \delta}{\partial \delta_{s2}\partial \delta_{s2}} = -\lambda^2 \delta_{s2}\frac{\lambda^2 \delta_{s2}}{\delta^3} + \frac{\lambda^2}{\delta} \tag{B.5}$$

$$\frac{\partial^2 \delta}{\partial \delta_n \partial \delta_n} = -\delta_n \frac{\delta_n}{\delta^3} \tag{B.6}$$

The individual traction components can be expressed using the chain rule as

$$t_i = \frac{\partial \varphi}{\partial \delta}\frac{\partial \delta}{\partial v_i} = \varphi' \frac{\partial \delta}{\partial v_i} = t\frac{\partial \delta}{\partial v_i} \tag{B.7}$$

where subscripts $i = 1, 2$ and 3 represent $\mathrm{s1}$, $\mathrm{s2}$, and n, respectively. To maintain consistent notation, let the relative displacements, $(v_1,\ v_2,\ v_3) = (\delta_{s1},\ \delta_{s2},\ \delta_n)$.

Under conditions of loading, the relationship between effective traction, t and effective displacement, δ can be specified as

$$t_1 = t\frac{\partial\delta}{\partial\delta_{s1}} = t\frac{\lambda^2\delta_{s1}}{\delta} \tag{B.8}$$

$$t_2 = t\frac{\partial\delta}{\partial\delta_{s2}} = t\frac{\lambda^2\delta_{s2}}{\delta} \tag{B.9}$$

$$t_3 = t\frac{\partial\delta}{\partial\delta_n} = t\frac{\delta_n}{\delta} \tag{B.10}$$

The tangent modulus matrix, $\boldsymbol{D}$ can be derived as

$$D_{ij} = \frac{\partial t_i}{\partial v_j} = \frac{\partial\left(\varphi'\frac{\partial\delta}{\partial v_i}\right)}{\partial v_j} = \frac{\partial\varphi'}{\partial v_j}\frac{\partial\delta}{\partial v_i} + \varphi'\frac{\partial^2\delta}{\partial v_j\partial v_i} = \varphi''\frac{\partial\delta}{\partial v_j}\frac{\partial\delta}{\partial v_i} + \varphi'\frac{\partial^2\delta}{\partial v_j\partial v_i} \tag{B.11}$$

And with the properties shown as

$$D_{ij} = D_{ji} \tag{B.12}$$

Using (B.7), (B.11) gives

$$D_{11} = \varphi''\frac{\partial\delta}{\partial\delta_{s1}}\frac{\partial\delta}{\partial\delta_{s1}} + \varphi'\frac{\partial^2\delta}{\partial\delta_{s1}\partial\delta_{s1}} = \frac{\varphi'\lambda^2}{\delta} + \frac{\lambda^4{\delta_{s1}}^2}{\delta^2}\left[\varphi'' - \frac{\varphi'}{\delta}\right] \tag{B.13}$$

$$D_{12} = D_{21} = \varphi''\frac{\partial\delta}{\partial\delta_{s1}}\frac{\partial\delta}{\partial\delta_{s2}} + \varphi'\frac{\partial^2\delta}{\partial\delta_{s1}\partial\delta_{s2}} = \frac{\lambda^4\delta_{s1}\delta_{s2}}{\delta^2}\left[\varphi'' - \frac{\varphi'}{\delta}\right] \tag{B.14}$$

$$D_{13} = D_{31} = \varphi''\frac{\partial\delta}{\partial\delta_{s1}}\frac{\partial\delta}{\partial\delta_n} + \varphi'\frac{\partial^2\delta}{\partial\delta_{s1}\partial\delta_n} = \frac{\lambda^2\delta_{s1}\delta_n}{\delta^2}\left[\varphi'' - \frac{\varphi'}{\delta}\right] \tag{B.15}$$

$$D_{22} = \varphi''\frac{\partial\delta}{\partial\delta_{s2}}\frac{\partial\delta}{\partial\delta_{s2}} + \varphi'\frac{\partial^2\delta}{\partial\delta_{s2}\partial\delta_{s2}} = \frac{\varphi'\lambda^2}{\delta} + \frac{\lambda^4{\delta_{s2}}^2}{\delta^2}\left[\varphi'' - \frac{\varphi'}{\delta}\right] \tag{B.16}$$

$$D_{23} = D_{32} = \varphi''\frac{\partial\delta}{\partial\delta_{s2}}\frac{\partial\delta}{\partial\delta_n} + \varphi'\frac{\partial^2\delta}{\partial\delta_{s2}\partial\delta_n} = \frac{\lambda^2\delta_{s2}\delta_n}{\delta^2}\left[\varphi'' - \frac{\varphi'}{\delta}\right] \tag{B.17}$$

$$D_{33} = \varphi''\frac{\partial\delta}{\partial\delta_n}\frac{\partial\delta}{\partial\delta_n} + \varphi'\frac{\partial^2\delta}{\partial\delta_n\partial\delta_n} = \frac{\varphi'}{\delta} + \frac{{\delta_n}^2}{\delta^2}\left[\varphi'' - \frac{\varphi'}{\delta}\right] \tag{B.18}$$

And φ'' is defined as

$$\varphi'' = \frac{\varphi'}{\delta}\left[1 - \frac{\delta}{\delta_c}\right] \tag{B.19}$$

For unloading,

$$\varphi' = \left(\frac{t_{max}}{\delta_{max}}\right)\delta \tag{B.20}$$

and

$$\varphi'' = \left(\frac{t_{max}}{\delta_{max}}\right) \tag{B.21}$$

For purposes of display of results, we shall find it convenient to define a damage parameter

$$d = \frac{\varphi(\delta_{max})}{G_c} \tag{B.22}$$

Evidently, d ranges from 0 to 1, with these limits corresponding to an intact and a fully damaged cohesive surface, respectively. Furthermore, it follows that

$$\dot{d} \geq 0 \tag{B.23}$$

APPENDIX C – INVERSE ANALYSIS METHOD

Inverse analysis assumes that the history of variables (e.g., force, displacement and stress) are given in a test (e.g., uniaxial tensile test) and it attempts to obtain a set of parameter values which would generate a good fit to the given variables history after a direct analysis by using these parameter values (Lei and Szeri, 2007). The objective function describes the variations between the predicted and experimental results, is defined to be

$$f = \sum_{i=1}^{n} \left[F_{p_i} - F_{e_i} \right]^2 \qquad \text{(C.1)}$$

where F_{p_i} and F_{e_i} are predicted and experimental results (forces), respectively, at the *i*th increment. A reasonable set of parameters values would yield when the objective function is minimized to an acceptable value.

The routine "lsqnonlin" of MATLAB is used to solve the nonlinear least-squares analysis in order to obtain a set of optimized results through direct calculations with an arbitrary initial set of parameter values passing to the target set of values. A python program generates input file for ABAQUS with initial guess of material parameter values. A MATLAB code calls an external finite element program ABAQUS to run the direct analysis with the input file and an output file .odb will be yielded. An output file is generated with another Python program by using .odb file and the predicted results are used for the comparison with the experimental results. Later, a new set of parameter values will

be found through the routine “lsqnonlin” and will be transferred to the input file for another direct analysis. A series of cycles will generate an optimized set of parameter values when the criteria met.